Uncooled Carbon Microbolometer Imager

Thesis by

Matthieu Liger

In Partial Fulfillment of the Requirements

for the Degree of

Doctor of Philosophy

California Institute of Technology

Pasadena, California

2006

(Defended September 13, 2005)

To my father, Xavier Liger

Acknowledgements

I will start by thanking my advisor, Yu-Chong Tai, first for giving me the opportunity to study and work in the Caltech Micromachining Laboratory and for mentoring me. I only wish I could be as creative and optimistic as he is.

There are other professors I want to thank. First, my sophomore-year physics teacher, Valérie Douay. If it wasn't for her extremely well-taught and inspiring electromagnetism class, I might not be here today. I am also thankful to the Professors who sat in my candidacy committee and/or defense committee: Ali Hajimiri, Ellis Meng, Oskar Painter, Demetri Psaltis, Axel Scherer, and Changhuei Yang.

Thanks to the "senior" labmates who taught me how to work around the lab, especially Nick Pornsin-Sirirak, Yong Xu, Jun Xie, Tze-Jung Yao and Ellis Meng. I still cannot believe I am now the senior guy in the lab. Thanks to my officemates Victor Shih and Qing He for some great discussions and to the rest of the Caltech Micromachining lab: Damien Rodger, Justin Boland, Ted Harder, Scott Miserendino, Angela Tooker, Siyang Zheng; the great Tanya Owen for taking such good care of us and Trevor Roper for taking care of the machines, some of which, being older than us, can be a handful. I also want to acknowledge Professor Satoshi Konishi of Ritsumeikan University and Doctor Stacey Boland who made some of the measurements presented in Chapter 3.

Thanks to the Caltech staff in general for making Caltech such wonderful environment for students; I am thinking especially of the people at the International Students Programs office: Parandeh Kia, Jim Endrizzi and Tara Tram. To Linda Dozsa, Veronica Robles, and Janet Couch from the electrical engineering department, to the staff of Red Door Cafe for the thousands of double expressos I must have had there, and the Chandler pizza guys.

I thank the people without whom my years in graduate school would not have been as pleasant. From the very first days of the international student orientation at Caltech: Vincent Hibon, Jeremy Witzens, Michela Muñoz-Fernandez, Behnam Analui and Abbas

Komijani, then later Hossein Hashemi, Sam Mandegaran, Nikoo Saber, Leila Setayeshgar, Lisa Cowan, Roya Bahreini, Ivana Komunjer, Maxime Rattier, Fatemeh Jalayer, Eva Kanso, Aaron Sorkin, and last but not least, Maryam Fazel. My roomates Olivier Delaire, Nicolas Ponchaut, Frank Ducheneaux, and Pierre Moreels for tolerating me, even when I was asleep on the couch.

Finally, I thank my parents who tried to deal with a kid who was more interested in doing experiments in the basement than he was in doing his homework. As it turned out, fifteen years later I was still doing experiments, but in another basement.

Abstract

The discovery of infrared radiation two centuries ago and the theory of blackbody radiation one century later have given birth to the field of thermal imaging. Since then, researchers have devised numerous ways to detect infrared radiation. From World War II to the 1980s, semiconductor-based cooled photon detector arrays have reigned over the field of thermal imaging. Albeit limited to expensive, bulky systems used for military applications due to their cooling requirement they have been . The emergence of micromachining techniques in the 1980s however, have allowed for the development of uncooled, thermal detector arrays. Uncooled systems are expected to find more and more applications, especially in the civilian world.

Here we present a novel and simple way to fabricate uncooled infrared detectors suitable for integration into large-area arrays. The design is based on carbon obtained by means of polymer pyrolysis. We demonstrate how some electrical and thermal properties can be adjusted by process parameters, and then present the first micromachined carbon uncooled bolometer made of two-layers of self-supporting pyrolyzed-parylene carbon having different process-tuned properties.

Finally, based on this unique design and fabrication process, we develop a carbon bolometer array and demonstrate the thermal imaging capability by taking thermal images. Measurements show that the sensitivity to target temperature can be as low as $31mK$ and $44mK$ for $100\mu s$ and $12\mu s$ electrical signal integration time, respectively. This matches the current state of the art which is very promising considering the fact that this is the first time pyrolytic carbon has been used to fabricate a microbolometer array.

Contents

List of Figures

List of Tables

Notations, Abbreviations and Physical Constants

Quantity	**Symbol**	**Unit**
Voltage Responsivity	$\Re$	$V.W^{-1}$
Temperature Coefficient of Resistance TCR	α	K^{-1}
Radiant Flux	Φ	W
Spectral Radiant Flux	Φ_λ	$W.m^{-1}$
Radiance	L	$W.m^{-2}.sr^{-1}$
Exitance	M	$W.m^{-2}$
Irradiance	E	$W.m^{-2}$
Intensity	I	$W.sr^{-1}$
Spectral Radiance	L_λ	$W.m^{-3}.sr^{-1}$
Spectral Exitance	M_λ	$W.m^{-3}$
Spectral Irradiance	E_λ	$W.m^{-3}$
Numerical Aperture	NA	1
F-number	F	1
Noise Voltage	V_n	V
Johnson Noise Voltage	V_j	V
$1/f$ Noise Voltage	V_f	V
Noise-Equivalent Power	NEP	W

Noise-Equivalent Temperature Difference	$NETD$	K
Focal Length	f	m
Thermal Conductivity	G_{th}	$W.K^{-1}$
Thermal Conductance	κ	$W.K^{-1}.m^{-1}$
Thermal Time Constant	τ_{th}	s
Heat Capacity	C_{th}	$J.K^{-1}$
Specific Heat Capacity	C	$J.Kg^{-1}K^{-1}$
Volumetric Heat Capacity	C_v	$J.m^{-3}$
Boltzmann Constant	k	$J.K^{-1}$
Temperature	T	K
Bias Current	I_b	A
Bias Voltage	V_b	V
Detectivity	D^*	$m.Hz^{1/2}W^{-1}$
Wavelength	λ	m
Resistance	R	Ω
Resistivity	ρ	$\Omega.m$
Contact Resistance	ρ_c	$\Omega.m^2$
Conductivity	σ	$\Omega^{-1}.m^{-1}$
Activation Energy	E_a	J
Bandwidth	B	Hz
Hooge Constant	α_H	1

Acronym	**Description**
MEMS	Micro Electro-Mechanical Systems

AC	Alternating Current
DC	Direct Current
IR	Infrared
MWIR	Medium Wavelength Infrared
LWIR	Long Wavelength Infrared
NIR	Near Infrared
TCR	Temperature Coefficient of Resistance
NETD	Noise Equivalent Temperature Difference
NEP	Noise Equivalent Power
LPCVD	Low Pressure Chemical Vapor Deposition
PECVD	Plasma Enhanced Chemical Vapor Deposition
VOx	Vanadium Oxide
MCT	Mercury-Cadium-Telluride
CMP	Chemical-Mechanical Polishing
TEM	Transmission Electron Microscope
TGA	Thermogravimetric Analysis
DSC	Differential Scanning Calorimetry
CMOS	Complementary Metal-Oxide Semiconductor
RIE	Reactive Ion Etching
DRIE	Deep Reactive Ion Etching
TMAH	Tetramethyl Ammonium Hydroxide
HMDS	Hexamethyldisilazane
AMTIR	Amorphous Material Transmitting Infrared
GPIB	General Purpose Interface Bus
ADC	Analog to Digital Converter

STI	Shallow Trench Isolation

Constant	**Symbol**	**Value**	**Unit**
Boltzmann Constant	k	$1.38065\,10^{-23}$	$J.K^{-1}$
Planck Constant	h	$6.62607\,10^{-34}$	$J.s^{-1}$
Stefan-Boltzmann Constant	σ_b	$5.6704\,10^{-8}$	$W.K^{-4}.m^{-2}$
Speed of Light in Vacuum	c	$2.9979\,10^{8}$	$m.s^{-1}$
Electron Charge	q	$1.6021\,10^{-19}$	C

Chapter 1

Introduction

1.1 Infrared Light and Thermal Imaging

In 1800, German-born British astronomer and Uranus discoverer William Herschel was studying solar radiation. Using a prism to separate the different wavelengths while monitoring the change in temperature on thermometers in the different color regions (Figure 1.1), he noticed, by design or by chance that if he put a thermometer beyond the red region, the corresponding temperature was increasing as well. He wrote[1]:

> "Thermometer No. 1 rose 7 degrees, in 10 minutes, by an exposure to the full red coloured rays. I drew back the stand,..... thermometer No. 1 rose, in 16 minutes, 8 3/8 degrees when its center was 1/2 inch out of the visible rays of the sun. .....**The first four experiments prove, that there are rays coming from the sun, which are less refrangible than any of those that affect the sight. They are invested with a high power of heating bodies but with none of illuminating objects; and this explains the reason why they have hitherto escaped unnoticed.**"

He had just discovered infrared radiation.[1]

The term "Infrared" from Latin *infra*, "below," is usually considered to apply to wavelength between $700nm$ and $1mm$. It can be argued that the first occurrence of infrared sensing actually goes back several millennia, when men placed their hand over a recently extinguished fire [2]. However, until Herschel's experiment this kind of infrared was simply

[1]The reader might wonder if he tried to do the same outside of the violet color region: he did. However, not being able to measure any change of temperature when placing his thermometers outside the violet, he concluded that the sun does not radiate beyond the visible violet .

Figure 1.1: Sir William Herschel Discovering Infrared Radiation

known as heat, or "radiant heat," and no one wondered what its similarities were with visible light[1].

In 1879, Joseph Stefan concluded from experimental data that the power transferred between two bodies was proportional to the difference of the fourth power of their temperature, a result later theoretically proven by Ludwig Boltzmann in 1884[3]. In 1896, Wilhelm Wien experimentally found that the wavelength of maximum radiation of a blackbody is inversely proportional to its absolute temperature[4]:

$$\lambda_{max} = \frac{0.28978}{T} \tag{1.1}$$

However, Wien's attempts to find the blackbody radiation distribution law failed. It was in 1901 that Max Planck first published the correct blackbody radiation law [5], giving the spectral exitance of the electromagnetic radiation emitted by a blackbody at a given temperature

$$M_\lambda(T,\lambda) = \frac{2\pi hc^2}{\lambda^5(e^{(hc/\lambda kT)}-1)}(W.m^{-3}), \tag{1.2}$$

Near Infrared	NIR	$0.7\mu m - 1.4\mu m$
Short Wavelength Infrared	SWIR	$1.4\mu m - 3\mu m$
Medium Wavelength Infrared	MWIR	$3\mu m - 8\mu m$
Long wavelength	LWIR	$8\mu m - 15\mu m$
Far Infrared	FIR	$15\mu m - 1000\mu m$

Table 1.1: Infrared Wavelength Regions

where M_λ is the spectral exitance, λ the wavelength considered, h Planck's constant, c the velocity of light in vacuum, and T the temperature (see Section 2.2.1 for more details on blackbody radiation).

1.1.1 Types of Infrared Light

What is considered to be infrared light spans 3 orders of magnitude and is usually divided into several regions that have different practical significance (Table 1.1). The near infrared spans from $1.5\mu m$ to $1.4\mu m$. It is used in telecommunications and is itself subdivided into several regions. Another application for near-infrared is remote sensing, e.g., to study and detect vegetation by their optical signature. Short and medium wavelength infrared can be used to detect some gases. Long wavelength infrared ($8\mu m - 14\mu m$) finds its main use in thermal imaging [6].

1.1.2 Atmospheric Transmission

Figure 1.2 shows the transmission spectrum of the earth's atmosphere through a $1km$ path. Due to absorption from water and carbon dioxide, the atmosphere is not transparent to all infrared wavelengths. As can be seen on the figure, there are two bands of wavelength to which the atmosphere is transparent: the $3\mu m - 5\mu m$ and the $8\mu m - 14\mu m$. The earth's temperature being around $300K$, most of the radiation it emits is around $10\mu m$ in wavelength (see Section 2.2.1.4 for more details). Therefore, the earth's atmosphere is transparent to the earth's radiation. Note that if that was not the case, the earth temperature would be much higher and we would not be here to talk about it. The atmosphere of Venus ,for example, is much "thicker" than that of Earth. For this reason, its temperature is as high as 450° C even though its distance from the sun is comparable to the distance

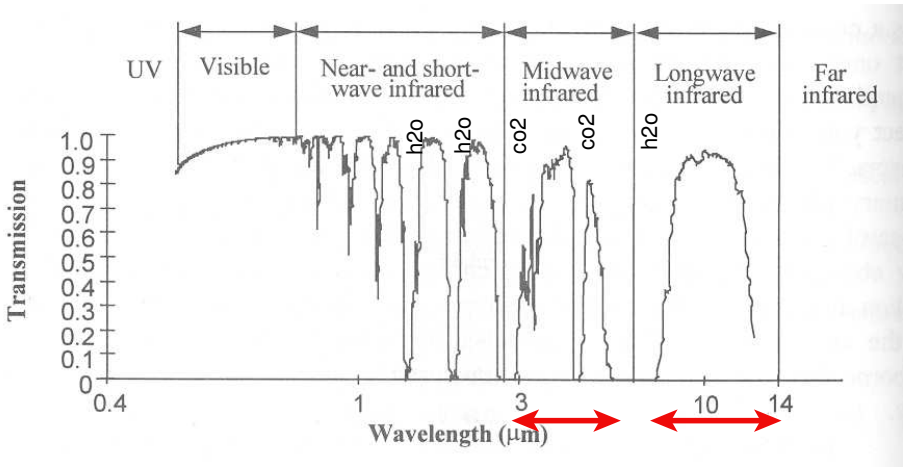

Figure 1.2: Atmosphere Transmission Spectrum

between the sun and the earth.

1.1.3 Remote Temperature Sensing and Thermal Imaging

For objects close to room temperature (300K), Wien's displacement law (Equation 1.1) predicts the wavelength of maximum blackbody emission around $10\mu m$. From the Stefan-Boltzmann law and Planck's radiation law (Equation 1.2), the amount of infrared emitted by a blackbody is a strong function of its temperature. Therefore, to remotely measured the temperature of an object, one must be able to measure the amount of infrared radiation it emits, preferably in the $8\mu m - 14\mu m$ atmospheric window. It is also possible to use the $3\mu m - 5\mu m$ window, but less infrared is emitted in this range, making it more demanding on the infrared detector that is used. Thermal imaging, which refers to the ability to measure the temperature on different points on a scene, requires either an array of infrared detectors operating in those wavelength ranges or a way to scan a scene using a single detector.

There are many applications to thermal imaging, civilian or military:

- Night vision
- Perimeter surveillance
- Vehicule/personnel detection
- Firefighting (smoke is transparent to LWIR)

- Industrial process monitoring
- Law enforcement
- Driver's vision enhancement
- Public Health (e.g., detecting individuals with fever in airports)

Figure 1.3 shows some examples of thermal images obtained with commercial uncooled thermal detector arrays.

1.2 Infrared Detectors

The different types of infrared detectors can be put in two categories: photon detectors and thermal detectors.

1.2.1 Photon Detectors

Photon detectors directly convert incoming photons into photocurrents. The energy of a photon having wavelength λ is

$$\begin{aligned} E &= \frac{hc}{\lambda} \\ E(eV) &= \frac{1.24}{\lambda(\mu m)}, \end{aligned}$$

where c is the speed of light in vacuum and h is Planck's constant. To detect infrared radiation, photon detectors use phenomena that are activated by energies between $\simeq 0.1eV$ (for LWIR) to $\simeq 1.8eV$ (for NIR).

Photodiodes In a photodiode, incoming photons are absorbed and generate electron-hole pairs that are give rise to a photocurrent. For the photons to be absorbed by the semiconductor, the bandgap of the semiconductor must be higher than the photons' energy. Figure 1.4 shows the absorption coefficient of several detector materials as a function of wavelength. For a given material, the achievable photodiode signal-to-noise ratio depends on the ratio $\frac{\alpha}{G}$, where α is the absorption coefficient and G the rate of thermal generation of free charge carriers. In the LWIR range, i.e., the most suitable range for thermal imaging, it is required to cool down the semiconductor to cryogenic temperatures ($\leq 77K$) in order to

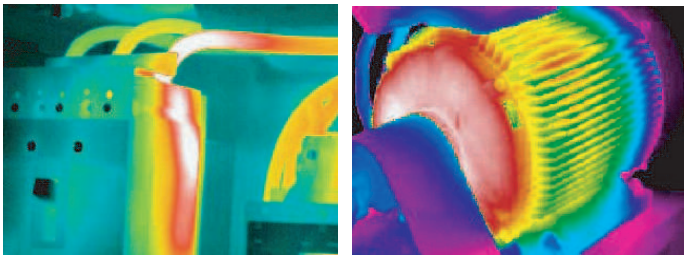

(a) Preventive Maintenance/Process Monitoring (www.indigo.com)

(c) Night Vision on Combat Field (www.indigo.com)

(d) Perimeter Surveillance (www.ulis-ir.com)

Figure 1.3: Some Examples of Thermal Imaging Applications

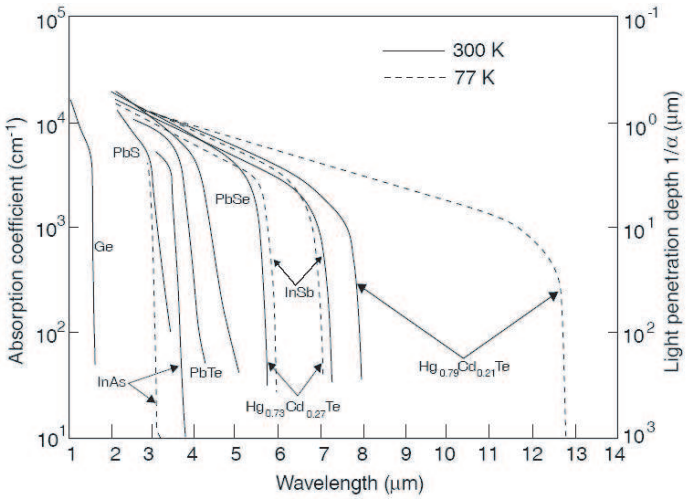

Figure 1.4: Absorbtion Coefficient for Various Materials, from [7]

obtain a good performance. One common material for LWIR detection and thermal imaging is Mercury Cadmium Telluride ($HgCdTe$, also called MCT). Other possible materials include Indium Antimonide ($InSb$), Indium Gallium Arsenide ($InGaAs$), Indium Gallium Antimonide ($InGaSb$), Mercury Zinc Telluride ($HgZnTe$), Mercury Manganese Telluride ($HgMnTe$) [7]. The bandgap of these materials can be engineered to correspond to various wavelength. For example, the bandgap of $Hg_{1-x}Cd_xTe$ was experimentally found to be[8]

$$Eg(eV) = -0.302 + 1.93x - 0.81x^2 + 0.832x^3 + 5.35 * 10^{-4}(1 - 2x)T. \tag{1.3}$$

Extrinsic Photoconductors: In extrinsic photoconductors, incoming photons excite electrons in the valence band to impurity levels inside the forbidden band. Therefore, the energy of interest is not the semiconductor bandgap but the distance between the valence level E_v and the impurity level. Highly-doped silicon detectors have been demonstrated using $Si : In$, $Si : As$, and $Si : Ga$. Again, for operation in the LWIR, this energy is small compared to thermal energy, and the devices require cooling.

Quantum Well Infrared Photodetectors (QWIP): In Quantum Well Infrared Photodetectors (QWIP), multilayer materials are used to create quantum wells. The energy levels are engineered so that the energy of infrared photons can excite electrons from those quantum wells into the conduction band. These electrons are then collected as photocurrent.

Similar to other photon detectors, QWIP need to be cooled. Even though the performance of QWIP is not as good as MCT photodiodes, their uniformity and operability and yield are higher. However, in cooled systems the cooling system accounts for a significant part of the total cost [7].

1.2.2 Thermal Detectors

Although technically also "photon detectors", thermal detectors are referred to this way because they first convert photons into heat before measuring the induced change in temperature. A thermal detector comprises an absorber which is thermally insulated to give a big temperature change upon incoming radiation. Several physical mechanisms can be used to measure this change in temperature. The main types of detection mechanisms are briefly described below.

Gas Expansion: In 1936, Hammond Hayes published a paper entitled "A receiver of Radiant Energy" in which he reported a new type of thermal detector[9]. He used pyrolyzed flower pappus as a "fluff," or gas absorber inside a closed chamber. When absorbing radiation the gas inside the fluff expanded and would cause a chamber wall displacement. The displacement was then measured capacitively, hence making device operable in Alternating Current (AC) only. Based on the same idea of gas expansion, Harold Zahl and Marcel Golay fabricated a "pneumatic infrared detector" published in 1946 [10]. Their device also used the expansion of a gas due to heat temperature, but the way to detect the gas expansion was through optical interference instead of an electrical signal. In 1947, Golay published another paper presenting an improved version using light deflection from a flexible mirror as a way to detect the gas expansion[11]. In a scanning configuration he demonstrated how to display the "heat image" of an airplane in flight.[2] Even though he was not the first to use gas expansion as a way to detect infrared light, this type of infrared detector is known as a "Golay Cell". They are still commercially available today.

Thermopiles: In 1821, Thomas Seebeck discovered the thermoelectric effect and made the first thermocouple. Seven years later, Leopoldo Nobili made the first "radiation thermocouple" using six antimony-bismuth thermocouples in series [12]. The electromotive force

[2] Which, to the author's knowledge, is the first demonstration of thermal imaging.

appearing across a thermopile made of n thermocouples is given by

$$\begin{aligned}\Delta V &= n\int_{T}^{T+\Delta T} S_a(T) - S_b(T)dT \\ &= \Delta T n(S_a - S_b) \text{ if } S_a(T) = S_a \text{ and } S_b(T) = S_b,\end{aligned}$$

where S_a and S_b are the Seebeck coefficients of the two materials the thermocouples are made of.

Pyroelectric Detectors: Pyroelectric detectors use pyroelectric materials to measure the temperature change caused by infrared radiation. Pyroelectric materials are materials that change polarization upon change in temperature. Pyroelectric detectors can only operate in AC mode, as free charges will cancel the obtained polarization in DC. The current flowing into or out of a pyroelectric detector made out of two electrode in between which is a pyroelectric material, is given by [13]

$$I = Ap\frac{dT}{dt}, \tag{1.4}$$

where A is the area of the electrodes, p the pyroelectric coefficient, and $\frac{dT}{dt}$ the rate of temperature change.

Thermomechanical Detectors: Thermomechanical infrared detectors use deflection of composite cantilevers made of two materials having different coefficients of thermal expansion. This type of composite cantilever is called a bimetalic cantilever or a bimaterial cantilever. They are (or were used) as low-cost temperature detectors in everyday applications, such as kitchen ovens or blinking Christmas decorations. The deflection at the tip of the cantilever is given by [14]

$$\Delta z = C * L^3(\alpha_1 - \alpha_2)\Delta T, \tag{1.5}$$

where C is a constant that depends on the materials' thicknesses and their Young's modulus, L is the length of the cantilever, and α_1 and α_2 are the coefficients of thermal expansion of the two layers. There are several ways this deflection can in turn be measured, e.g., optical reading (deflection of a light beam on the cantilever), capacitive sensing ,or piezoresistive

sensing.

Bolometers: Bolometers are thermal sensors that use a thermistor to measure the temperature change induced by incident infrared radiation. The change in bolometer resistance due a change in temperature is given by

$$\Delta R = \alpha R \Delta T, \tag{1.6}$$

where α is the temperature coefficient of resistance of the thermistor and ΔT the temperature change due to the incident radiation.

The theory and current state of the art of bolometers is described in detail in Chapter 2.

1.3 Micromachining for Uncooled Thermal Imaging

Since thermal detectors rely on a change of temperature induced by radiation, the sensing element of a thermal sensor must be thermally insulated. Given the dimensions achievable by conventional machining, this thermal insulation causes thermal detectors to be much slower than photon detectors. Therefore during most of the twentieth century, photon detectors were preferred to thermal detectors. However, as microelectronic fabrication techniques matured dramatically because of their use in integrated circuits, it became possible to fabricate thermal detectors that were well thermally insulated and small enough have an acceptable response time although, not comparable to that of photon detectors.

All types of uncooled thermal sensors discussed in the previous section have their micromachined version. Tunneling micro-Golay cells [15, 16], thermopile arrays [17, 18], thermomechanical sensors, and arrays [19, 14] have been demonstrated. However, so far only two technologies have found commercial success in uncooled thermal imagers: microbolometer arrays and pyroelectric arrays.

In the 1980s the US Army Night Vision Laboratory (now part of the U.S. Army's Night Vision and Electronic Sensors Directorate, NVESD) and the Defense Advanced Research Projects Agency (DARPA) funded microbolometer research at Honeywell International Inc. [2]. The results of this research were declassified in 1992, revealing unexpectedly high uncooled microbolometer performance using vanadium oxide (VOx) as thermistor material.

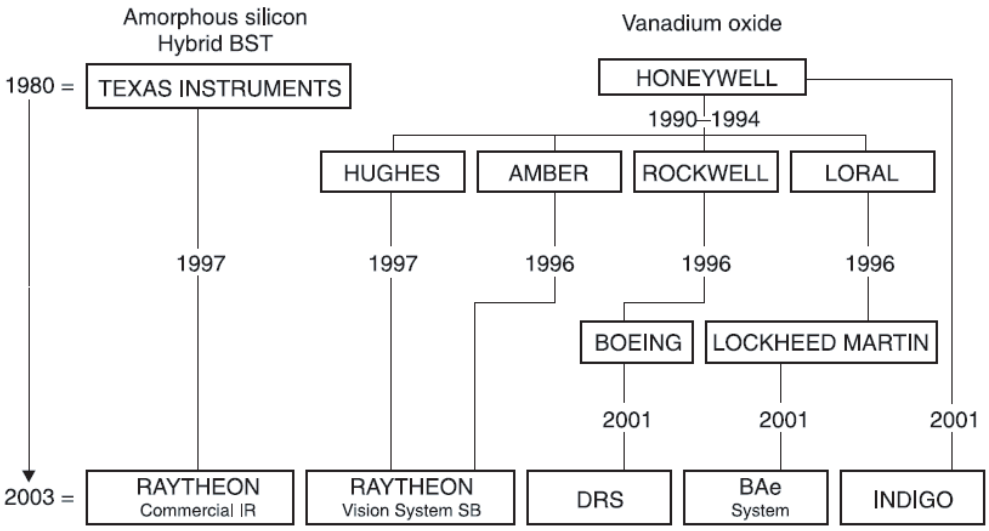

Figure 1.5: Evolution of the Uncooled Infrared Industry in the US, from [20]

At about the same time, the Army Night Vision Laboratory and DARPA also sponsored research on barium-strontium-titanate (BST) pyroelectric arrays developed at Texas Instruments (now Raytheon Company). Texas Instruments Inc. also worked on bolometers using amorphous silicon as the thermistor material. The Honeywell technology has since been licensed to several companies. Figure 1.5 shows a schematic of the evolution of the uncooled infrared detector array industry in the United States [20].

Bibliography

[1] W. Herschel, "Experiments on the refrangibility of the invisible rays of the sun," *Philosophical Transactions of the Royal Society of London*, vol. 90, pp. 284–293, 1800. Available on
http://www.jstor.org/. 1, 2

[2] R. Buser and M. Tompsett, "Historical overview," in *Semiconductor and Semimetals* (D. D. Skatrud and P. W. Kruse, eds.), vol. 47, ch. 1, Academic Press, 1997. 1, 10

[3] P. Kruse, L. McGlauchlin, and R. McQuistan, *Elements of Infrared Technology: Generation, Transmission and Detection*. John Wiley & Sons, Inc, 1962. 2

[4] "Aerospace science and technology dictionnary."
http://www.hq.nasa.gov/office/hqlibrary/aerospacedictionary/. 2

[5] M. Planck, "On the law of distribution of energy in the normal spectrum," *Annalen der Physik*, vol. 4, 1901. 2

[6] "Infrared." Wikipedia, 2005.
http://en.wikipedia.org/wiki/Infrared. 3

[7] A. Rogalski, "Infrared detectors: Status and trends," *Progress in Quantum Electronics*, vol. 27, no. 2, pp. 59–210, 2003. xi, 7, 8

[8] G. L. Hansen, J. L. Schmit, and T. N. Casselman, "Energy gap versus alloy composition and temperature in $hg_{1-x}cd_xte$," *Journal of Applied Physics*, vol. 53, no. 10, pp. 7099–7101, 1982.
http://link.aip.org/link/?JAP/53/7099/1. 7

[9] H. V. Hayes, "A new receiver of radiant energy," *Review of Scientific Instruments*,

vol. 7, no. 5, pp. 202–204, 1936.
http://link.aip.org/link/?RSI/7/202/1. 8

[10] H. A. Zahl and M. J. E. Golay, "Pneumatic heat detector," *Review of Scientific Instruments*, vol. 17, no. 11, pp. 511–515, 1946.
http://link.aip.org/link/?RSI/17/511/1. 8

[11] M. J. E. Golay, "A pneumatic infra-red detector," *Review of Scientific Instruments*, vol. 18, no. 5, pp. 357–362, 1947.
http://link.aip.org/link/?RSI/18/357/1. 8

[12] McGraw-Hill Encyclopedia of Science and Technology Online.
http://www.accessscience.com. 8

[13] P. Muralt, "Micromachined infrared detectors based on pyroelectric thin films," *Reports on Progress in Physics*, vol. 64, no. 10, pp. 1339–1388, 2001.
http://stacks.iop.org/0034-4885/64/1339. 9

[14] P. G. Datskos, N. V. Lavrik, and S. Rajic, "Performance of uncooled microcantilever thermal detectors," *Review of Scientific Instruments*, vol. 75, no. 4, pp. 1134–1148, 2004.
http://link.aip.org/link/?RSI/75/1134/1. 9, 10

[15] T. W. Kenny, W. J. Kaiser, S. B. Waltman, and J. K. Reynolds, "Novel infrared detector based on a tunneling displacement transducer," *Applied Physics Letters*, vol. 59, no. 15, pp. 1820–1822, 1991.
http://link.aip.org/link/?APL/59/1820/1. 10

[16] T. Kenny, "Uncooled infrared imaging systems," in *Semiconductor and Semimetals* (D. D. Skatrud and P. W. Kruse, eds.), vol. 47, ch. 8, Academic Press, 1997. 10

[17] M. Foote, E. Jones, and T. Caillat, "Uncooled thermopile infrared detector linear arrays with detectivity greater than $10^9 cm.hz^{1/2}w^{-1}$," *IEEE Transactions on Electron Devices*, vol. 45, September 1998. 10

[18] A. Schaufelbhl, N. Schneeberger, U. Mnch, M. Waelti, O. Paul, O. Brand, H. Baltes, C. Menolfi, Q. Huang, E. Doering, and M. Loepfe, "Uncooled low-cost thermal imager

based on micromachined cmos integrated sensor array," *Journal Of Microelectromechanical Systems*, vol. 10, December 2001. 10

[19] Y. Zhao, M. Mao, R. Horowitz, A. Majumdar, J. Varesi, P. Norton, and J. Kitching, "Optomechanical uncooled infrared imaging system: Design, microfabrication, and performance," *Journal Of Microelectromechanical Systems*, vol. 11, april 2002. 10

[20] J. Tissot, "Ir detection with uncooled focal plane arrays. state of the art and trends," *Opto-Electronics Review*, vol. 12, no. 1, p. 105109, 2004. xi, 11

Chapter 2

Uncooled Bolometers for Thermal Imaging

Introduction

The Merriam-Webster dictionary entry for *bolometer* states:

> Etymology: From the Greek *bole*, ray and *metron*, measure.
> :A very sensitive thermometer whose electrical resistance varies with temperature and which is used in the detection and measurement of feeble thermal radiation and is especially adapted to the study of infrared spectra.

Although technically correct, this definition is incomplete because it does not explain how the presence of radiation leads to a change in temperature and electrical resistance. A more complete definition could be as follows: "A device that measures thermal radiation by converting said radiation into a temperature change and subsequently measuring the induced change in electrical resistance."

The bolometer was invented in 1878 by Samuel Pierpont Langley while he was studying radiation of the Sun. Langley's bolometer consisted of four strips of titanium arranged in a Wheatsone bridge. Two of the metal strips were painted black and exposed to radiation while the two others were covered. The signal could be read using a galvanometer. Langley claimed to be able to detect a cow within a quarter of a mile. Figure 2.1 shows a drawing of the first bolometer (http://earthobservatory.nasa.gov).

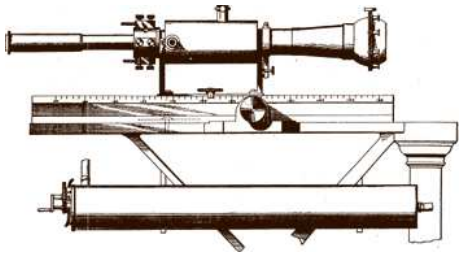

Figure 2.1: Langley's Bolometer With its Optics

.

2.1 Radiometry

To perform thermal imaging, we need to detect the thermal radiation coming from an object and we need to know the relationship between the detected radiation and the object temperature. Radiometry by definition is the science of radiation measurement. This section introduces several important radiometry definitions. We then lay out the equations governing the radiation exchange between a blackbody at a given temperature and a detector through a lens.

2.1.1 Radiant Flux

The radiant flux $\phi(W)$ emitted or received by a surface is the power of electromagnetic radiation it emits or receives.

2.1.2 Irradiance

The irradiance $E(W.m^{-2})$ of a surface is the amount of radiant flux it receives per unit area.

2.1.3 Radiance

The radiance $L(W.m^{-2}.sr^{-1})$ of a surface is defined as the amount of radiant flux it emits per unit of projected area and per unit of solid angle. This definition is better understood if placed in the context of radiation exchanges between two surfaces. Let us consider an infinitesimal element of area of a source dA_s having radiance L emitting light into a light cone $d\omega$. Let us call θ_s the angle between the surface dA_s and the direction of light propagation (Figure 2.2). Its *projected*, or *foreshortened*, *area* is defined as the

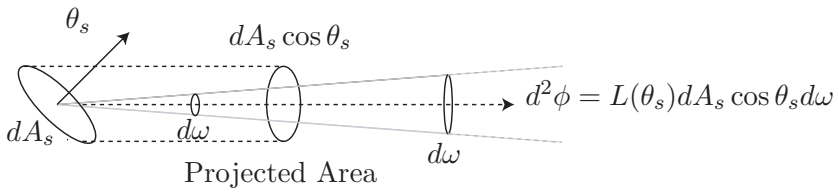

Figure 2.2: Concept of Radiance

projection of this area onto the plane which is normal to the direction of light propagation, i.e., $dA_s \cos\theta_s$. Let us now consider the light cone having an elemental solid angle $d\omega$ (Figure 2.2). Since the definition of radiance is the amount of radiant flux emitted by the source per unit projected area and per unit of solid angle, the radiant flux emitted by dA_s in the light cone subtended by $d\omega$ is

$$d^2\phi = L(\theta_s) dA_s \cos\theta_s d\omega. \tag{2.1}$$

2.1.4 Exitance

The exitance $M(W.m^{-2})$ of a surface is the total radiant flux it emits per unit area:

$$M \equiv \frac{d\Phi}{dA_s} = \int L(\theta_s) \cos\theta_s d\omega_d. \tag{2.2}$$

The spectral exitance of a surface is the radiant flux it emits per unit area and per unit wavelength:

$$M_\lambda \equiv \frac{d\Phi_\lambda}{dA_s} = \int L_\lambda(\theta_s) \cos\theta_s d\omega_d. \tag{2.3}$$

where the integrals is taken over an hemisphere.

2.1.5 Intensity

Intensity $I(W.sr^{-1})$ is the amount of radiant flux emitted per unit of solid angle:

$$I = \frac{d\phi}{d\omega} \tag{2.4}$$

$$= L(\theta_s) dA_s \cos\theta_s. \tag{2.5}$$

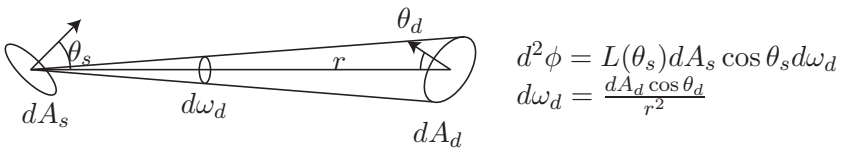

Figure 2.3: Radiation Exchange Between Two Infinitesimal Surfaces

2.1.6 Radiation Exchange Between Two Surfaces

Let us now consider the radiation exchange between a surface dA_s and a detector surface dA_d, with r the distance between the two surfaces, θ_s and θ_d the angle between the light propagation direction and the surface dA_s and dA_d, respectively (Figure 2.3).

As seen before from the definition of radiance we have

$$d^2\Phi = L(\theta_s)dA_s\cos\theta_s d\omega_d, \tag{2.6}$$

with $d\omega_d$ the solid angle subtended by dA_d from dA_s. Using the definitions in Figure 2.3 this can also be written

$$d^2\Phi = L(\theta_s)\frac{dA_s dA_d\cos\theta_s\cos\theta_d}{r^2} \tag{2.7}$$

and

$$d^2\Phi = L(\theta_s)dA_d\cos\theta_d d\omega_s, \tag{2.8}$$

with $d\omega_s$ the solid angle subtended by dA_s from dA_d.

2.1.7 Lambertian Surfaces

By definition, the radiance of a Lambertian surface $L(\theta_s)$ is independent of θ_s:

$$L(\theta_s) = L. \tag{2.9}$$

Let us consider an elemental Lambertian surface dA_s located in the center of a receiving hemisphere of radius r. By definition, the exitance M of the surface dA_s is the total amount of radiant flux emitted per unit of area. In the following the subscript letter, h represents the hemisphere. Because the source is in the center of the hemisphere, we have $\theta_h = 0$ for

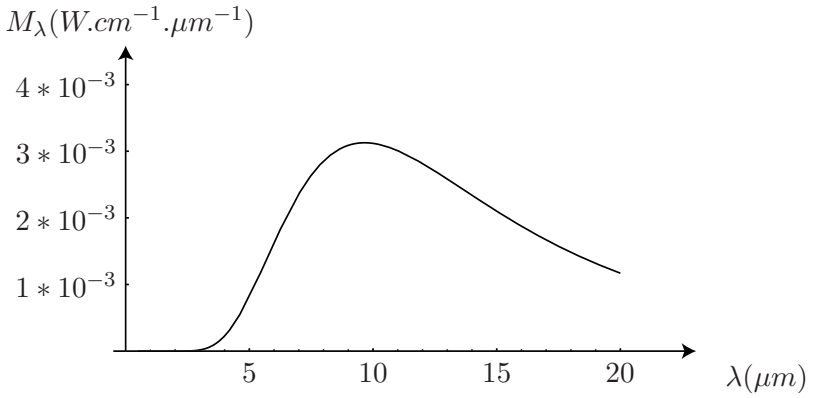

Figure 2.4: Spectral Exitance of a Blackbody at 300^oK

each elemental receiving hemisphere area. From Equation 2.6, we get

$$\begin{aligned} M &= \int_{\Omega_h} L\cos\theta_s d\omega_h \\ &= \int_{S_h} L\cos\theta_s \frac{dS_h}{r^2} \\ &= \int_{\theta_s=0}^{\pi/2}\int_{\varphi=0}^{2\pi} L\sin\theta_s\cos\theta_s d\varphi d\theta_s \\ M &= \pi L. \end{aligned} \tag{2.10}$$

2.2 Thermal Imaging

2.2.1 Blackbody Radiation

2.2.1.1 Definition

A black body is a Lambertian source having spectral exitance given by Planck's blackbody radiation equation:

$$M_\lambda(T,\lambda) = \frac{2\pi hc^2}{\lambda^5(e^{(hc/\lambda kT)}-1)}(W.m^{-3}). \tag{2.11}$$

Figure 2.4 shows the exitance spectra of a blackbody at $T = 300^oK$.

Material	Emissivity
Aluminum foil	0.04
Steel (polished)	0.07
Brick	0.93
Glass	0.95
Human skin	0.98
Water	0.96
Wood	0.9
Concrete	0.95

Table 2.1: Emissivity of Various Materials

2.2.1.2 Radiance

From Equation 2.10 the spectral radiance is simply

$$L_\lambda(T,\lambda) = \frac{M(T,\lambda)}{\pi}(W.m^{-3}.sr^{-1}). \tag{2.12}$$

Real materials always have an exitance smaller than the ideal blackbody, given by

$$L_\lambda(T,\lambda) = \epsilon_\lambda \frac{M(T,\lambda)}{\pi}(W.m^{-3}.sr^{-1}), \tag{2.13}$$

where $\epsilon_\lambda < 1$ is the material spectral emissivity. Materials for which the spectral emissivity is independent of the wavelength (i.e., $\epsilon_\lambda = \epsilon$) are called graybodies. Although these are only hypothetical since no material emits at *all wavelengths* of the electromagnetic spectrum, some materials have spectral emissivities that can be considered constant across wavelengths of practical interest (e.g., LWIR). Table 2.1 shows the emissivities of various materials.

2.2.1.3 Exitance

The total exitance of a blackbody is given by the Stefan-Boltzmann's law:

$$M(T) = \int_0^{+\infty} M_\lambda(T,\lambda)d\lambda = \sigma_b T^4, \tag{2.14}$$

where $\sigma_b = 5.607 * 10^{-8} W.m^{-2}K^{-4}$ is the Stefan-Boltzmann constant.

2.2.1.4 Wien's Displacement Law

The wavelength of maximum spectral excitance λ_{max} of a blackbody depends on its temperature T. From Equation 2.11, λ_{max} and T can be shown to satisfy the relation

$$\lambda_{max}T = \frac{hc}{5k(1-\exp^{-\frac{hc}{k\lambda_{max}T}})}, \tag{2.15}$$

which can be solved numerically to give

$$\lambda_{max}T = 2.8978 * 10^{-3}(m.K),$$

or in a more convenient form

$$\lambda_{max}(\mu m) = \frac{2897.8}{T(K)}. \tag{2.16}$$

Therefore, objects close to room temperature ($T \sim 300^oK$) radiate mostly at wavelengths within the $8\mu m - 14\mu m$ atmospheric window (LWIR).

2.2.2 Radiation Transfer Between an Object and a Detector

To remotely measure the temperature of an object or a scene one must collect the radiation it emits on a detector. In this section, we derive the expression of the irradiance on a detector E_d due to an object having a spectral exitance $M_{\lambda,o}$ when the radiation coming from the object is focused on the detector using a lens of focal length f and of diameter D. Figure 2.5 shows the typical imaging system configuration. f is the focal distance of the lens , z_o is the distance between the object and the lens, and z_i is the distance between the image (or detector) and the lens.

First we calculate the spectral radiant flux $\Phi_{\lambda,o\rightarrow l}$ being transferred from the object surface A_o to the lens surface A_l. Assuming the there are no losses in the lens, this spectral radiant flux will then be incident on the detector surface A_d. Figure 2.6 shows the geometry definitions used for this calculation.

From Equation 2.1 we get

$$\Phi_{\lambda,o\rightarrow l}(T,\lambda) = \int_{A_o}\int_{\Omega_l} L_{\lambda,o}(T,\lambda)\cos\theta d\omega_l dA_o$$

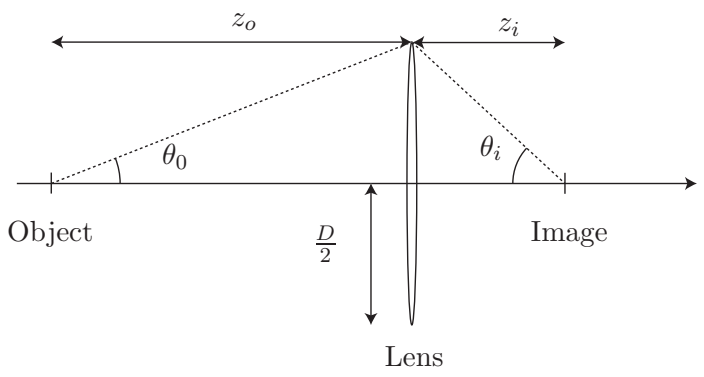

Figure 2.5: Typical Imager

$$= A_o L_{\lambda,o}(T,\lambda) \int_{\Omega_l} \cos\theta d\omega_l,$$

where $d\omega_l$ is the elemental solid angle.

From Figure 2.6, we make the appropriate substitutions

$$\begin{aligned}
\theta &= \theta_l, \\
d\omega_l &= \frac{dA_l}{r^2}\cos\theta, \\
r &= \frac{z_o}{\cos\theta}, \\
r' &= z_o \tan\theta, \\
dA_l &= r' d\varphi dr' \\
&= \frac{z_o^2 \tan\theta}{\cos^2\theta} d\varphi d\theta, \\
d\omega_l &= \sin\theta d\varphi d\theta, \\
\Phi_{\lambda\, o\to l}(T,\lambda) &= A_o L_{\lambda,o}(T,\lambda) \int_0^{2\pi}\int_0^{\theta_0} \sin\theta\cos\theta d\theta d\varphi \\
&= A_o \pi L_{\lambda,o}(T,\lambda)\sin^2\theta_0. \qquad (2.17)
\end{aligned}$$

For or a Lambertian object we can substitute Equation 2.10 into Equation 2.17 to get

$$\Phi_{\lambda,o\to l}(T,\lambda) = A_o M_{\lambda,o}(T,\lambda)\sin^2\theta_0. \qquad (2.18)$$

From Abbe's sine condition (also called the optical sine theorem)[1] we have

$$A_d \sin^2\theta_i = A_o \sin^2\theta_o.$$

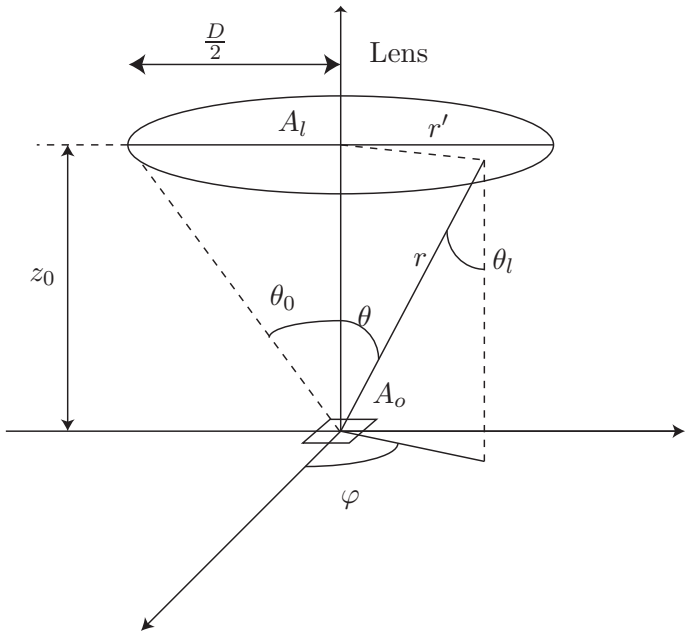

Figure 2.6: Imaging System Geometry Definitions

Therefore, the spectral radiant flux incident on the detector is

$$\begin{aligned}
\Phi_{\lambda,o\to d}(T,\lambda) &= A_d M_{\lambda,o}(T,\lambda)\sin^2\theta_i \\
&= A_d M_{\lambda,o}(T,\lambda) NA^2 \\
\Phi_{\lambda,o\to d}(T,\lambda) &= \frac{A_d M_{\lambda,o}(T,\lambda)}{4F^2},
\end{aligned} \tag{2.19}$$

and the irradiance on the detector surface is

$$\begin{aligned}
E_{\lambda,d}(T,\lambda) &\equiv \frac{\Phi_{\lambda,o\to d}(T,\lambda)}{A_d} \\
&= \frac{M_{\lambda,o}(T,\lambda)}{4F^2},
\end{aligned} \tag{2.20}$$

where

$$NA \equiv \sin\theta_i \text{ (Numerical Aperture)} \tag{2.21}$$

$$F \equiv \frac{1}{2NA} = \frac{1}{2\sin\theta_i} \text{ (F-Number)}. \tag{2.22}$$

Equation 2.19 is well know among photographers (in fact it is also called the camera equation) because it relates the irradiance on a photographic film to the scene radiance and

camera F-number. For an object located at infinity ($z_0 = f$) and if $f \gg D$, we have

$$\begin{aligned} F &= \frac{1}{D}\sqrt{\frac{D^2}{4} + f^2} \\ &\simeq \frac{f}{D}. \end{aligned}$$

In the literature, the focal ratio f/D and F are often considered to be identical and are simply referred to as "the F-number" or "f/#". However, this approximation leads to significant errors when F is comparable to 1.

2.2.3 Radiation Transfer Between a Blackbody and a Detector

If a blackbody at temperature T radiates to a detector having an area A_d through an optical system having F-number F, the radiant flux on the detector in the $[\lambda_1 - \lambda_2]$ band is given by integrating Equation 2.19

$$\begin{aligned} \Phi_{[\lambda_1,\lambda_2]}(T) &= \int_{\lambda_1}^{\lambda_2} \Phi_\lambda(T,\lambda)d\lambda \\ &= \frac{A_d}{4F^2}\int_{\lambda_1}^{\lambda_2} M(\lambda,T)d\lambda \\ &= \frac{A_d}{4F^2}\int_{\lambda_1}^{\lambda_2} \frac{2\pi hc^2}{\lambda^5(e^{(hc/\lambda kT)}-1)}d\lambda. \end{aligned} \tag{2.23}$$

2.3 Bolometer Theory

2.3.1 Electrical-Thermal Analogy

To study the behavior of thermal systems in general and bolometers in particular, it is very convenient to use the electro-thermal analogy. To find the thermal equivalent of electrical quantities, we start by noting that in electronics one studies the behavior and motion of electrons, i.e., electric charge. In thermal engineering we are interested in the behavior of thermal energy instead. Therefore, the first step in building the electro-thermal analogy is stating that electric charge and thermal energy are equivalent:

$$\begin{aligned} q(C) &\Leftrightarrow E(J) \\ \text{Charge} &\Leftrightarrow \text{Thermal Energy} \end{aligned}$$

Electric current is the amount of charge that passes through a section per unit of time. The thermal equivalent is then energy per unit of time, i.e., power:

$$\begin{aligned} I = \frac{dq}{dt}(A) &\Leftrightarrow P = \frac{dE}{dt}(W) \\ \text{Electric Current} &\Leftrightarrow \text{Thermal Power.} \end{aligned}$$

The reason why electric charge flows from one region in space to another region in space is the presence of a potential gradient (electric field). Equivalently, the reason why thermal energy flows from one region in space to another region in space is the presence of a temperature gradient. Therefore, the thermal equivalent of electrostatic potential is temperature:

$$\begin{aligned} V(V) &\Leftrightarrow T(K) \\ \text{Electric Potential} &\Leftrightarrow \text{Temperature.} \end{aligned}$$

Using the same kind of reasoning, one can easily find the thermal equivalents of other electrical quantities such as current density, conductivity, conductance, and capacitance.

$$\begin{aligned} J = \frac{dI}{dS}(A.m^{-2}) &\Leftrightarrow Q = \frac{dP}{dS}(W.m^{-2}) \\ \text{Current Density} &\Leftrightarrow \text{Thermal Energy Flux,} \\ J = -\sigma\nabla V(A.m^{-2}) &\Leftrightarrow Q = -\kappa\nabla T(W.m^{-2}) \\ \text{Electrical Conduction} &\Leftrightarrow \text{Thermal Conduction,} \\ \sigma(A.V^{-1}.m^{-1}) &\Leftrightarrow \kappa(W.K^{-1}.m^{-1}) \\ \text{Electrical Conductivity} &\Leftrightarrow \text{Thermal Conductivity,} \\ G = \frac{L}{\sigma W t} &\Leftrightarrow G_{th} = \frac{L}{\kappa W t} \\ \text{Electrical Conductance} &\Leftrightarrow \text{Thermal Conductance,} \\ I = C\frac{dV}{dt} &\Leftrightarrow P = C_{th}\frac{dT}{dt} \\ \text{Electrical Capacity} &\Leftrightarrow \text{Thermal Capacity, and} \\ C[C.V^{-1}] &\Leftrightarrow C_{th}[J.K^{-1}] \\ \text{Electrical Capacitance} &\Leftrightarrow \text{Heat Capacity.} \end{aligned}$$

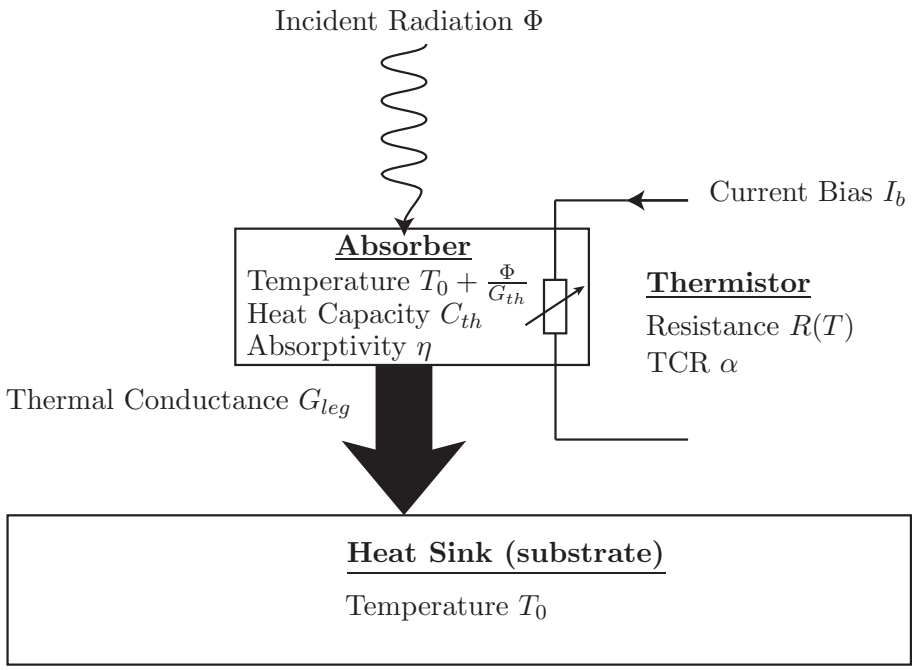

Figure 2.7: Bolometer Principle

2.3.2 Structure

Figure 2.7 shows a simplified bolometer structure. An absorber is linked to a heat sink through a low thermal conductance G_{leg}. As it absorbs an incident radiant flux $\Phi(W)$, the temperature increases. By measuring the resistance of a thermistor placed on the absorber, one can calculate the amount of absorbed radiant flux.

2.3.3 Model

Using the electrical-thermal analogy introduced in Section 2.3.1, we can draw the electrical equivalent of the bolometer thermal circuit, which is a classical first-order, RC-type circuit (Figure 2.8). The losses through radiation are modeled with a thermal conductance G_{rad}. The expression of G_{rad} is found by taking the derivative of the total exitance of a blackbody around room temperature (Equation 2.14) and multiplying by the bolometer area $2 * A_d$ (because both the top surface and the bottom surface of the bolometer are radiating):

$$G_{rad} = 2A_d \frac{d\eta\sigma T^4}{dT} = 8A_d\sigma T^3. \tag{2.24}$$

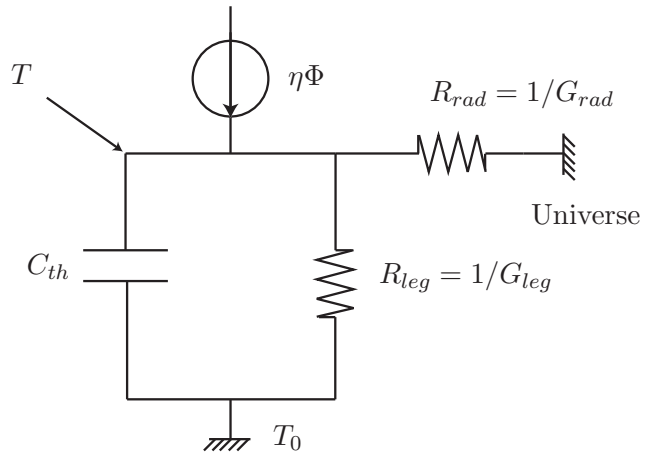

Figure 2.8: Bolometer Equivalent Electric Circuit

The total thermal conductance G_{th} is given by

$$G_{th} = G_{leg} + G_{rad}. \tag{2.25}$$

The radiation conductance is often neglected, however it should be noted that if the thermal conductance to the substrate G_{leg} approaches the value of the radiation conductance G_{rad}, then both should be taken into account.

2.3.3.1 Static Behavior

In steady state, we have

$$\begin{aligned} T(\Phi) &= T_0 + \frac{\eta\Phi}{G_{th}} \\ \Delta T(\Phi) &\equiv T(\Phi) - T_0. \end{aligned}$$

Therefore, if the thermistor has a resistance R_0 at room temperature and a Temperature Coefficient of Resistance (TCR) α, we have

$$\begin{aligned} R(\Phi) &= R_0(1 + \alpha\Delta T(\Phi)) \\ &= R_0(1 + \alpha\frac{\eta\Phi}{G_{th}}) \\ \Delta R(\Phi) &= R_0\alpha\frac{\eta\Phi}{G_{th}}, \end{aligned}$$

and the voltage signal ΔV measured when biasing the bolometer with a current I_b is [1]

$$\Delta V(\Phi) \quad = \quad I_b R_0 \alpha \frac{\eta \Phi}{G_{th}}. \tag{2.26}$$

Equation 2.26 leads to the definition of the voltage responsivity $\Re$:

$$\Re(V.m^{-1}) \quad \equiv \quad \frac{\Delta V(\Phi)}{\Phi} = \frac{\alpha \eta R_0 I_b}{G_{th}}. \tag{2.27}$$

As one would naturally expect from Figure 2.7, $\Re$ is high when:

1. The absorptivity is high (most of the incoming radiant flux is absorbed and converted to temperature rise).

2. The thermal conductance is small (good absorber insulation, high temperature rise for a given absorbed radiant flux).

3. The TCR of the thermistor is big (big change in thermistor resistance for a given change in absorber temperature).

4. I_b is high (big change in signal voltage for a given change in thermistor resistance).

2.3.3.2 Dynamic Behavior

Let us define

$$\overline{\Phi}(j\omega) \quad \equiv \quad \Phi_0(\omega) e^{j\omega t} \tag{2.28}$$

and

$$\overline{\Delta T}(j\omega) \quad \equiv \quad \Delta T \Phi_0(\omega) e^{j(\omega t + \varphi)}. \tag{2.29}$$

We can write the expression of the thermal transfer function (which, using the electrothermal analogy of Section 2.3.1 is equivalent to a complex impedance):

$$H_{th}(j\omega) \equiv \frac{\overline{\Delta T}(j\omega)}{\eta \overline{\Phi}(j\omega)} \quad = \quad \frac{1}{G_{th}(1 + j\omega\tau_{th})}. \tag{2.30}$$

[1] We assume for now that the temperature of the absorber is not affected by the Joulean heating resulting from I_b.

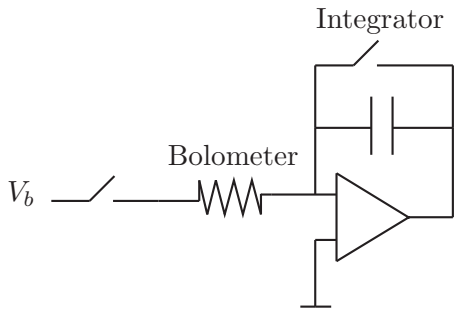

Figure 2.9: Simple Bolometer Readout Circuit

It follows that

$$\Delta T(\omega) = \frac{\eta \Phi_0}{G_{th}\sqrt{1+(\omega\tau_{th})^2}},$$

where τ_{th}, the thermal time constant of the bolometer, is given by

$$\tau_{th} \equiv \frac{C_{th}}{G_{th}}. \tag{2.31}$$

From Equation 2.31, it is obvious that there is a trade-off between D.C. responsivity and thermal time constant. In fact, if one wants to increase $\Re$ by decreasing G_{th} while keeping τ_{th} unchanged, C_{th} has to be decreased by the same amount as G_{th}.

2.3.4 Signal Readout

Figure 2.3.4 shows a simplified bolometer readout circuit in a voltage bias configuration. Typically, a voltage pulse is applied for a duration τ_{pulse}, and the resulting current is integrated. The result of the integration is multiplied by the appropriate coefficient to give a value of the average bolometer current. The power dissipated by Joulean heating during readout will cause a temperature increase on the bolometer. Because the thermal conductivity from bolometer to substrate is low *by design*, this temperature rise might be significant. If we assume that the α remains constant during the readout, the temperature $\Delta T(t)$ must satisfy

$$\begin{aligned} R(\Delta T){I_b}^2 &= C_{th}\frac{\Delta T}{dt} + G_{th}\Delta T, \\ R_0(1+\alpha\Delta T){I_b}^2 &= C_{th}\frac{\Delta T}{dt} + G_{th}\Delta T, \end{aligned}$$

and using $\overline{\Delta T}(j\omega)$ as defined in Equation 2.29

$$\begin{aligned}\overline{\Delta T}(j\omega) &= \frac{R_0 {I_b}^2}{(G_{th} - R_0\alpha {I_b}^2) + jC_{th}\omega} \\ &= \frac{R_0 {I_b}^2}{G_{\text{eff}} + jC_{th}\omega} \\ &= \frac{R_0 {I_b}^2}{G_{\text{eff}}}\frac{1}{1 + j\omega\tau_{\text{eff}}}, \end{aligned} \tag{2.32}$$

with

$$G_{\text{eff}} = G_{th} - R_0\alpha {I_b}^2 \tag{2.33}$$

$$\tau_{\text{eff}} = \frac{C_{th}}{G_{eff}} = \frac{C_{th}}{G_{th} - R_0\alpha {I_b}^2}. \tag{2.34}$$

Equations 2.33 and 2.34 show that the bolometer temperature still exhibits a first-order frequency response. However, depending on the sign of α, the effective thermal constant can be greater or lower than the intrinsic thermal conductance. The effective time constant will be lower or greater, respectively. This is due to the fact that for a constant current, the power injected in the bolometer varies:

$$\Delta T(t) = \frac{R_0 {I_b}^2}{G_{\text{eff}}}\Big(1 - \exp(-\frac{t}{\tau_{eff}})\Big). \tag{2.35}$$

Equations 2.33 and 2.34 show that if α is positive (as would be the case for a metallic thermistor), there exists a critical biasing current I_{crit} for which G_{eff} and τ_{eff} will become negative:

$$I_{crit} = \sqrt{\frac{G_{th}}{R_0\alpha}}. \tag{2.36}$$

If $I_b > I_{crit}$, the bolometer will experience thermal runaway, as Equation 2.35 clearly shows. Such runaway is very likely to destroy or damage the bolometer.[2]

For $t \ll \tau_{eff}$ we have, from Equation 2.35,

$$\begin{aligned}\Delta T(t) &\simeq \frac{R_0 {I_b}^2}{G_{\text{eff}}}\frac{t}{\tau_{eff}} \\ &\simeq \frac{R_0 {I_b}^2}{C_{th}} \end{aligned} \tag{2.37}$$

Therefore, if $\tau_{pulse} \ll \tau_{eff}$, the temperature $\Delta T_{\tau_{pulse}}$ at the end of the integration pulse of

[2] However, we assumed that α was independent of T, which might not be true, especially at high temperatures.

length τ_{pulse} is

$$\Delta T_{pulse} = \frac{R_0 I_b^2 \tau_{pulse}}{C_{th}}. \tag{2.38}$$

Equation 2.38 shows that even if α is negative and/or thermal runaway is avoided, the integration time τ_{pulse} and bias current I_b must be chosen so that the temperature increase ΔT_{pulse} is low enough to avoid damaging the bolometer. Finally, as will be shown in Section 2.3.5, τ_{pulse} will affect the bolometer noise performance.

2.3.5 Noise

There are several uncorrelated sources to bolometer noise: the Johnson noise (or thermal noise), the $1/f$ noise (also called flicker noise), and the background noise. The $1/f$ noise depends on the material used and on the geometry of the device. In this section, we discuss these different noise contributions in the case of the timed-integration readout circuit discussed in Section 2.3.4.

2.3.5.1 Readout Circuit Noise Bandwidth

The total noise at the output of a circuit having transfer function $H(f)$ and input power noise spectral density $S_i(f)$ is given by

$$\begin{aligned} < {V_n}^2 > &= \int_0^{+\infty} S_o(f) df \\ &= S_i \int_0^{+\infty} |H(f)|^2 df \\ &= S_i B, \end{aligned} \tag{2.39}$$

where B is the noise bandwidth defined by

$$B \equiv \int_0^{+\infty} |H(f)|^2 df.$$

The readout circuit described in Section 2.3.4 averages the signal over an integration time τ_{pulse}. Its impulse response $h(t)$ is

$$h(t) = \begin{cases} 0 \text{ for } t < 0 \\ \frac{1}{\tau_{pulse}} \text{ for } 0 \leq t \leq \tau_{pulse} \\ 0 \text{ for } t > \tau_{pulse} \end{cases}$$

and its transfer function $H(f)$ is

$$H(f) = e^{-j\pi f \tau_{pulse}} \frac{\sin \pi f \tau_{pulse}}{\pi f \tau_{pulse}}. \tag{2.40}$$

The noise bandwidth of the readout circuit can be calculated by integrating Equation 2.40, but it is easier to calculate it using Parseval's relation:

$$\begin{aligned} B &= \int_0^{+\infty} \left(\frac{\sin \pi f \tau_{pulse}}{\pi f \tau_{pulse}} \right)^2 df \\ &= \frac{1}{2} \int_{-\infty}^{+\infty} |H(f)|^2 df \\ &= \frac{1}{2} \int_{-\infty}^{+\infty} h(t)^2 dt \\ &= \frac{1}{2} \int_0^{\tau_{pulse}} \frac{1}{{\tau_{pulse}}^2} dt \\ B &= \frac{1}{2\tau_{pulse}}. \end{aligned} \tag{2.41}$$

2.3.5.2 Johnson Noise

Due to its resistive nature, the bolometer exhibits Johnson (thermal) Noise . J.B. Johnson experimentally found that the noise power spectral density in a resistor of resistance R_0 given by [2]

$$S_j = 4kTR_0. \tag{2.42}$$

where k is the boltzmann constant and R_0 is the electrical resistance of the bolometer at room temperature. Equation 2.42 was proven theoretically by Harry Nyquist[3].[3]

When the bolometer signal is read by the integrated and dump circuit presented in Section 2.3.4, the Johnson noise at the output is found by combining Equation 2.42, Equation

[3] In fact, Nyquist's paper appear right after Johnson's in the same issue of the same journal [2, 3].

2.39, and Equation 2.41:

$$\sqrt{< V_j^2 >} = \sqrt{\frac{2kTR_0}{\tau_{pulse}}}. \tag{2.43}$$

We conclude this section on Johnson noise by showing that the Johnson noise voltage can be expressed as a function of the temperature rise the bolometer experiences during the readout/integration pulse (see Section 2.3.4). Substituting Equation 2.38 into Equation 2.43 gives

$$\sqrt{< V_j^2 >} = V_b\sqrt{\frac{2kT}{\Delta T_{pulse}C_{th}}}. \tag{2.44}$$

This important result shows that to minimize the Johnson noise contribution to the total bolometer noise it is desirable to use materials that can handle a high temperature increase during readout.

2.3.5.3 $1/f$ Noise

While measuring noise in vacuum tubes, Johnson found that not only was there a white noise (the thermal noise discussed above) but also another noise component which was stronger at low frequencies, which he failed to explain [4]. This noise is called $1/f$ noise, or flicker noise, and is found in many physical systems, electrical and others[5].

The $1/f$ noise (or flicker noise) power spectral density of a resistor is given by

$$S_f(f) = \frac{KV_b^b}{f^a} \tag{2.45}$$

where V_b is the bias voltage across the resistor, K is a constant that depends on the material used as well as on the geometry of the resistor, a is a constant that depends on the material and which is usually found to be close to 1, and b is a constant that is usually found to be between 0.5 and 2 [6]. In many cases, the $1/f$ noise is equal to (or approximated by)

$$S_f(f) = \frac{KV_b^2}{f}. \tag{2.46}$$

Despite what is believed by some, no resistor is free of $1/f$ noise. However, the magnitude of this noise depends on the resistor material and geometry.

In a famous paper published in 1969 [7], F.N. Hooge proposed a "universal" relation

$$K = \frac{\alpha_H}{nV}, \tag{2.47}$$

where n is the charge carrier density of the material, V is the total volume of the resistor, and α_H is an empirical constant depending on the resistor material. Some measurements of α_H are collected in [8]. It should be noted that if $1/f$ noise actually follows Equation 2.47, then for a material with fixed sheet resistance (i.e., fixed thickness and fixed resistivity) a "small" square will have less noise than a "big" square, even though their Johnson noise will be identical. Such a volume dependence was reported for VOx (vanadium oxide) films and p-nc-SiC:H films in [9] and [10] respectively. However, little literature is available regarding $1/f$ noise in materials, and authors often cite values for K in materials without mentioning the volume of the resistors considered.

We want to calculate the total noise in a pulsed-bias bolometer with integration time τ_{pulse}. In many publications this noise power is calculated using the equation

$$< {V_f}^2 > \;\; = \;\; \int_{f_1}^{B} S_f(f) df,$$

leading to a noise power

$$< {V_f}^2 > \;\; = \;\; K V_b^2 \ln \frac{B}{f_1} = K V_b^2 \ln \frac{1}{2 f_1 \tau_{pulse}}. \tag{2.48}$$

where B is the noise bandwidth and f_1 is an arbitrary frequency chosen to avoid the divergence of S_f at $f = 0$. However, Equation 2.48 is incorrect and is due to a common misunderstanding of the definition of noise bandwidth. It is true that the total thermal noise is given by

$$< {V_j}^2 > \;\; = \;\; \int_{0}^{B} Sj(f) df, \tag{2.49}$$

but only because $S_j(f) = S_j$. When a noise power spectral density depends on frequency, the concept of noise bandwidth cannot be used. The correct expression for the $1/f$ noise

power at the output of the integrating readout circuit is

$$\begin{aligned}
< {V_f}^2 > &= \int_{f_1}^{+\infty} |H(f)|^2 \frac{{KV_b}^2}{f} df \\
&= \int_{f_1}^{+\infty} \Big(\frac{\sin \pi f \tau_{pulse}}{\pi f \tau_{pulse}}\Big)^2 \frac{{KV_b}^2}{f} df \\
&= {KV_b}^2 \int_{\pi f_1 \tau_{pulse}}^{+\infty} \frac{\sin^2 x}{x^3} dx.
\end{aligned}$$

We define $J_{a,b}$ as

$$\begin{aligned}
J_{a,b} &= \int_a^b \frac{\sin^2 x}{x^3} dx \\
&= \int_a^b \frac{1-\cos 2x}{2x^3} dx \\
&= \Big[\frac{\cos 2x - 1}{4x^2}\Big]_a^b + \frac{1}{2}\int_a^b \frac{\sin 2x}{x^2} dx \\
&= \Big[\frac{\cos 2x - 1}{4x^2}\Big]_a^b - \Big[\frac{\sin 2x}{2x}\Big]_a^b + \int_a^b \frac{\cos 2x}{x} dx \\
&= \Big[\frac{\cos 2x - 1}{4x^2}\Big]_a^b - \Big[\frac{\sin 2x}{2x}\Big]_a^b + \int_{2a}^{2b} \frac{\cos u}{u} du \\
&= \Big[\frac{\cos 2x - 1}{4x^2}\Big]_a^b - \Big[\frac{\sin 2x}{2x}\Big]_a^b + Ci(2b) - Ci(2a) \\
&= \frac{\cos 2b - 1}{4b^2} - \frac{\cos 2a - 1}{4a^2} - \frac{\sin 2b}{2b} + \frac{\sin 2a}{2a} + Ci(2b) - Ci(2a),
\end{aligned}$$

where $Ci(x)$ is the cosine integral defined by

$$Ci(x) \equiv -\int_x^{+\infty} \frac{\cos u}{u} du. \tag{2.50}$$

then

$$\begin{aligned}
< {V_f}^2 > &= {KV_b}^2 \int_{\pi f_1 \tau_{pulse}}^{+\infty} \frac{\sin^2 x}{x^3} dx \\
&= {KV_b}^2 J_{\pi f_1 \tau_{pulse}, +\infty} \\
< {V_f}^2 > &= {KV_b}^2 \Big(\frac{1-\cos 2\pi f_1 \tau_{pulse}}{4(\pi f_1 \tau_{pulse})^2} + \frac{\sin 2\pi f_1 \tau_{pulse}}{2\pi f_1 \tau_{pulse}} - Ci(2\pi f_1 \tau_{pulse})\Big).
\end{aligned} \tag{2.51}$$

Equation 2.51 can be simplified using the fact that in most cases $2\pi f_1 \tau_{pulse} \ll 1$.

The first-order series expansion of $Ci(x)$ is [11]

$$Ci(x) = \gamma + \ln(x) + O(x)^2, \tag{2.52}$$

where $\gamma = 0.58$ is the Euler-Mascheroni constant. Therefore, the first-order series expansion of $< {V_f}^2 >$ is

$$< {V_f}^2 >= K{V_b}^2\Big(\frac{3}{2} - \gamma - \ln(2\pi f_1 \tau_{pulse}) + O(2\pi f_1 \tau_{pulse})^2\Big). \tag{2.53}$$

Equation 2.53 shows that Equation 2.48 overerestimates the $1/f$ noise power by

$$-K{V_b}^2(\frac{3}{2} - \gamma - \ln \pi) \simeq 0.22K{V_b}^2.$$

2.3.5.4 Temperature Fluctuation Noise and Background Noise

An abbreviated and adapted derivation of thermal fluctuation noise and background noise based on the more general case in [12] is given below. The mean-square fluctuations in energy of a system with thermal capacity C_{th} is

$$< \Delta E^2 > \quad = \quad kT^2 C_{th}. \tag{2.54}$$

This random fluctuation of the energy stored in the bolometer will induce a random fluctuation in bolometer temperature, which in turn will lead to a random fluctuation of the bolometer voltage, i.e., a *temperature fluctuation voltage noise*.

The bolometer temperature and its stored energy are linked through

$$\Delta E = C_{th} \Delta T \tag{2.55}$$

From Equation 2.54 and Equation 2.55, the mean-square temperature fluctuation is found to be

$$< {\Delta T_{TF}}^2 >= \frac{< \Delta E^2 >}{{C_{th}}^2} = \frac{kT^2}{C_{th}}. \tag{2.56}$$

Let us assume that this temperature fluctuation is due to a fluctuation in radiant flux Φ_{TF} and that the power spectral density $S_{\Phi_{TF}}$ of Φ_{TF} is independent of frequency. We can write

$$S_{\Phi_{TF}}(f) = S_0.$$

Therefore,

$$< {\Delta T_{TF}}^2 >= \int_0^{+\infty} S_0 \eta^2 |H_{th}(j2\pi f)|^2 df,$$

where H_{th} is the thermal transfer function defined in Equation 2.30:

$$\begin{aligned} < \Delta T_{TF}{}^2 > &= \frac{S_0 \eta^2}{G_{th}{}^2} \int_0^{+\infty} \frac{1}{1+(2\pi f \tau_{th})^2} df \\ < \Delta T_{TF}{}^2 > &= \frac{S_0 \eta^2}{4 G_{th} C_{th}}. \end{aligned} \tag{2.57}$$

Combining Equation 2.56 and Equation 2.57, we get

$$S_0 = \frac{4kT^2 G_{th}}{\eta^2}. \tag{2.58}$$

Using the $\Delta V = \alpha V_b \Delta T$, the power spectral density of the temperature fluctuation voltage noise can be written

$$S_{TF}(f) = \alpha^2 V_b{}^2 S_0 \eta^2 |H_{th}(j2\pi f)|^2 = \frac{4kT^2 \alpha^2 V_b{}^2}{G_{th}} \frac{1}{1+(2\pi f \tau_{th})^2}. \tag{2.59}$$

However, if the frequencies of interest are much higher than $1/2\pi\tau_{th}$, the total voltage noise can be approximated by

$$\sqrt{< V_{TF}{}^2 >} = \alpha V_b \sqrt{\frac{kT^2}{C_{th}}} \tag{2.60}$$

(which can also be found using Equation 2.56).

As noted in [12], if most of the heat loss from the bolometer is due to radiation, G_{th} reduces to the radiation thermal conductivity $G_{rad} = 8\eta A_d \sigma_b T^3$ and the temperature fluctuation noise identifies with the background noise, i.e., the noise due to fluctuations in the rate of arrival of photons on the bolometer.

2.3.6 Noise-Equivalent Power

The noise equivalent power (NEP) of a bolometer is defined as the amount of radiant flux incoming on the bolometer that would lead to a voltage signal equivalent to the noise power:

$$NEP \equiv \frac{V_n}{\Re} = \frac{\sqrt{V_j^2 + V_f^2 + V_{TF}^2}}{\Re}. \tag{2.61}$$

2.3.7 Detectivity

The detectivity D^*, sometimes called "D star", is a figure of merit that normalizes performance to the square root of area and bandwidth.

$$D^* \equiv \frac{\Re\sqrt{BA_d}}{V_n}, \tag{2.62}$$

where A is the area of the detector and B is the bandwidth of the bolometer/readout system. The bandwidth of the measurement should also be taken into account because for any noise power spectral density one could theoretically reduce the total noise by reducing the bandwidth (e.g., by using an integrator with an arbitrarily long integration time). However, as noted in [13], detectivity is not a good figure of merit for thermal detectors (such as bolometers) or thermal imagers. The detectivity was originally defined for photon detectors. The reason for taking the area A_d into account in the detectivity is the fact that in such detectors the dominating noise power (usually generation-recombination noise) is proportional to the detector area. This is not the case for thermal detectors. In fact, if one assumes that Hooge's formula for $1/f$ noise holds (Equation 2.47), the noise power is *inversely* proportional to the area (for constant thickness).

Some authors use the following alternative definition:

$$D^{*\prime} \equiv \Re\sqrt{\frac{A_d}{S_n}}, \tag{2.63}$$

where S_n is the total noise power spectral density. If bolometer noise is dominated by Johnson noise or temperature fluctuation noise, then $V_n = \sqrt{S_n B}$ and the two definitions are equivalent. However when $1/f$ noise is non-negligible, using the alternative definition overestimates the bolometer performance.

2.3.8 Noise Equivalent Temperature Difference

The most relevant figure of merit for bolometers used for thermal imaging is the Noise-Equivalent Temperature Difference (NETD). It is the smallest temperature change on a target that one can measure using said bolometer. Quantitatively, the NETD is defined as the temperature difference on a blackbody target that will lead to a signal-to-noise ratio of 1.

To calculate the NETD of a bolometer, we start by calculating the change in radiant flux the bolometer will receive when the target temperature changes. The change in radiant flux falling on the detector per ^oK change on the source is found by differentiating Equation 2.23:

$$\begin{aligned}
\frac{d\Phi_{\lambda_1-\lambda_2}}{dT}(W.K^{-1}) &= \int_{\lambda_1}^{\lambda_2} \frac{d\Phi_\lambda(T,\lambda)}{dT} d\lambda \\
&= \frac{A_d}{4F^2} \int_{\lambda_1}^{\lambda_2} \frac{M(\lambda,T)}{dT} d\lambda \\
&= \frac{A_d}{4F^2} \int_{\lambda_1}^{\lambda_2} M(\lambda,T) \frac{hce^{(hc/\lambda kT)}}{k\lambda T^2(e^{(hc/\lambda kT)-1})} d\lambda \\
&= \frac{A_d}{4F^2} \Big(\frac{dM}{dT}\Big)_{T,[\lambda_1,\lambda_2]}, \\
&\text{where} \\
\Big(\frac{dM}{dT}\Big)_{T,[\lambda_1-\lambda_2]} &= \int_{\lambda_1}^{\lambda_2} M(\lambda,T) \frac{hce^{(hc/\lambda kT}}{k\lambda T^2(e^{(hc/\lambda kT)-1})} d\lambda. \qquad (2.64)
\end{aligned}$$

If we define $V_s(\Delta T_{target})$ to be the signal voltage caused by a temperature difference ΔT_{target}, the NETD is

$$\begin{aligned}
NETD &= \frac{\Delta T_{target}}{V_s(\Delta T_{target})/V_n} \\
&= \frac{\Delta T_{target} V_n}{\Re \Delta T_{target} \frac{d\Phi_{\lambda_1-\lambda_2}}{dT}} \\
&= \frac{4F^2 \Delta T_{target} V_n}{A_d \Re \Delta T_{target} \big(\frac{dM}{dT}\big)_{T,[\lambda_1-\lambda_2]}} \\
NETD &= \frac{4F^2 V_n}{A_d \Re \big(\frac{dM}{dT}\big)_{T,[\lambda_1-\lambda_2]}}. \qquad (2.65)
\end{aligned}$$

From Equation 2.61, we can write the NETD as a function of the NEP:

$$NETD = NEP \frac{4F^2}{A_d \big(\frac{dM}{dT}\big)_{T,[\lambda_1-\lambda_2]}}, \qquad (2.66)$$

or using Equation 2.62, as a function of the detectivity D^*:

$$NETD = \frac{\sqrt{B} * 4F^2}{D^* \sqrt{A_d} \big(\frac{dM}{dT}\big)_{T,[\lambda_1-\lambda_2]}}. \qquad (2.67)$$

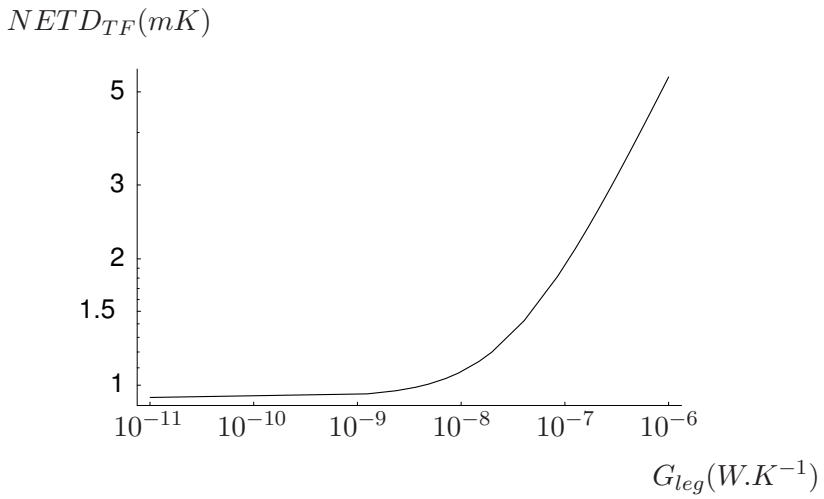

Figure 2.10: Ideal NETD as a Function of G_{leg}, adapted from [12]

2.3.9 Theoretical Limitations

Even if one could measure a temperature in a way that was free of Johnson noise and $1/f$ noise, the temperature-fluctuation would still be present:

$$\begin{aligned} NEP_{TF} &= \sqrt{S_0 B} \\ &= \sqrt{\frac{4kT^2 G_{th} B}{\eta^2}}, \end{aligned} \tag{2.68}$$

where S_0 is defined in Equation 2.58 and B is the bandwidth considered. From Equation 2.66, the expression of the temperature fluctuation-limited NETD is

$$\begin{aligned} NETD_{TF} &= \frac{4F^2 NEP_{TF}}{A_d \left(\frac{DM}{dT}\right)_{T,[\lambda_1-\lambda_2]}} \\ &= \frac{8F^2 T\sqrt{kG_{th}B}}{\eta A_d \left(\frac{dM}{dT}\right)_{T,[\lambda_1-\lambda_2]}}. \end{aligned} \tag{2.69}$$

Equation 2.69 shows the temperature fluctuation-limited NETD for a bolometer at temperature T irradiated by a blackbody source at the same temperature.

To reduce this NETD, the most obvious way is to reduce the thermal conductance G_{leg} in order to reduce the total thermal conductance G_{th}. However, once the total thermal conductance reaches G_{rad}, further reduction of G_{leg} does not improve the NETD and the

bolometer reaches its background temperature fluctuation noise limit[12]. The NETD is then given by

$$NETD_{BG} = \frac{8F^2T\sqrt{k8\eta\sigma_b T^3 A_d B}}{\eta A_d\left(\frac{dM}{dT}\right)_{T,[\lambda_1-\lambda_2]}} \tag{2.70}$$

$$= \frac{16F^2\sqrt{2k\sigma_b T^5 B}}{\sqrt{\eta A_d}\left(\frac{dM}{dT}\right)_{T,[\lambda_1-\lambda_2]}}. \tag{2.71}$$

As discussed in Section 2.4.1, for thermal imaging applications the area A_d cannot be changed dramatically. For an array used at video frame rate (30Hz), the integration time τ_{pulse} has to be $33ms$ or less. Figure 2.10 shows the minimum achievable NETD as a function of the suspension thermal conductance G_{leg} for $\tau_{pulse} = 33ms$, $\eta = 1$, $F = 1$, $A_d = 50\mu m * 50\mu m$, $T = 300K$, $\lambda_1 = 8\mu m$, and $\lambda_2 = 14\mu m$.

2.4 State of the Art

2.4.1 Orders of Magnitude

2.4.1.1 Pixel Size

When designing a LWIR imager, it is desirable to minimize the pixel size (as long as one is able to obtain the desired thermal conductance). There are two reasons for that: the cost of the optics and spatial resolution. The optical materials used for LWIR optics such as Germanium (Ge), Zinc Selenide (ZnSe), and Zinc Sulfide (ZnS) are expensive (in part because they require anti-reflection coating). It is therefore desirable to reduce the diameter of the lens used. For a constant F number, this requires a smaller array and therefore a smaller pixel size. A smaller pixel array is desirable to achieve high spatial resolution while keeping a reasonable size for the array. The theoretical minimum pixel size is dictated by the diffraction limit (assuming a perfect lens). The diameter of the first Airy disc is given by

$$d = \frac{f}{D}2.44\lambda. \tag{2.72}$$

thus for LWIR infrared and for an F/1 optics (typical for uncooled bolometer imaging arrays), this leads to a minimum pixel size of about $30\mu m$. However, for such a pixel size it would be difficult to achieve high fill-factor and low thermal conductance with available mi-

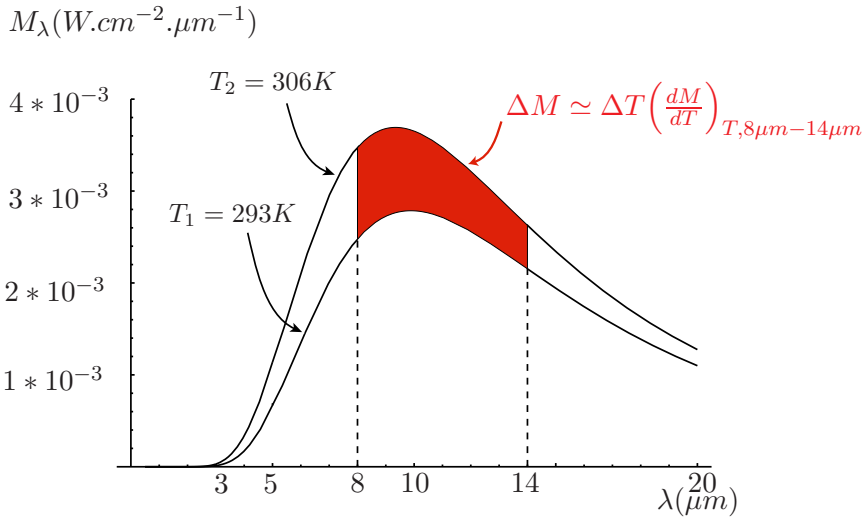

Figure 2.11: Spectral Exitance of Blackbody Sources at Different Temperatures

crofabrication techniques and materials. The typical pixel size in state-of-the-art bolometer arrays is between $35\mu m$ and $50\mu m$.

2.4.1.2 Bolometer Temperature Resolution

Suppose we want to use a bolometer array to "see" a person with a skin temperature of 33^oC ($\simeq 360^oK$) in a room at 20^oC ($\simeq 293^oK$). Figure 2.11 shows the difference of spectral exitance in the wavelength range considered. The difference in exitance (shaded on Figure 2.11) between the background and the subject over the $8\mu m - 14\mu m$ range can be estimated to be:

$$\Delta M \simeq \Delta T_s \left(\frac{dM}{dT}\right)_{300K,8\mu m-14\mu m}. \tag{2.73}$$

From Equation 2.64 we calculate

$$\left(\frac{dM}{dT}\right)_{300K,8\mu m-14\mu m} = 2.6 * 10^{-4} W.cm^{-2}. \tag{2.74}$$

For a change ΔT_s in source temperature, the difference in radiant flux incoming on the bolometer is given by

$$\Delta\Phi \quad = \quad \frac{A_d \Delta T_s}{4F^2}\left(\frac{dM}{dT}\right)_{300K,8\mu m-14\mu m}, \tag{2.75}$$

and the corresponding change in bolometer temperature is given by

$$\Delta T_d = \frac{A_d \Delta T_s}{4 G_{th} F^2} \left(\frac{dM}{dT}\right)_{300K, 8\mu m - 14\mu m}. \tag{2.76}$$

Let us consider a bolometer and its optical system having parameters $F = 1$, $A_d = (50\mu m)^2$, and $G_{th} = 10^{-7} W.K^{-1}$ and calculate the changes in incoming radiant flux (Equation 2.75) and bolometer temperature (Equation 2.76) for different changes in source temperature.

- If $\Delta T_s = 13^o C$ (difference between human subject skin and background at room temperature), we have $\Delta\Phi = 21.1nW$ and $\Delta T_d = 211mK$.
- If $\Delta T_s = 50mK$,we have $\Delta\Phi = 81.2pW$ and $\Delta T_d = 812\mu K$. Hence, by definition, to have an NETD of $50mK$ the resolution of the bolometer temperature measurement needs to be better than $812\mu K$.

2.4.2 Vanadium Oxide (VOx) Bolometers

Vanadium oxide bolometers are one of the most successful kinds of bolometers. They combine high TCR ($\simeq 2\%.K^{-1}$) and low $1/f$ noise. Table 2.2 shows a summary of parameters for a 240*336 array. The achieved NETD is $39mK$.

2.4.3 Titanium Bolometers

Titanium has been demonstrated as a thermistor material in bolometers [15, 16]. One of the main advantages of using titanium is its full compatibility with IC fabrication processes, allowing monolithic integration. Although titanium has a relatively low TCR (compared with other bolometer materials), its low $1/f$ leads to an acceptable performance (see discussion in Section 2.5.4).

2.4.4 Silicon Bolometers

Amorphous silicon is used in commercial bolometer arrays in the US by Raytheon Company and in France by ULIS. Amorphous silicon has the advantage of being easily integrated into IC fabrication processes while having a good TCR. However, the $1/f$ is high as well. The NETD claimed by Raytheon (now Thermal-Eye) in its handheld $160*120$ pixel cameras is $100mK$ [17]. The ULIS UL01011 is said to have an average NETD of $85mK$ [18].

Parameter	**Value**
Pitch	$50\mu m$
Fill Factor	70%
Support material	$0.8\mu m$ Silicon Nitride
Beam Lateral Dimensions	$2\mu m * 50\mu m$
Thermal Capacitance	$3 * 10^{-9} J.K^{-1}$
Thermal Conductance	$2 * 10^{-7} W.K^{-1}$
Thermal Time Constant	$15ms$
Absorptivity	80%
Sensing Material	Vanadium Oxide
TCR	$-2.3\%.K^{-1}$
Pixel Resistance	$20k\Omega$
Responsivity	$3.2\,10^5 V.W^{-1}@V_b = 5V$
Detector Noise	$20\mu V$
Frame Rate	$30Hz$
Integration Time	$5\mu s$
Bias Current	$250\mu A$
NETD (F/1)	$39mK$

Table 2.2: Parameters of a 240*336 Array of VOx Bolometers, from [14]

Parameter	**Value**
Pitch	$50\mu m$
Fill Factor	59%
Support material	$0.8\mu m$ CVD Silicon Dioxide
Absorptivity	unreported
Thermal Conductance	$2.2 * 10^{-7} W.K^{-1}$
Thermal Time Constant	$15ms$
Absorptivity	80%
Sensing Material	Titanium
TCR	$+0.25\%.K^{-1}$
Pixel Resistance	$3.4k\Omega$
Responsivity	$1.06\,10^5 V.W^{-1} * \eta @ V_b = 8.5V$
Frame Rate	$30Hz$
Integration Time	$5.3\mu s$
Bias Current	$2.50mA$
NETD (F/1)	$90mK$

Table 2.3: Parameters of a 128*128 Array of Titanium Bolometers, from [15]

In [19], Eminoglu et. al. reported single-crystal silicon bolometers fabricated using a CMOS post-processing. Again, the integration with IC fabrication is a very attractive feature. However, the obtained TCR is low ($.34\%.K^{-1}$). Because the $1/f$ is very small in single-crystal silicon, the noise is dominated by Johnson noise. The obtained NETD of $80\mu m * 80\mu m$ pixels with $F/1$ optics and using a $125\mu s$ integration time was $470mK$.

2.4.5 Other Types of Bolometers

Among other materials used to fabricate bolometers are Yttrium Barium Copper Oxide (YBaCuO) [20, 21]. High TCRs can be achieved while the $1/f$ noise remains relatively low. In [22], Hayashi et. al. use Perovskite Manganese Oxide (BiLaSrMnO) as the sensitive material. The reported NETD is lower than $100mK$ (although the noise itself is not reported). olycrystalline silicon germanium alloys (Poly SiGe) were reported in [23] with an achieved TCR of $2\%.K-1$ and a $1/f$ noise factor of $K = 6.62 * 10^{-12}$. A bolometer based on amorphous germanium-silicon-oxygen (GeSiO) was presented in [24]. The reported TCR is high but is obtained for high values of resistivities ($10^5\Omega.cm$). The achieved responsivity was $380V.W^{-1}$, but the value of $1/f$ noise was not reported. silicon carbide was also proposed as the temperature sensitive material in [25]. The TCR was reported to be as high as $6.5\%.K^{-1}$. However, even though the $1/f$ noise spectral was measured, the bias and the frequency at which the measurement was made were not reported.

2.5 Reaching the Theoretical Limit

If the total bolometer noise is dominated by the temperature fluctuation noise, the theoretical limit is reached and the NEP and NETD can only by reduced by decreasing G_{th}.[4] In this section, we discuss $1/f$ noise and Johnson noise only. The $1/f$ noise-limited NETD and the Johnson noise-limited NETD are given respectively by

$$NETD_f = \frac{4F^2G_{th}}{A_d\eta\alpha\left(\frac{dM}{dT}\right)_{T,[\lambda_1-\lambda_2]}}\sqrt{K\left(\frac{3}{2}-\gamma-\ln(2\pi f_1\tau_{pulse})\right)} \tag{2.77}$$

$$NETD_j = \frac{4F^2G_{th}}{A_d\eta\alpha V_b\left(\frac{dM}{dT}\right)_{T,[\lambda_1-\lambda_2]}}\sqrt{\frac{2kTR}{\tau_{pulse}}} \tag{2.78}$$

[4] For a given area.

2.5.1 Lower G_{th} and C_{th}

The pixel-to-substrate thermal conductance of current bolometers is about three times higher than their radiative thermal conductance. Progress could still be made by decreasing the pixel-to-substrate conductance. However, the thermal time constant of most state-of-the-art bolometers is on the order of a few tens of milliseconds, the maximum acceptable for thermal imaging. As mentioned in Section 2.3.3.2, any lowering of thermal conductance would have to be accompanied by a lowering of thermal capacitance. Most existing devices use metallic or semiconducting thermistors and metallic electrodes; these materials can not be made freestanding without a supporting material which adds dead thermal conductance and dead thermal capacitance to the device. It would be desirable to find a materials which could be used as electrode and/or thermistor without the need of a supporting material.

2.5.2 Higher Absorptivity

Most current bolometers rely on quarter-wavelength cavities to reach absorptivities η close to 80% in the $8\mu m - 14\mu m$ band. Therefore, only little could be gained from increasing the absorptivity.

2.5.3 Wider Bandwidth

One could think of using materials with absorptivities high enough to not require cavities. The $3\mu m - 5\mu m$ band could then be used in conjunction with the $8\mu m - 14\mu m$ band. However, the NETD would only by marginally improved because the of the low exitance of blackbody sources in this band, as shown in Equation 2.79 and Equation 2.80.

$$\left(\frac{dM}{dT}\right)_{300K,[3\mu m-5\mu m]} = 2.1 * 10^{-5} W.cm^{-2}.K^{-1} \quad (2.79)$$

$$\left(\frac{dM}{dT}\right)_{300K,[8\mu m-14\mu m]} = 2.6 * 10^{-4} W.cm^{-2}.K^{-1} \quad (2.80)$$

2.5.4 Higher TCR and Lower $1/f$ Noise Material

Having a material with higher TCR α would improve both responsivity and NETD. There are indeed materials with TCRs higher than those found in current bolometers. Unfortunately, it often comes at the price of higher resistivity (therefore more Johnson noise) and higher $1/f$ noise. Usually, increasing the TCR by half of an order of magnitude

leads to an increase in resistivity and $1/f$ noise by several orders of magnitude. It is important to note that in terms of NETD, the TCR is not the only parameter to consider. The total noise of a bolometer biased at V_b during an integration time τ_{pulse} is given by (2.3.5):

$$\sqrt{KV_b^2\Big(\frac{3}{2}-\gamma-\ln(2\pi f_1\tau_{pulse})\Big)+\frac{2kTR}{\tau_{pulse}}}. \tag{2.81}$$

If we define a constant

$$C=\frac{4F^2}{A_d\big(\frac{dM}{dT}\big)_{T,[\lambda_1-\lambda_2]}},$$

then combining Equation 2.81 and Equation 2.65 we get:

$$NETD=\frac{CG_{th}\sqrt{KV_b^2\Big(\frac{3}{2}-\gamma-\ln(2\pi f_1\tau_{pulse})\Big)+\frac{2kTR}{\tau_{pulse}}}}{\eta\alpha V_b}. \tag{2.82}$$

As can be seen on Equation 2.82, if the total noise is dominated by the Johnson noise (second term in the square root), an increase in V_b or τ_{pulse} results in a better NETD. Then, if all other parameters are constant, the NETD reduces to

$$NETD_f=\frac{CG_{th}\sqrt{K\Big(\frac{3}{2}-\gamma-\ln(2\pi f_1\tau_{pulse})^2\Big)}}{\eta\alpha}. \tag{2.83}$$

Equation 2.83 suggests the introduction of a figure of merit β for materials to be used as the temperature sensor in bolometers (such a figure of merit was originaly proposed in [26]):

$$\beta=\frac{|\alpha|}{\sqrt{K}}. \tag{2.84}$$

For VOx having a TCR of $-2.3\%.K^{-1}$, the $1/f$ noise constant is reported to be $K=10^{-13}$ [14]. This leads to a value $\beta=7.3*10^4K^{-1}.V.Hz^{-1/2}$. For films of titanium having a TCR of $0.25\%.K^{-1}$, the reported $1/f$ noise constant is $K=3*10^-15$, leading to a $\beta=4.6*10^4K^{-1}.V.Hz^{-1/2}$. Therefore, even though the TCR of titanium is one order of magnitude lower than that of VOx, the $1/f$ noise-limited NETD that can be obtained with Ti is only 2.4 times higher than what can be obtained with VOx. Vanadium oxide and titanium are currently used in bolometer arrays precisely because they have a good ratio of TCR over noise. However, one can hope for materials that would surpass the existing ones

in terms of β which would reduce the $1/f$-limited NETD.

2.5.5 Integration Time and Current Bias

Both the $1/f$ noise and the Johnson noise are decreasing functions of the integration time.[5] Figure 2.12 shows the Johnson and $1/f$ noise contributions for different values of bolometer resistance and $1/f$ noise factor $KV_b{}^2$. It appears that if the $1/f$ noise is dominant, increasing the integration time has very little effect on the total noise. For example if a bolometer has a resistance $R_0 = 20k\Omega$ and a $1/f$ noise factor $KV_b{}^2 = 10^{-13}\,V^2$, then

- For an integration time $\tau_{pulse} = 1\mu s$, the noise is dominated by Johnson noise and is about $10\mu V$.
- For an integration time $\tau_{pulse} = 100\mu s$, the contribution of Johnson noise and $1/f$ noise are comparable and total noise approaches $1\mu V$.
- For an integration time $\tau_{pulse} = 10ms$, the noise is dominated by $1/f$ noise and is virtually the same as it was for $\tau_{pulse} = 100\mu s$.

If the noise is Johnson-dominated, it can be reduced by increasing the integration time or by increasing the biasing current. Once the contributions of Johnson noise and $1/f$ noise are comparable, it is useless to further increase the integration time or to the further increase the biasing current.

[5] For realistic numbers design parameter $f_1 << \frac{1}{\tau_{pulse}}$ and Equation 2.83 is defined.

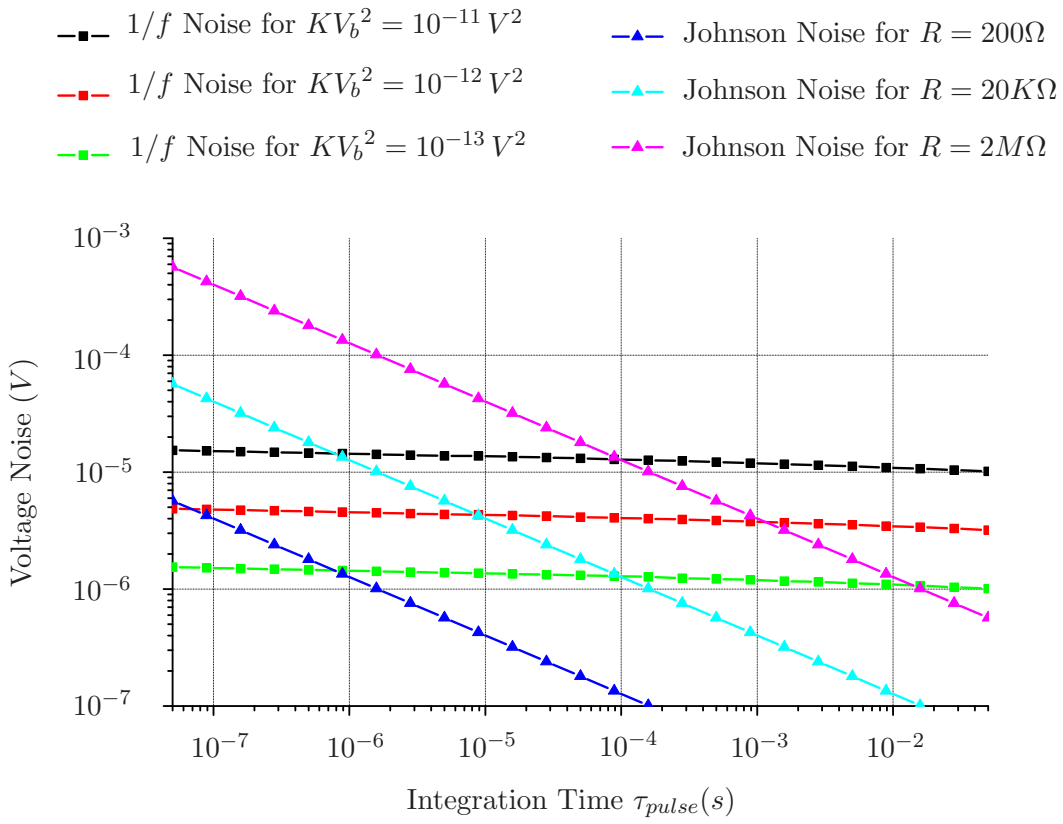

Figure 2.12: Noise Behavior for Different Integration Times

Bibliography

[1] M. Bass, ed., *Handbook of Optics*, vol. II: Devices, Measurements, & Properties. McGraw-Hill, 2d ed., 1995. 22

[2] J. Johnson, "Thermal agitation of electricity in conductors," *Phys. Rev.*, vol. 32, 1928. 32

[3] H. Nyquist, "Thermal agitation of electric charge in conductors," *Phys. Rev.*, vol. 32, 1928. 32

[4] J. Johnson, "The schottky effect in low frequency circuits," *Phys. Rev.*, vol. 26, p. 7185, 1925. 33

[5] E. Milotti, "1/f noise: a pedagogical review," tech. rep., 2001. http://arxiv.org/ftp/physics/papers/0204/0204033.pdf. 33

[6] P. Gray, P. Hurst, S. Lewis, and R. Meyer, *Analysis and Design of Analog Integrated Circuits*. John Wiley and Sons, Inc, 4 ed., 2001. 33

[7] F. N. Hooge, "1/f noise is no surface effect," *Phys. Lett.*, vol. 29A, 1969. 34

[8] F. Hooge, "1/f noise sources," *IEEE Transactions on Electron Devices*, vol. 41, no. 11, pp. 1926–1935, 1994. 34

[9] V. Y. Zerov, Y. V. Kulikov, V. Malyarov, I. Kherbtov, I. Shaganov, , and E. Shadrin, "Vanadium oxide films with improved characteristics for ir microbolometeric matrices," *Technical Physical Letters*, vol. 27, pp. 378–380, 2001. 34

[10] H. K. Lee, S. Y. Myong, K. S. Lim, and E. Yoon, "Electrical properties of photo-cvd boron-doped hydrogenated nanocrystalline silicon-carbide (p-nc-sic:h) films for uncooled ir bolometer applications," *Journal of Non-Crystalline Solids*, vol. 316, pp. 297–301, 2003. 34

[11] E. W. Weisstein, "Cosine integral.," *MathWorld–A Wolfram Web Resource*, 2005. http://mathworld.wolfram.com/CosineIntegral.html. 35

[12] P. W. Kruse, *Uncooled Thermal Imaging. Arrays, Systems, and Applications*. SPIE-The International Society for Optical Engineering, 2001. xi, 36, 37, 40, 41

[13] P. G. Datskos and N. V. Lavrik, "Detectors figures of merit," tech. rep., Oak Ridge National Laboratory, 2003. 38

[14] R. A. Wood, "Uncooled infrared imaging systems," in *Semiconductor and Semimetals* (D. D. Skatrud and P. W. Kruse, eds.), vol. 47, ch. 3, Academic Press, 1997. xiv, 44, 48

[15] A. Tanaka, S. Matsumoto, N. Tsukamoto, S. Itoh, K. Chiba, T. Endoh, A. Nakazato, K. Okuyama, Y. Kumazawa, M. Hijikawa, H. Gotoh, T. Tanaka, and N. Teranishi, "Infrared focal plane array incorporating silicon ic process compatible bolometer," *IEEE Transactions on Electron Devices*, vol. 46, no. 11, 1996. xiv, 43, 45

[16] H. Lee, J. Yoon, E. Yoon, S. Ju, Y. Yong, W. Lee, and S. Kim, "A high fill-factor infrared bolometer using micromachined multilevel electrothermal structures," *IEEE Transactions on Electron Devices*, vol. 46, pp. 1489–1491, July 1999. 43

[17] "Thermal-eye x100xp brochure," tech. rep., Thermal-Eye, 2005. 43

[18] "Ul 01011 brochure," tech. rep., ULSI-IR, 2004. 43

[19] S. Eminoglu, D. Tezcan, M. Tanrikulu, and T. Akin, "Low-cost uncooled infrared detectors in cmos process," *Sensors and Actuators A*, vol. 109, 2003. 46

[20] A. Jahanzeb, C. Travers, Z. Celik-Butler, D. Butler, and S. Tan, "A semiconductor ybacuo microbolometer for room temperature ir imaging," *IEEE Transactions On Electron Devices*, vol. 44, pp. 1795–1801, October 1997. 46

[21] M. Almasri, D. Butler, and Z. Celik-Butler, "Self-supporting uncooled infrared microbolometers with low-thermal mass," *Journal of Microelectromechanical Systems*, vol. 10, pp. 469–476, September 2001. 46

[22] K. Hayashi, E. Ohta, H. Wada, H. Higuma, and S. Miyashita, "Fabrication of bilasrmno uncooled microbolometer," *Japanese Journal of Applied Physics*, vol. 1, pp. 5281–5284, March 2001. 46

[23] S. Sedky, P. Fiorini, M. Caymaxa, C. Baert, L. Hermans, and R. Mertens, "Characterization of bolometers based on polycrystalline silicon germanium alloys," *IEEE Electron Device Letters*, vol. 19, October 1998. 46

[24] E. Iborra, M. Clement, L. V. Herrero, and J. Sangrador, "Ir uncooled bolometers based on amorphous $g_{e_x}s_{i_{1-x}}o_y$ on silicon micromachined structures," *Journal of Microelectromechanical Systems*, vol. 11, August 2002. 46

[25] T. Ichihara, Y. Watabe, Y. Honda, and K. Aizawa, "A high performance amorphous sic:h thermistor bolometerbased on micro-machined structure," in *International Conference on Solid-state Sensors and Actuators Transducers 97*, (Chicago, IL), june 1997. 46

[26] P. C. Shan, Z. Celik-Butler, D. P. Butler, A. Jahanzeb, C. M. Travers, W. Kula, and R. Sobolewski, "Investigation of semiconducting ybacuo thin films: A new room temperature bolometer," *Journal of Applied Physics*, vol. 80, no. 12, pp. 7118–7123, 1996. 48

Chapter 3

Pyrolyzed Parylene as a MEMS Material

3.1 Parylene

3.1.1 Chemical Structure and Deposition Process

Parylene is a generic name for poly-para-xylylene (parylene N) and its modified versions, parylene C and D [1]. Figure 3.1 shows the chemical structure of different types of commercially available parylenes. Parylene is a polymer deposited by vapor phase. Figure 3.2 shows the deposition process for parylene C. A powder of di-monochloro-para-xylylene dimer (Figure 3.3) is placed into a vaporizer taken to temperatures up to 170°C. The dimer sublimates and enters a pyrolysis section at 690°C where it is broken into para-monochloro-xylylene monomer. The monomer vapor then enters the deposition chamber, which is normally at room temperature. The monomer vapor then polymerizes into poly-para-monochloro-xylylene on surfaces inside the chamber. In a typical parylene deposition system, the pressure inside the chamber is regulated by controlling the vaporizer temperature through a feedback loop. The film quality is a function of the pressure. If the pressure is too high, the quality of the parylene film will be poor[2]. Typical vapor pressures are

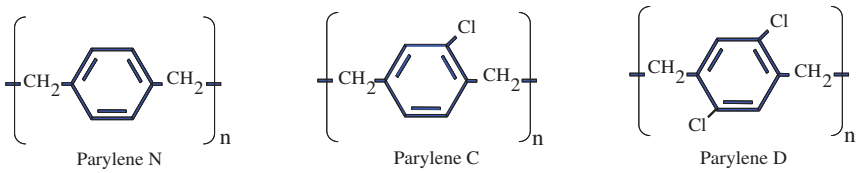

Figure 3.1: Chemical structure of different types of parylenes

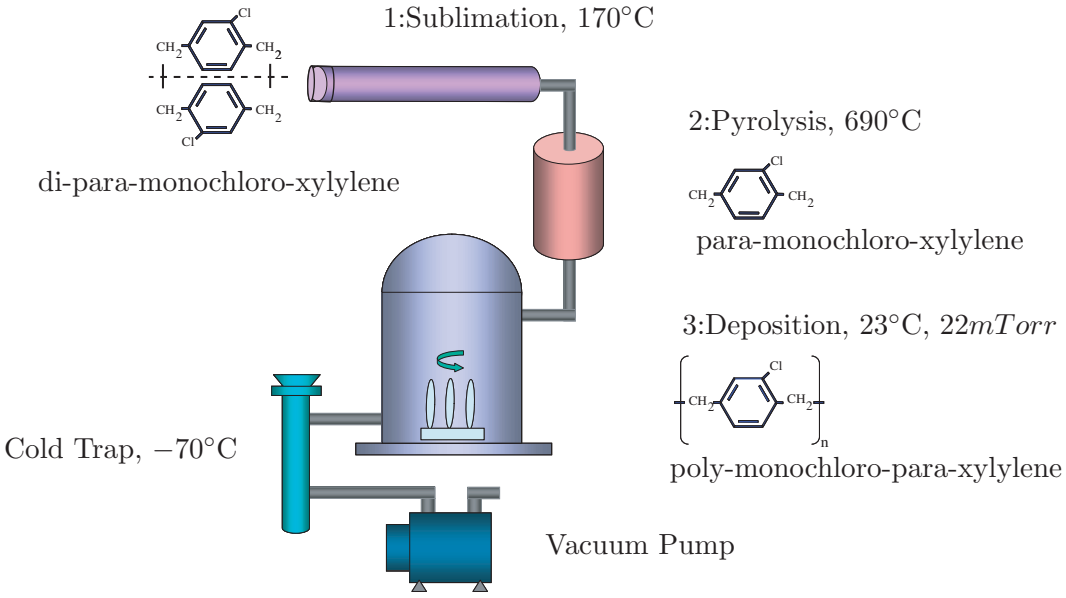

Figure 3.2: Parylene Deposition Process

Figure 3.3: Di-para-xylylene Dimer

between $10mTorr$ and $100mTorr$, leading to deposition rates of about $0.7\mu m$ per hour for parylene N and $5\mu m$ for parylene C and D. Because parylene molecules bounce many times before depositing and polymerizing, parylene films are highly conformal. Pinhole-free parylene films as thin a a few hundred angstroms can be deposited. The deposition rate of parylene has a strong dependence on substrate temperature (increasing with decreasing temperature). For this reason the cold trap located before the pump is highly effective in capturing the excess vapor before it reaches the pump. On the other hand, the deposition rate can be greatly reduced by increasing the substrate temperature and is negligible if the substrate temperature is above 140°C. Using this fact, localized substrate heating can be used to selectively deposit parylene on certain substrate areas [3, 4].

Figure 3.4: Parylene C Film

3.1.2 Properties

Parylene films are transparent to visible light and look plastic-like. Figure 3.4 shows a film of parylene after it was taken off its substrate. Parylene strongly absorbs UV having wavelength below $280nm$ and can be damaged by strong UV radiation. For this reason parylene should not be exposed to sunlight for extended periods of time. Parylene is inert to most chemicals, organic solvents, acid, and alkaline solutions but can be dissolved by chloro-napthalene (at 175°C for parylene C and 265°C for parylene N) [1]. Even though parylene is not attacked by acids like HF or solvents like acetone, it has been shown that those chemicals can either swell parylene or permeate through it [5].

3.1.2.1 Mechanical Properties

Table 3.1 shows selected mechanical properties of parylene. The density of parylene is much lower than that of silicon, and its Young's modulus is 20 to 70 times lower. For this reason, when used in MEMS one can think of parylene as being to silicon what plastic is to metal.

	Parylene N	Parylene C	Parylene D
Density ($g.cm^{-3}$)	$1.10 - 1.12$	1.289	1.418
Young's Modulus (GPa)	2.4	2.7	2.6
Tensile Strength (MPa)	$43 - 76$	69	76
Yield Strength (MPa)	42	55	62

Table 3.1: Selected Mechanical Properties of Parylene [1]

3.1.2.2 Electrical Properties

Table 3.2 shows electrical properties of parylene. Parylene is a good electrical insulator; in fact, it has been studied as a possible low-k dielectric in integrated circuits [6]. The dielectric dissipation factor is one of the parameters that varies the most among the different types of parylene. Electrostatic actuators made of free-standing parylene have been demonstrated, e.g., in [7]. However, it has also been shown that under high electric field, parylene surfaces undergo charging [8].

	Parylene N	Parylene C	Parylene D
Volume Resistivity ($\Omega.cm$)	$1.4 * 10^{17}$	$8.8 * 10^{16}$	$1.2 * 10^{17}$
Dielectric Strength ($V.cm^{-1}$)	$2.76 * 10^{6}$	$2.21 * 10^{6}$	$2.17 * 10^{6}$
Dielectric Constant @$60Hz$	2.65	3.15	2.84
Dissipation factor @$60Hz$	$2 * 10^{-4}$	$4 * 10^{-2}$	$4 * 10^{-3}$

Table 3.2: Selected Electrical Properties of Parylene [1]

3.1.2.3 Thermal Properties

Table 3.3 shows selected thermal properties of parylene. As can be seen, the thermal conductivity of parylene is extremely low, about four orders of magnitude lower than metals and silicon and more than one order of magnitude lower than silicon dioxide and silicon nitride. In fact, the thermal conductivity of parylene C (which is lowest among parylenes) is only three times that of air. The thermal capacity per unit volume is also a few times lower than metals, silicon, oxide, or nitride. The melting point is different among the different types of parylene. Parylene N has the highest melting point at 420°C, and parylene C has the lowest melting point at 290°C. The coefficient of thermal expansion of parylene is one order of magnitude higher than that of silicon and of the same order of magnitude as metals.

3.1.3 Parylene as a MEMS Material

Over the past decade, parylene has become more and more popular among researchers in the Micro Electro-Mechnanical Systems (MEMS) field. Parylene can easily be patterned using conventional lithography and O_2 etching. Furthermore its low-temperature deposi-

Parameter	Parylene N	Parylene C	Parylene D
Melting Point (° C)	420	290	380
Linear Coefficient of Expansion (K^{-1})	$6.9 * 10^{-5}$	$3.5 * 10^{-5}$	$3 - 8 * 10^{-5}$
Thermal Conductivity ($W.m^{-1}.K^{-1}$)	0.13	$8.4 * 10^{-2}$	–
Specific Heat ($J.K^{-1}.g^{-1}$)	0.84	0.71	–
Volumic Heat Capacity ($J.K^{-1}.cm^{-3}$)	0.92	0.92	–

Table 3.3: Selected Thermal Properties of Parylene [1]

tion, conformality, and biocompatibility make it an attractive candidate for devices such as microfluidic and implantable devices [9, 10].

3.2 Parylene Pyrolysis

3.2.1 Pyrolysis

Pyrolysis, from the Greek *pyro* (fire) and *lusis* (loosen) is defined as the decomposition of a material or compound due to heat [11]. For organic materials, pyrolysis has to be performed in the absence of oxygen to avoid oxidation. For this reason it is sometimes called "incomplete combustion".

Pyrolysis has been known and used for centuries, even though it is impossible to say how many. In fact, it is interesting to know that it was by pyrolysis of organic materials that Thomas Edison produced his first incandescent filaments. He stated in his patent on "Electric Lamp" awarded in 1880 [12]:

> "I have discovered that even a cotton thread carbonized and placed in a glass bulb exhausted to one millionth of an atmosphere offers from one hundred to five hundred ohms resistance to the passage of current."

Reports of phenol formaldehyde resin (bakelite) pyrolysis can be traced back to the 1960s [13], and other polymers such as polyimide have also been studied [14]. Mechanical properties of carbon films obtained by pyrolysis of furfuryl alcohol-modified phenolic resin were reported in [15].

In [16, 17] the potential of pyrolyzed photoresist for MEMS and electrochemical applications was investigated. Table 3.4 shows the sheet resistance of $6\mu m$ films of AZ4330

Pyrolysis Temperature	**Sheet Resistance** ($\Omega/\square$)
600	146.4
700	845.8
800	244.8
900	94.3
1000	57.1
1100	52.1

Table 3.4: Sheet Resistance of $6\mu m$ films of Photoresist after Pyrolysis, after [17]

photoresist pyrolyzed at different temperatures from [17]. The minimum obtained resistivity was $5.1 * 10^{-3}\Omega.cm$, which is comparable to commercial glassy carbon. The measured weight loss was up to 69% and the thickness shrinkage up to 84%. It was also reported that films obtained by pyrolysis at 600°C had an unstable resistivity.

In [18], Wang et al. proposed using free-standing pyrolyzed-photoresist as tunable resistors. They found that by using different biasing currents the resistance of the free-standing resistors could be increased or decreased. Their conclusion was that the increase of resistance was due to thermal oxidation (the experiments were made in air) and that the decrease in resistance was due to further carbonization. Another prior work of interest was conducted by Hui et al. [19]. In this work parylene was pyrolyzed above $700°C$ in order to produce a high-temperature sacrificial layer that could be easily removed by oxidation at high temperature. However, the transition of properties from parylene to carbon was not reported, and neither were mechanical and electrical properties. Two attractive features of parylene are first the fact that it is free of any solvent or of any feature-enhancer (as opposed to photoresist or polyimide) and second that its chemical vapor deposition process of parylene leads to very pure films. Therefore, it is reasonable to think that pyrolysis of parylene films leads to carbon films of better quality and having a better reproducibility.

In the following sections, we report for the first time on the properties of parylene C films after pyrolysis. We present data on the structure and mechanical and electrical properties of parylene films after pyrolysis at temperatures ranging from 400°C to 1500°C. We also discuss some of the issues associated with the integration of pyrolyzed-parylene films into regular MEMS fabrication processes in order to use those films in devices.

3.2.2 Process

$4\mu m$-thick parylene C films were deposited on silicon wafers and pyrolyzed at different temperatures in N_2 atmosphere with a $10°C/min$ ramp rate. In addition to silicon, parylene films were deposited on silicon/titanium/platinum (Si/Ti/Pt) and silicon/chrome/gold to estimate catalytic effects of platinum and gold.

3.2.2.1 Appearance and Thickness Change

Under an optical microscope, pyrolyzed-parylene films look dark, smooth, and continuous. No changes in lateral directions of parylene C film could be observed in our experiments. The thicknesses of parylene films were measured before and after pyrolysis with an Alphastep surface profilometer. Figure 3.5 shows the thickness (%) as the ratio of thickness between the pyrolyzed films and their initial thickness. Only little changes in thickness can be observed for temperatures below 500°C. In fact, there is little change in the appearance of the films as well. Films pyrolyzed at 600°C on Si experienced a shrinkage of about 75%, while films pyrolyzed at 800°C and above experienced a shrinkage of about 80%. Shrinkage appears to continue to occur as the pyrolysis temperature is increased above 800°C, but only slightly. The thickness of films pyrolyzed on Si/Ti/Pt decreased by 85% for 800°C pyrolysis, while that of films pyrolyzed Si and Si/Cr/Au decreased by 80% for 800°C pyrolysis. This indicates a slight catalytic effect of platinum on the pyrolysis process and no catalytic effect of gold.

3.2.2.2 Weight Loss

The weight of several parylene C films were measured before and after pyrolysis. Figure 3.6 shows the weight (in %) of pyrolyzed films where 100% is their initial weight. As expected (and similar to thickness change), very little weight change occurs for pyrolysis temperatures below $500°C$. It was found that after exposure to air (20°C, 47% in humidity) the weight of pyrolyzed-parylene film decreases if baked at 100°C or if placed in vacuum. The weight then increases when once exposed to air. We believe this weight change is due to moisture absorption and desorption. Electrical resistivity experiments also suggest that pyrolyzed-parylene films can absorb airborne moisture (See Section 3.2.5.4). As can be seen on Figure 3.6, the weight loss of films pyrolyzed on silicon/titanium/platinum is about 5%

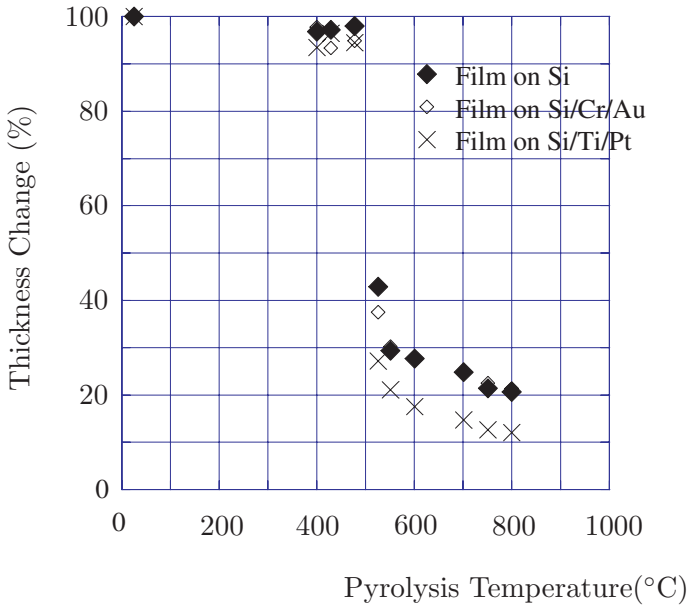

Figure 3.5: Thickness Change

higher than that of films pyrolyzed on bare silicon or silicon/chrome/gold. However, there is no observable shift in the temperature at which the weight loss starts to occur.

3.2.2.3 TEM

A film of parylene C pyrolyzed at 800°C was observed using a Transmission Electron Microscope (TEM) (Figure 3.7), and small amounts of graphite-like crystallite structures can be seen. The electron-diffraction diagram also confirms the existence of (002) plane of graphite. However, as a whole, this film is recognized as amorphous carbon.

3.2.2.4 TGA, DSC, and Raman Analysis

Thermogravimetric analysis (TGA) and differential scanning calorimetry (DSC) was performed in the solid state ionics and electroceramics lab at the California Institute of Technology [1] and reported in [20]. Thermogravimetric analysis (TGA)and differential scanning calorimetry (DSC) were performed simultaneously on a film of parylene C. Figure 3.9 reproduces the obtained data. As seen in Figure 3.9, the material undergoes an endothermic phase transition at 296°C [20]. This is consistent with the melting temperature

[1] data taken by graduate student Stacey Boland

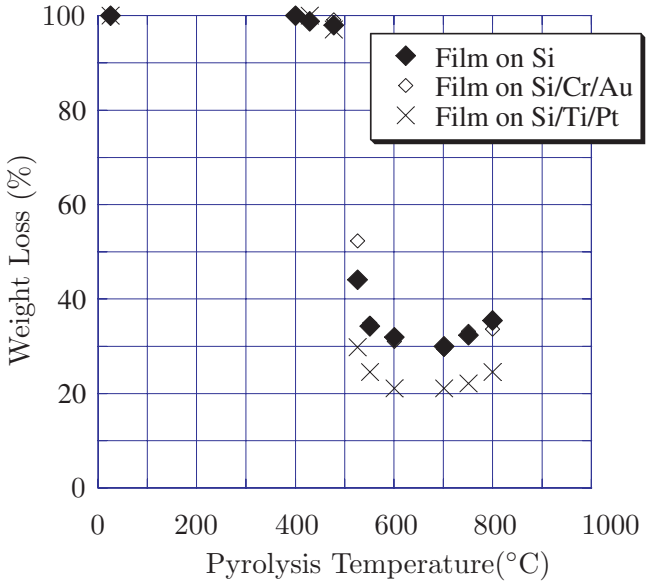

Figure 3.6: Weight Loss

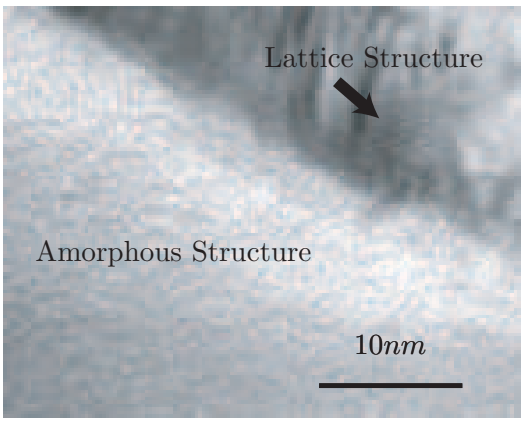

Figure 3.7: Pyrolyzed Parylene TEM Micrograph

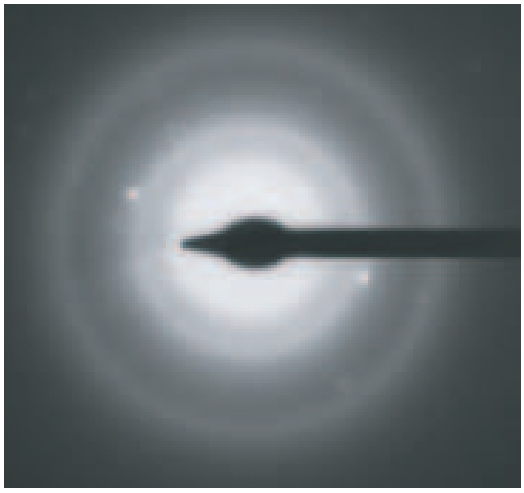

Figure 3.8: Pyrolyzed Parylene Diffraction Pattern

of 290°C provided by parylene dimer manufacturer (see Table 3.3). An exothermic event occurs simultaneously at 480°C, which we identify as the actual pyrolysis in its literal meaning. This is consistent with the observed thickness change and weight loss discussed in Sections 3.2.2.1 and 3.2.2.2, respectively. The weight loss during this event was 66%. At temperatures above 500°C, the weight continued to decrease slightly, and the the total loss at 1500°C was 70.1%, consistent with experiments conducted on silicon and silicon/chrome/gold.

Raman analysis was done on both a free-standing pyrolyzed parylene film pyrolyzed at 1550°C and a film of parylene deposited on Si and subsequently pyrolyzed at 900°C in N_2[20]. Figure 3.10 reproduces the results of this experiment. The data obtained for parylene pyrolyzed at 900°C on Si shows broad and poorly defined G and $D1$ peaks, whereas the free-standing film shows narrow, well-defined peaks, clearly indicative of glassy carbon. For purely crystalline graphite, only the G band would be observed while the presence of the $D1$ band indicates a finite particle size[20]. From these experiments, as well as TEM observation and diffraction pattern, we can conclude that pyrolysis of parylene above 500°C leads to films of amorphous carbon that become increasingly graphitic, or crystalline, as the pyrolysis temperature is increased further.

3.2.3 Processing of Pyrolyzed Parylene

Pyrolyzed-parylene is easy to integrate in a MEMS fabrication process. Figure 3.11 shows a film of pyrolyzed-parylene patterning with oxygen plasma and on which a layer of

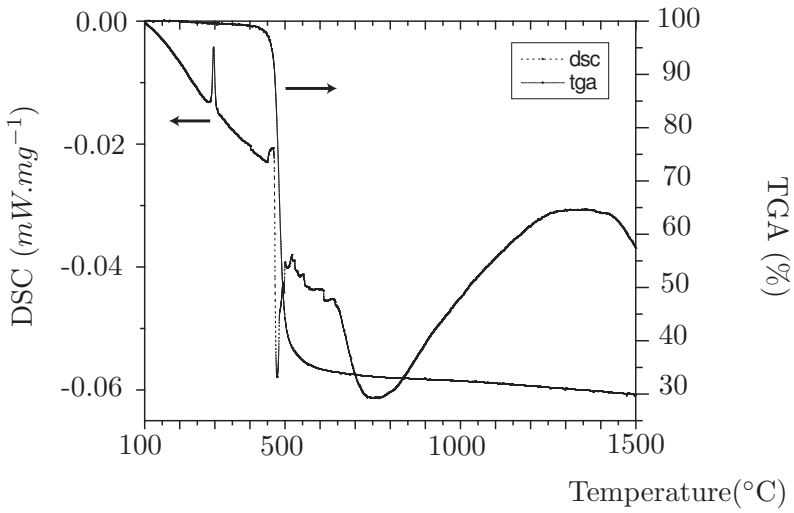

Figure 3.9: TGA and DSC, courtesy of [20]

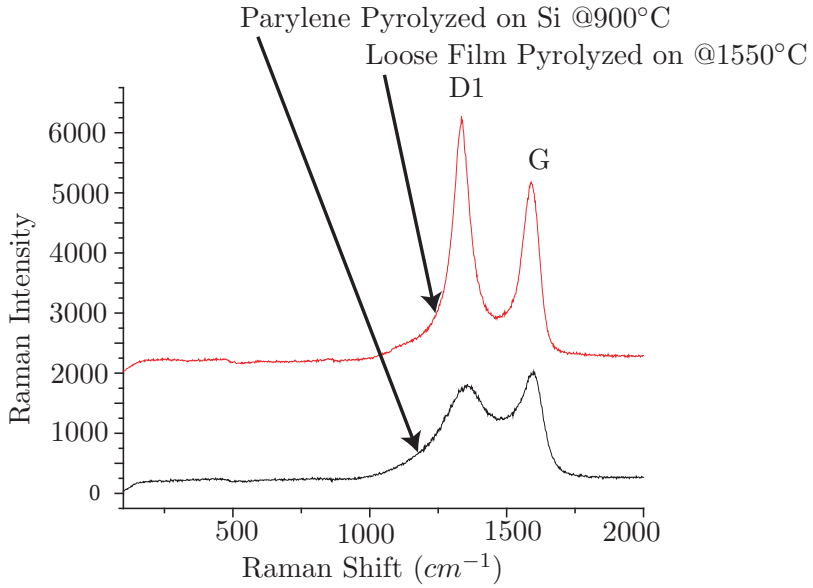

Figure 3.10: Raman Analysis, courtesy of [20]

Figure 3.11: Patterned and Selectively Metallized Pyrolyzed Parylene

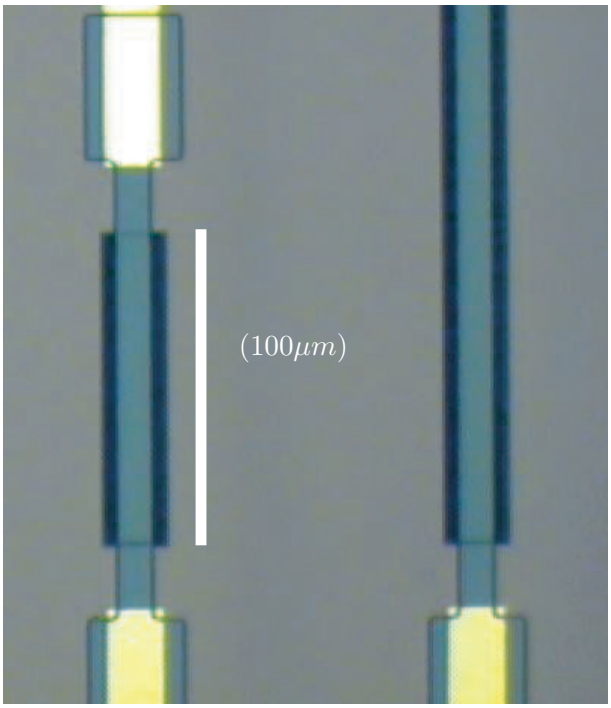

Figure 3.12: Pyrolyzed Parylene Free-standing Bridges

chrome/gold has been thermally evaporated and subsequently patterned. In this section, we discuss some issues associated with the fabrication of pyrolyzed-parylene MEMS devices. Figure 3.12 shows two free-standing bridges of pyrolyzed-parylene.

3.2.3.1 Adhesion

When depositing parylene on surfaces like silicon, silicon dioxide or some metals, the usual process includes an A-174 adhesion promotion step prior to deposition [21]. It was found that parylene films after pyrolysis had better adhesion if that step was *not* performed. In this study, all parylene films that were to undergo pyrolysis were deposited without the adhesion promotion step. For this reason, it is preferable to pattern pyrolyzed-parylene films *after* pyrolysis. Patterning parylene that was deposited without A174 lead to delamination problems when the photoresist is eventually stripped from the wafers (prior to pyrolysis). Adhesion to silicon and to silicon dioxide was found to be excellent. Patterned films of pyrolyzed parylene on silicon and silicon dioxide were able to withstand "agressive" processes such as RCA cleaning [22], diluted Hydrofluoric acid (HF), long exposure to Buffered HF (BHF), ultrasonic agitation, acetone rinsing and Tetramethyl Ammonium Hydroxide (TMAH) etching. The adhesion of metals to pyrolyzed-parylene is acceptable for MEMS processing, though not as good as that of pyrolyzed-parylene to silicon and silicon dioxide. Surface cleanliness is crucial for pyrolyzed-parylene therefore it is highly desirable to thoroughly clean any surface prior to depositing parylene. RCA-1 (NH_4OH:H_2O_2:H_2O, 1:1:5 at 75°C for 15 min) was found to be a good candidate for this purpose. Other possible techniques are BHF dip, oxygen plasma treatment or Piranha cleaning (H_2SO_4 : H_2O_2 4 : 1).

3.2.3.2 Patterning

Pyrolyzed-parylene is fully compatible with conventional lithography. Adhesion of photoresist on pyrolyzed-parylene was found to be satisfactory, whether or not hexamethyldisilazane (HMDS) treatment was used prior to photoresist spinning. Pyrolyzed-parylene can be etched by oxygen plasma using either a photoresist mask or a metal mask. The etching rate of pyrolyzed-parylene in an Reactive Ion Etching (RIE) reactor with an oxygen pressure of $200mTorr$, a flow of $40sccm$, and a power of $400W$ was studied. Table 3.5 shows the etching rates of different pyrolyzed-parylene films compared to photoresist and regular

Material	**Etching Rate** ($\mu m.min^{-1}$)	**Selectivity to Photoresist**
Photoresist	0.39	1
Parylene C	0.35	0.90
Parylene pyrolyzed @ 600°C	0.31	0.79
Parylene pyrolyzed @700°C	0.23	0.59
Parylene pyrolyzed @ 800°C	0.21	0.54

Table 3.5: Comparison of Etching Rates in RIE

parylene. It was mentioned already that for reasons related to adhesion, it is preferable to pattern pyrolyzed-parylene rather than pyrolyzing patterned parylene. Another reason is the selectivity of pyrolyzed-parylene etching vs. photoresist. If a $5\mu m$-thick parylene film is to be pyrolyzed, a photoresist film of at least $5.6\mu m$in thickness is required as a mask layer. On the other hand, if pyrolysis is performed first, the film will be $1\mu m$ and, according to the selectivity quoted in Table 3.5, the required photoresist mask thickness is $1.9\mu m$. Therefore, small patterns are easier to reach with the second scenario.

3.2.4 Mechanical Properties

3.2.4.1 Density

The properties of carbon films are strongly connected with their density [17]. For this reason, changes in density were calculated using previous results on weight loss and thickness change. Figure 3.13 shows the obtained densities for different films. There seems to be a discontinuity around 500°C corresponding to the beginning of the second phase of weight change. Scattering values between 500°C and 600°C seem to indicate a transient phase in the pyrolysis. The results in Figure 3.13 will be used to investigate relations between density and other properties in the following sections.

3.2.4.2 Young's Modulus and Stress

The Young's modulus and the stress of parylene-pyrolyzed carbon were evaluated using the diaphragm load-deflection tests. $20\mu m$-thick silicon diaphragms were fabricated on silicon wafers using Potassium Hydroxide (KOH) etching. Then, a $3\mu m$-thick parylene

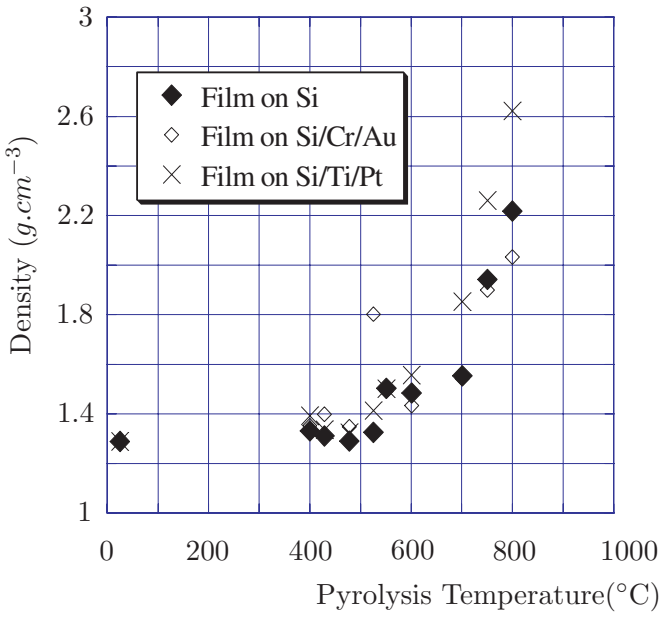

Figure 3.13: Density as a Function of Pyrolysis Temperature

C was deposited on the wafers and the $20\mu m$-thick silicon diaphragms were etched by Bromine Trifluordide (BrF_3) gas-phase etching, thus creating parylene membranes. Those membranes were finally pyrolyzed into carbon. The deformation of the carbon diaphragms as a function of applied pressure is studied according to the method described in [23]. Both Young's modulus and the stress are simultaneously obtained by fitting the resulting data to the load-deflection relationship reported [23]. Figure 3.14 shows the calculated Young's modulus and stress as a function of pyrolysis temperature. In the calculation, the poisson's ratio was assumed to be 0.4. The Young's modulus after the pyrolysis became $50GPa$ for 800°C pyrolysis (4.5°C.min^{-1} ramp rate). The stress also increased below 700°C, but showed a drop at 800°C.

3.2.4.3 Surface Properties

Film surfaces pyrolyzed at various temperatures were observed with an atomic force microscope. The measured surface roughness was below $5nm$ both for films pyrolyzed at 500°C and 800°C. However, the periodical length of roughness for the film at 800°C was longer than that for 500°C.

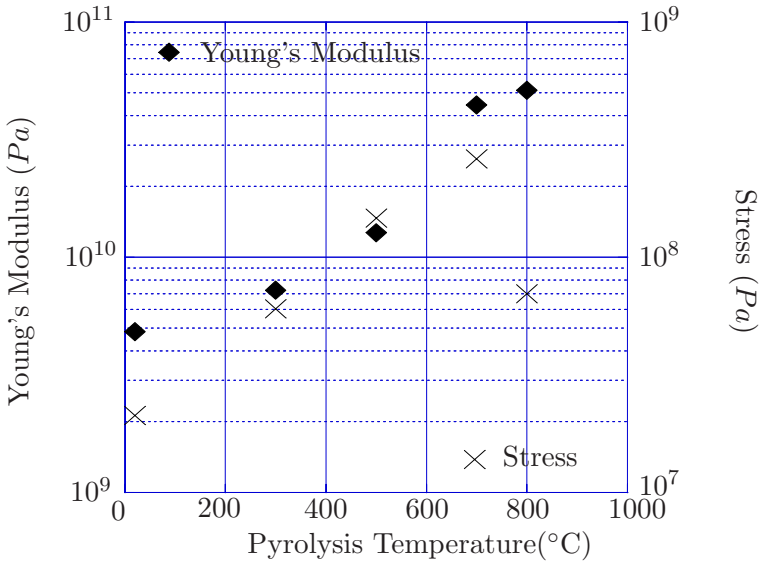

Figure 3.14: Young's Modulus and Stress

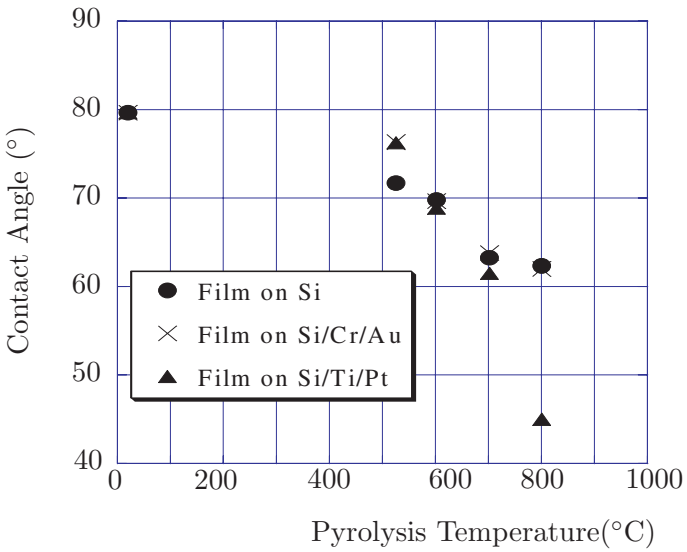

Figure 3.15: Contact Angle

3.2.5 Electrical Properties

3.2.5.1 Resistivity

The resistivity of pyrolyzed parylene films was measured using $1\mu m$-thick parylene C films pyrolyzed in N_2 atmosphere at different temperatures (up to 900°C). Conventional lithography and oxygen plasma etching (as discussed in Section 3.2.3.2) were used to define Van der Pauw structures or "Greek crosses" in the pyrolyzed-parylene films [24, 25]. Cr/Au electrodes were then deposited on top of these crosses. Figure 3.16 shows one of the fabricated crosses. By running a current from terminal A to terminal B and measuring the voltage between terminal D and terminal C, one can calculate the sheet resistance $\rho_{\square}$ in $\Omega/\square$ using Equation 3.1:

$$\rho_{\square} = \frac{\pi}{\ln 2}\frac{V_{DC}}{I_{AB}}. \tag{3.1}$$

An $HP4145B$ semiconductor parameters analyzer was used to sweep the current I_{AB} while measuring the voltage V_{DC}. The sheet resistance was then calculated by fitting the obtained $I-V$ characteristic. After the sheet resistance was calculated, the value of the resistivity was calculated using thickness t (which is a function of the pyrolysis temperature as well, as discussed in Section 3.2.2.1):

$$\rho = \rho_{\square} t. \tag{3.2}$$

The resistivity of parylene-pyrolyzed carbon as a function of pyrolysis temperature is shown in Figure 3.17. One set of samples was pyrolyzed using a ramping rate of $10°C.min^{-1}$ to the maximum temperature, while another set of samples was pyrolyzed using a ramping rate of $4.5°C.min^{-1}$. Parylene films pyrolyzed at temperatures below 600°C exhibit very high resistivity. The resistivity became less than $10^{10}\Omega.cm$ above 600°C and decreased to about $1*10^{-2}\Omega.cm$ at 900°C, which was close to $5*10^{-3}\Omega.cm$ reported for glassy carbons obtained above 1000°C[17]. The pyrolysis with a lower ramp rate led to a lower resistivity. However, it is impossible to know whether this is due to the ramping rate itself rather than to the fact that for a given maximum temperature, samples pyrolyzed with a lower ramping rate were subjected to high temperatures for a longer time. The behavior of pyrolyzed-parylene resistivity supports the conclusion of Section 3.2.2.4, as the resistivity of pyrolyzed-parylene gets closer to that of graphite when the pyrolysis temperature is increased. The resistivity of graphite on the c-axis is reported to be $3.5*10^{-3}\Omega.cm$ [26], which is a little less than one

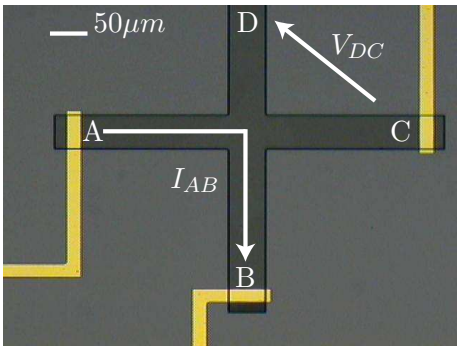

Figure 3.16: Sheet Resistance Test Structure

order of magnitude higher than the resistivity of parylene when pyrolyzed at 900°C (Figure 3.17).

3.2.5.2 Contact Resistance

The contact resistance of pyrolyzed-parylene to Ti/Au and Cr/Au electrodes was measured using a Kelvin structure [25]. Figure 3.18 shows one of the fabricated Kelvin structures. The contact resistance is calculated by flowing a current between terminals B and C while measuring the voltage drop between terminals A and D. Both positive and negative I_{BC} were applied using an HP4145b semiconductor parameter analyzer. It was found that both chrome/gold and titanium/gold contacts to pyrolyzed parylene exhibit ohmic behavior. Figure 3.19 shows V_{AD} vs. I_{BC} between titanium/gold and a film of pyrolyzed-parylene having a resistivity $\rho = 79.4\Omega.cm$. The contact resistance is calculated using Equation 3.3

$$\rho_c = \frac{V_{AD}}{A_c I_{BC}}, \tag{3.3}$$

where A_c is the contact area. Figure 3.20 shows the contact resistance between different films of pyrolyzed-parylene and titanium/gold. As one would naturally expect, the contact resistance to pyrolyzed-parylene depends the resistivity. The contact resistance obtained for films pyrolyzed at high temperature is comparable to that of aluminum contacts to highly-doped silicon [27]. Some preliminary tests with aluminum electrodes suggested that aluminum was not a good contact to pyrolyzed-parylene.

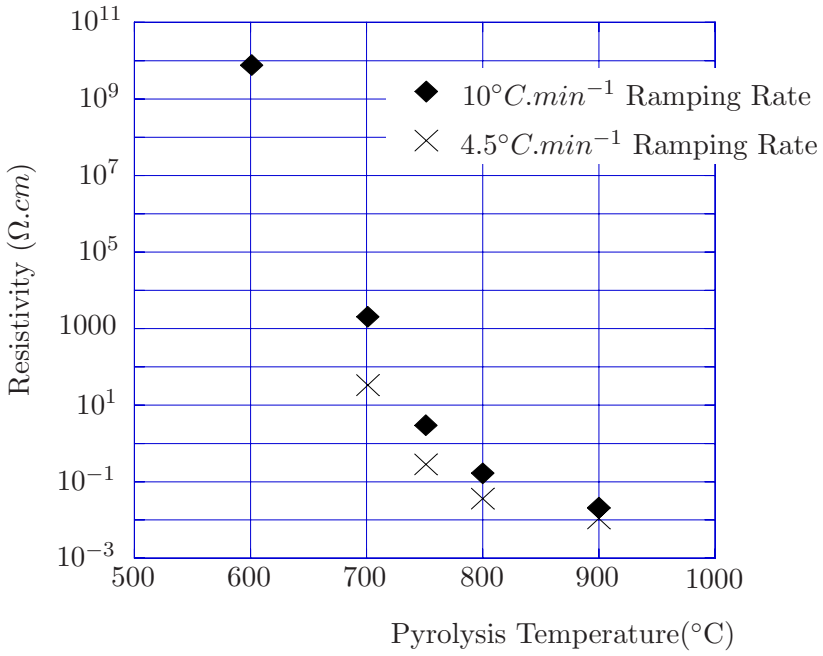

Figure 3.17: Pyrolyzed Parylene Resistivity as a Function of Pyrolysis Temperature

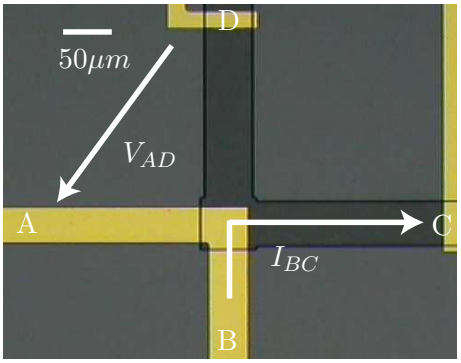

Figure 3.18: Contact Resistance Test Structure

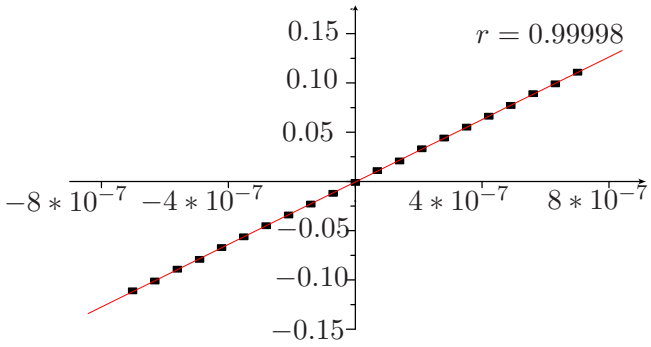

Figure 3.19: Contact Current-Voltage Characteristic

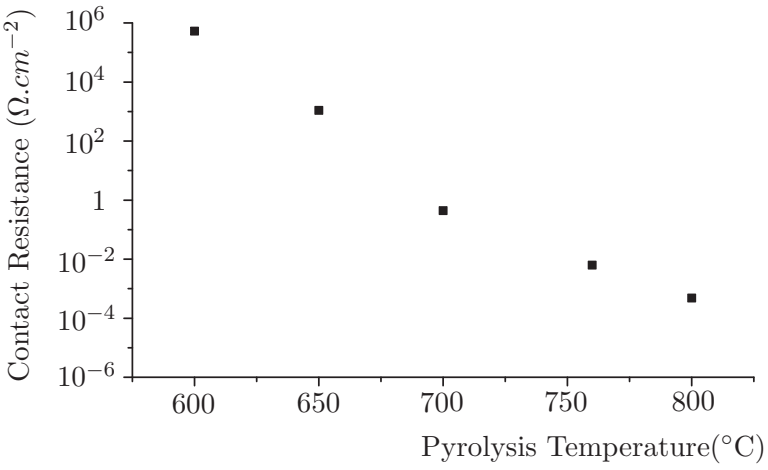

Figure 3.20: Contact Resistance as a Function of Pyrolysis Temperature

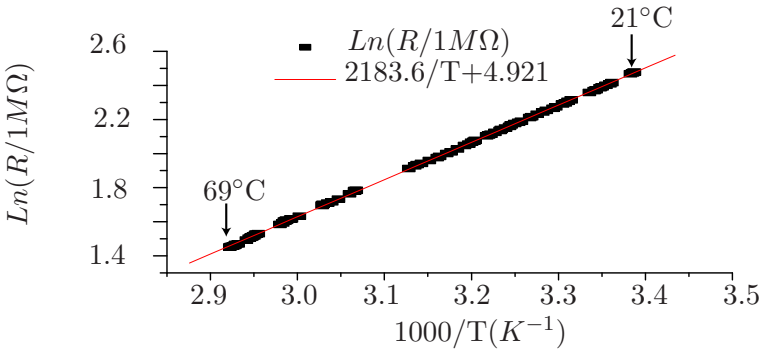

Figure 3.21: Temperature Dependence

3.2.5.3 Temperature Sensitivity

The temperature dependence of the conductivity of pyrolyzed parylene was measured in an oven with flowing N_2 using a precision thermocouple for temperature reference. The conductivity of all pyrolyzed-parylene films was found to exhibit an Arrhenius dependence:

$$\sigma = \sigma_0 \exp\left(-\frac{E_a}{kT}\right), \tag{3.4}$$

where E_a is the activation energy and T the temperature of the film. The temperature coefficient of resistance for materials following such a dependence is

$$\alpha = -\frac{E_a}{kT^2}. \tag{3.5}$$

Figure 3.21 shows the temperature dependance of a film of pyrolyzed parylene having resistivity $\rho = 1.9 * 10^3 \Omega.cm$ at room temperature. The extracted value of E_a/k is $2183.6K$. This corresponds to an activation energy of $0.19eV$ and a TCR at room temperature of $\alpha = -2.4\%.K^{-1}$. The TCR of pyrolyzed-parylene films can change by an order of magnitude depending on the room-temperature resistivity. This is a common feature among materials having high TCR and a resistivity that can be tuned by the fabrication process (such as amorphous silicon or vanadium oxide). Figure 3.22 shows the TCR of different pyrolyzed-parylene films pyrolyzed at different temperatures (therefore having different room-temperature resistivity). As can be seen on this figure, the TCR (and therefore the activation energy) has a logarithmic dependence on the room-temperature resistivity. Em-

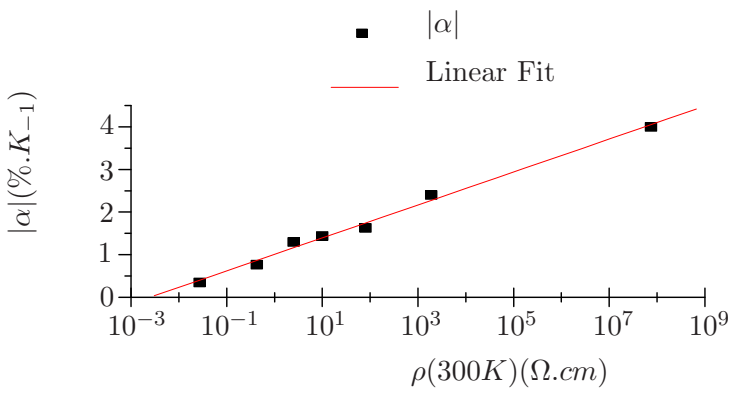

Figure 3.22: TCR Dependence on Resistivity

pirically, the TCR can be estimated to be

$$|\alpha|(K^{-1}) = 0.010712 + 0.0038671 \log(\rho(\Omega.cm)). \tag{3.6}$$

Even though the use of pyrolyzed-parylene as a bolometer material will be discussed in detail in Chapter 4, this is a good time to make some preliminary remarks. The evolution of TCR as a function of resistivity is very important when one considers candidates for bolometer materials. It is therefore useful to compare this evolution with that observed in other materials commonly used in bolometers. Figure 3.23 and Figure 3.24 show the relationship between the TCR and the room-temperature resistivity of VOx and amorphous silicon, respectively, from [28] and [29]. In [28], the expression of the TCR is calculated to be

$$|\alpha|(K^{-1}) = 0.03227 + 0.010556 * \log(\rho(\Omega.cm)). \tag{3.7}$$

In [30], Collier et. al. measured the resistivity temperature dependence of carbon rods having a resistivity $5 * 10^{-3}\Omega.cm < \rho < 5.5 * 10^{-3}\Omega.cm$ and graphite. The TCR at $300K$ was measured to be $\alpha = -0.032\%.K^{-1}$ while for graphite, the TCR around $300K$ was $0.5\%.K^{-1}$.

3.2.5.4 Humidity Sensitivity

It was mentioned in Section 3.2.2.2 that the weight of pyrolyzed-parylene films increased when their temperature was taken from 100°C to room temperature (20°C). To estimate

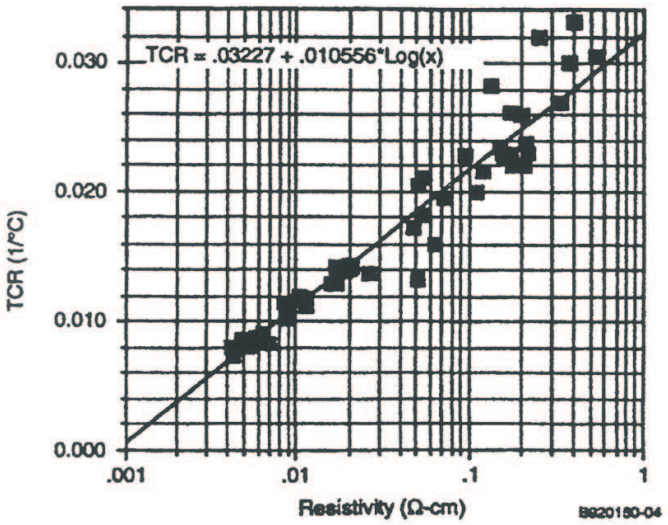

Figure 3.23: VOx TCR Dependence on Resistivity, after [28]

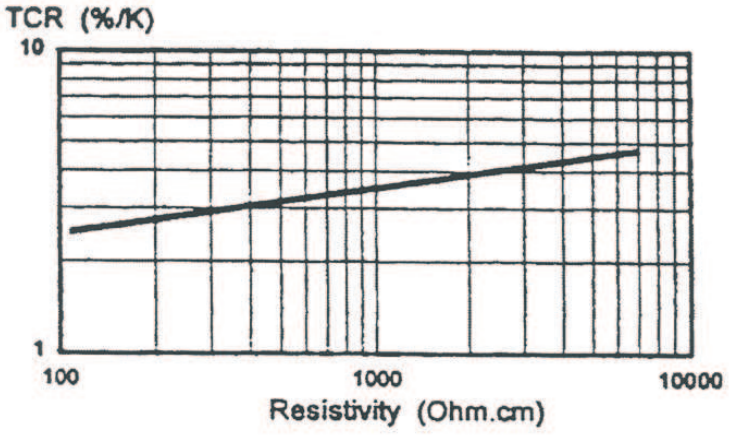

Figure 3.24: a-Si TCR Dependence on Resistivity, after [29]

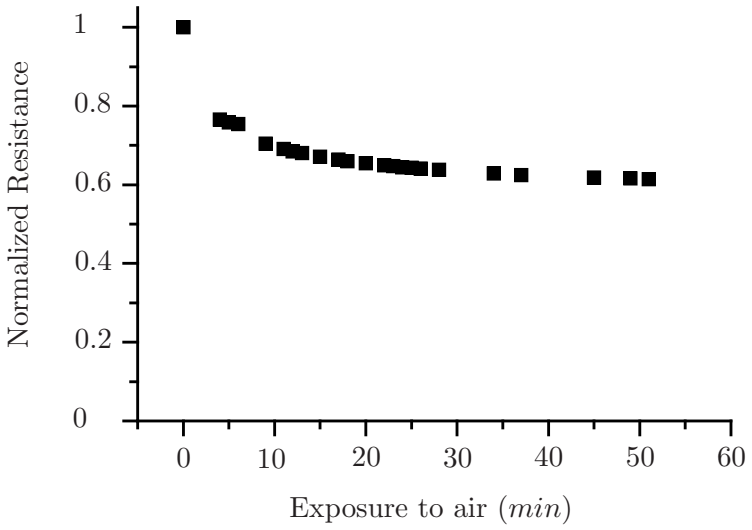

Figure 3.25: Pyrolyzed Parylene Resistance Change Upon Exposure to Air

the effect of humidity on the resistivity, a resistance made of a $1\mu m$-thick parylene film pyrolyzed at 650°C was placed into a vacuum chamber with flowing N_2 for 2 hours. Air was then allowed to flow into the chamber. Figure 3.25 shows the normalized resistance as a function of time since air started to fill the chamber.

In another experiment the resistance was measured in air with a temperature varying from 110°C to 20°C. A temperature-controlled chuck with heating and cooling capability was used in order to reach temperature set-points quickly. Figure 3.26 shows the resistance as a function of temperature. As can be seen on this figure the resistance starts to drop , around 36°C and at 20°C, the resistance is lower than what it was at 120°C. Since the drop starts at a temperature higher than the air temperature, this drop cannot be due to condensation on the surface and 20°C is still above the dew point (the relative humidity was estimated to be 60%). Measurement made in N_2 do not exhibit this drop (see Figure 3.21).

3.3 Conclusion

We have conducted a series of experiments involving the pyrolysis of parylene using different pyrolysis temperatures. Pyrolysis of parylene above 500°C leads to films of glassy carbon having a resistivity than can be tuned over an 11 orders of magnitude range depend-

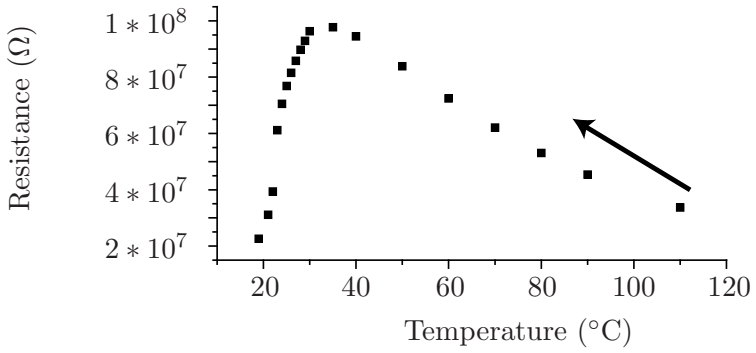

Figure 3.26: Pyrolyzed Parylene Resistance in Air

Parameter	Range
Density ($g.cm^{-3}$)	$1.3 < d < 2.2$
Young's Modulus (Pa)	$10^9 < E < 10^{10}$
Contact Angle (°)	$80 < \theta < 62$
Resistivity @300K ($\Omega.cm$)	$10^{-2} < \rho < 10^9$
Contact Resistance @300K ($\Omega.cm^{-2}$)	$10^{-4} < \rho_c < 10^6$
TCR ($\%.K^{-1}$)	$0.3 < \lvert\alpha\rvert < 4$

Table 3.6: Summary of Key Properties of Pyrolyzed Parylene

ing on the maximum temperature. Data suggests that after the pyrolysis occurs (around 500°C), films of pyrolyzed-parylene experience changes in structure and become more and more crystalline as the temperature is further increased. The TCR was found to be relatively high, between $-0.3\%.K^{-1}$ and $-4\%.K^{-1}$ depending on the pyrolysis temperature. We showed that pyrolyzed-parylene can easily be integrated into standard microfabrication processes. Lithography techniques and etching techniques can be used to pattern pyrolyzed films and to obtain free-standing structures. Table 3.6 summarizes some parameters of interest for pyrolyzed-parylene. The data shown in this chapter leads us to conclude that some properties of pyrolyzed-parylene make it attractive to be used in uncooled bolometers. Chapter 4 discusses such a device.

Bibliography

[1] S. C. S. Inc., "Parylene specifications and properties." http://www.scscookson.com/parylene_knowledge/specifications.cfm. xiv, 54, 56, 57, 58

[2] Specialty Coating Systems Cookson Inc., *PDS2010 Parylene Deposition System User's Manual*. 54

[3] Y. Xu and Y. Tai, "Selective deposition of parylene c for underwater shear-stress sensors," in *Digest of technical papers, Transducers'03, the 12th International Conference Solid-State Sensors, Actuators and Microsystems*, June 2003. 55

[4] E. Charlson and E. C. R. Sabeti, "Temperature selective deposition of parylene-c," *IEEE Transactions on Biomedical Engineering*, vol. 39, pp. 202–206, February 1992. 55

[5] M. Liger, D. Rodger, and Y. Tai, "Robust parylene-to-silicon mechanical anchoring," in *Proceedings of The 16th IEEE International MEMS Conference (MEMS'03)*, pp. 602–605, January 2003. 56

[6] C. Chiang and M. A. C. P. D. Fraser, "Challenges and issues of low-k dielectrics," in *Proceedings of Technical Papers, International Symposium on VLSI Technology, Systems, and Applications*, pp. 37–39, June 1997. 57

[7] M. Liger, N. Pornsinsirirak, Y. Tai, S. Ho, and C. Ho, "Large-area electrostatically-valved skins for adaptive flow control on ornithopter wings," in *Technical Digest, Solid State Sensor and actuator Workshop*, pp. 247–250, June 2002. 57

[8] T. Yao, K. Walsh, and Y. Tai, "Dielectrics charging effects on parylene electrostatic

actuators," in *Proceedings of the Fifteenth IEEE International Conference on Micro Electro Mechanical Systems (MEMS '02)*, pp. 614–617, January 2002. 57

[9] P. Chen, D. Rodger, M. Humayun, and Y. Tai, "Spiral-tube parylene intraocular pressure sensor," in *Digest of Technical Papers, 18th IEEE International Conference on MicroElectroMechanical Systems (MEMS 2005)*, (Miami FL), January-February 2005. 58

[10] J. Xie, J. Shih, Q. He, C. Pang, Y. Tai, Y. Miao, and T. Lee, "An integrated lc-esi chip with electrochemical-based gradient generation," in *Proceedings of the 17th IEEE International Conference on MicroElectroMechanical Systems (MEMS 2004)*, (Maastricht, The Netherlands), pp. 334–337, January 2004. 58

[11] Wiktionary, "pyrolysis." http://en.wiktionary.org/wiki/pyrolysis. 58

[12] T. Edison, "Electric lamp," January 1880. US Patent 223,898. 58

[13] G. Learmont, L. Nabi, G. Bramham, and J. Bailey, "Pyrolyzis of phenol-formaldehyde resins .1.," *Plastics & Polymers*, vol. 37, no. 129, pp. 201–, 1969. 58

[14] M. Inagaki, T. Ibuki, and T. Takeichi, "Carbonization behavior of polyimide films with various chemical structures," *Journal of Applied Polymer Science*, vol. 44, pp. 521–525, january 1992. 58

[15] O. Schueller, S. Brittain, C. Marzolin, and G. Whitesides, "Fabrication and characterization of glassy carbon mems," *Chem. Mater.*, vol. 9, pp. 1399–1406, 1997. 58

[16] J. Kim, X. Song, K. Kinoshita, M. Madou, and R. White, "Electrochemical studies of carbon films from pyrolyzed photoresist," *J. Electrochem Soc*, vol. 145, July 1998. 58

[17] S. Ranaganathan, R. McCreery, S. M. Majji, and M. Madou, "Photoresist-derived carbon for microelectromechanical systems and electrochemical applications," *Journal of The Electrochemical Society*, vol. 147, no. 1, pp. 277–282, 2000. xiv, 58, 59, 67, 70

[18] T. Wang and A. Lal, "Suspended carbon bridges as onchip tunable resistors," in *Digest of Technical Papers, The 10th International Conference of Solid-State Sensors and Actuators (transducers'99)*, (Sendai, Japan), June 1999. 59

[19] E. Hui, C. Keller, and R. Howe, "Carbonized parylene as a conformal sacrificial layer," in *Technical Digest of the 8th Solid-State Sensor and Actuator Workshop*, pp. 256–260, 1998. 59

[20] S. Miserendino, S. Boland, and Y. C. Tai, "Material and electrochemical properties of pyrolyzed parylene-c," in *206th Meeting of the Electrochemical Society*, October 2004. xii, 61, 63, 64

[21] S. C. S. Inc., "Product specifications, a-174 silane promotion." 66

[22] W. K. W and D. Puotinen, "Cleaning solutions based on hydrogen peroxide for use in silicon semiconductor technology," tech. rep., 1970. 66

[23] O. Tabata, K. Kawahata, S. Sugiyama, , and I. Igarashi, "Mechanical property measurements of thin-films using load deflection of composite rectangular membranes," *Sensors and Actuators*, vol. 20, pp. 135–141, 1989. 68

[24] L. van der Pauw, "A method of measuring the resistivity and hall coefficient of lamellae of arbitrary shape," tech. rep., Philips, 1958. 70

[25] A. Walton, "Microelectronic test structures," tech. rep. 70, 71

[26] Cutnell and Johnson, *Physics 4th ed.* Wiley and Sons. 70

[27] S. Sze, *Physics of Semiconductor Devices, Second Edition.* John Wiley and Sons, 1981. 71

[28] B.Cole, R.Horning, B.Johnson, K. Nguyen, P. Kruse, and M. Foote, "High-performance infrared detector arrays using thin film microstructures," in *Proceedings of the Ninth IEEE International Symposium on Applications of Ferroelectrics.ISAF'94*, pp. 653–656, August 1991. xii, 75, 76

[29] E. Mottin, A. Bain, J. Martin, J. O.-B. S.Bisotto, J. YON, and J. Tissot, "Uncooled amorphous silicon technology enhancement for 25μm pixel pitch achievement," *Infrared Technology and Applications XXVIII, SPIE*, vol. 4820, 2002. xii, 75, 76

[30] L. J. Collier, W. S. Stiles, and W. G. A. Taylor, "The variation with temperature of the electrical resistance of carbon and graphite between 0° c. and 900° c.," *Proceedings*

of the Physical Society, vol. 51, no. 1, pp. 147–152, 1939. http://stacks.iop.org/0959-5309/51/147. 75

Chapter 4

Uncooled Pyrolyzed-Parylene Carbon Bolometer

Introduction

This chapter presents a novel uncooled, all-parylene bolometer. The device is made of two layers of pyrolyzed parylene and a metal layer for interconnections only. We demonstrate that high responsivity can be achieved by tailoring the electrical conductivity and the TCR using different pyrolysis conditions for each parylene layer.

4.1 Design

Figure 4.1 shows a typical resistive uncooled bolometer: a free-standing temperature-sensitive element is linked to a substrate by low thermal conductance legs. Equations 2.27 and 2.65 show the expression of the DC responsivity and the NETD of such a device (Chapter 2):

$$\Re(V.m^{-1}) = \frac{\Delta V(\Phi)}{\Phi} = \frac{\alpha \eta R_0 I_b}{G_{th}}, \tag{2.27}$$

$$NETD(K) = \frac{4F^2 V_n}{A_d \Re\left(\frac{dM}{dT}\right)_{T,[\lambda_1-\lambda_2]}}, \tag{2.65}$$

where α is the TCR of the sensing element, R is the bolometer resistance, G_{th} is the pixel-to-substrate thermal conductance, and η is the bolometer absorptivity. The thermal time constant is given by Equation 2.31:

$$\tau_{th} \equiv \frac{C_{th}}{G_{th}}, \tag{2.31}$$

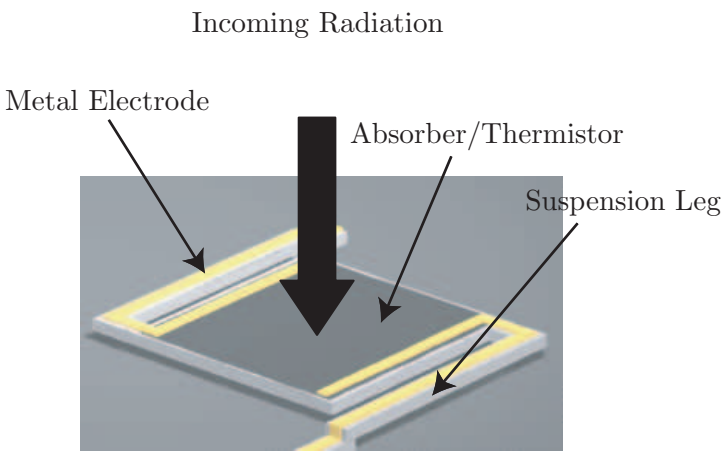

Figure 4.1: Typical Bolometer Design

where C_{th} is the thermal capacitance. The key parameters to obtain good responsivity are: high TCR α, low G_{th} and low voltage noise V_n. However, as we try to decrease the thermal conductance, we must be able to decrease the thermal capacitance, as failure to do so would result in unacceptably high thermal time constant. To be useful for thermal imaging with a video frame rate ($30Hz$), the thermal time constant should be kept below $30ms$.

The suspension legs are usually made of silicon nitride or polysilicon. In the case of silicon nitride legs, it is necessary to have another layer for electrical conduction.

Most uncooled bolometers use vanadium oxide (VOx) [1] or amorphous silicon (a-Si) [2] as the temperature-sensitive material, reaching a TCR of about 1.5% to 3%[3]. Another possible material is yttrium-barium-copper oxide (YBaCuO), also reaching TCRs as high as 3% at room temperature [4].

As shown in Chapter 3, the electrical resistivity of pyrolyzed parylene can be adjusted over a very wide range (from at least $10^{10}\Omega.cm$ down to $10^{-2}\Omega.cm$), while the TCR of such films varies between $0.3\%.K_{-1}$ and $4\%.K^{-1}$. We also showed in Chapter 3 that free-standing structures of pyrolyzed-parylene can be achieved.

Carbon was already being used as a detector material in cooled bolometers several decades ago. In 1959, W.S. Boyle and K.F. Rodgers reported a cooled carbon bolometer made of a "thin" layer of carbon ($48\mu m$) and having an area of $19mm^2$. The obtained responsivity was $\Re = 10^4 V.W^{-1}$ and the detectivity was $D^* = 4.25 * 10^{10}$[5]. In 1965

Shepard described a similar experiment, reaching a responsivity of $\Re = 2.1 * 10^4 V.W^{-1}$[6].

In this work we propose a carbon bolometer using pyrolyzed parylene both for the temperature-sensing element and for the suspension legs. To the author's best knowledge, this is the first time a micromachined carbon bolometer and micromachined carbon bolometer array are reported.

Figure 4.2 shows the proposed design. Since our ultimate goal is to build an uncooled infrared camera, some bolometers had a geometry similar to that shown on Figure 4.1. There are major differences with the typical "textbook" bolometer design:

- The temperature-sensing element is made of parylene pyrolyzed at low temperature, leading to a high resistivity and high TCR.
- The suspension leg is made of parylene pyrolyzed at high temperature, leading to a low resistivity.

There are a number of advantages to this design compared to the traditional design.

- The fabrication process is very simple.
- The bolometer is self-supporting, there is no "dead" thermal conductance or thermal capacitance due to a supporting layer.
- There is no need for a quarter-wavelength cavity, the wavelength range is extended.
- The suspension legs participate in the absorbtion of incoming radiation.
- There are no positive-TCR metal electrodes, and all section of the bolometer have a negative TCR.

The main disadvantage of this design the fact that is not compatible with Complementary Metal-Oxide-Semiconductor (CMOS) or bipolar circuits due to the high-temperature required for parylene pyrolysis. Only hybrid integration with electronic circuitry is possible.

We chose $-2\%.K^{-1}$ as the target TCR, a value comparable to that found in typical semiconducting bolometers [1, 7]. For such a TCR, the second layer of parylene must have a resistivity on the order of $10^2 \Omega.cm$. Therefore the target thickness of the pyrolyzed parylene film was chosen to be 2000Å. The obtained sheet resistance will then be $\rho_\square \sim 5M\Omega$. In

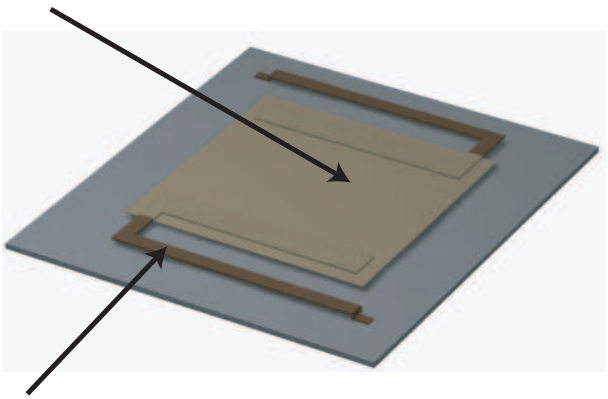

Figure 4.2: Two-level Pyrolyzed-Parylene Bolometer Design

theory, it would be possible to use only one layer of high-resistivity pyrolyzed parylene layer, serving both as thermistor and suspension; however, this would lead to an unreasonable bolometer resistance. We chose the resistivity of the suspension layer to be in the order of $10^{-2}\Omega.cm$ and its thickness to be 8000Å. The sheet resistance for such a resistivity and thickness is $\rho_{\square} \sim 125\Omega$. The absorber size was chosen to be $50*50\mu m^2$. The total bolometer resistance is given by

$$R = 2R_{leg} + R_{pixel}. \tag{4.1}$$

The number of resistance squares (ratio between length and width) of the absorber region is 1. Bolometers with different suspension geometry were designed with lengths ranging from $50\mu m$ to $170\mu m$, while the width was constant and equal to $5\mu m$. The number of resistance squares for these suspension dimensions is therefore between 20 to 68. Given the ratio of resistivity between the two layers of pyrolyzed-parylene, the resistance of the absorber area is three orders of magnitude higher than the suspension legs. Therefore, the total bolometer resistance is by far dominated by the absorber area. This ensures a higher relative change in resistance $\Delta R/R$ for a given absorbed radiant flux. Even though the responsivity is proportional to the absolute change of resistance ΔR, a higher relative change in resistance is easier to measure using either a voltmeter or an analog-to-digital converter (ADC).

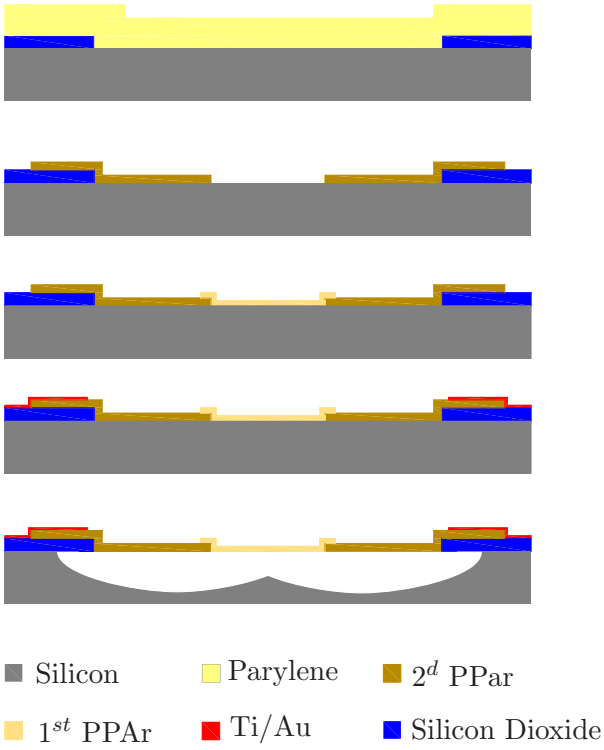

Figure 4.3: Fabrication Process Flow

4.2 Fabrication

4.2.1 Process Flow

The device process, as shown in Figure 4.3, begins with a 5000Å oxide growth and patterning. A $3\mu m$-thick parylene-C layer is then deposited and pyrolyzed in a nitrogen atmosphere. The temperature is raised to 800°C at 10°C/min and then cooled to room temperature at 2°C/min. The resulting film is patterned to define the suspension legs. The pyrolyzed-parylene etching is done in a Technics PEIIA plasma etcher with $400W$ of power and an O_2 pressure of $200mT$. A $1.4\mu m$ layer of AZ1518 photoresist is used as mask. A second layer of parylene ($0.8\mu m$) is deposited and pyrolyzed at 660°C at 10°C/min. For better repeatability, the samples are being kept at the maximum pyrolysis temperature for 2 hours. The second layer of pyrolyzed parylene is patterned to define the pixel area. Next, a Ti/Au interconnection layer (60Å/2000Å) is evaporated and patterned by wet etching using photoresist as a mask. Finally, the bolometers are released by Xenon Difluoride (XeF_2) gas-phase etching. In order to fully release the bolometers, an etch depth of $25\mu m$ should

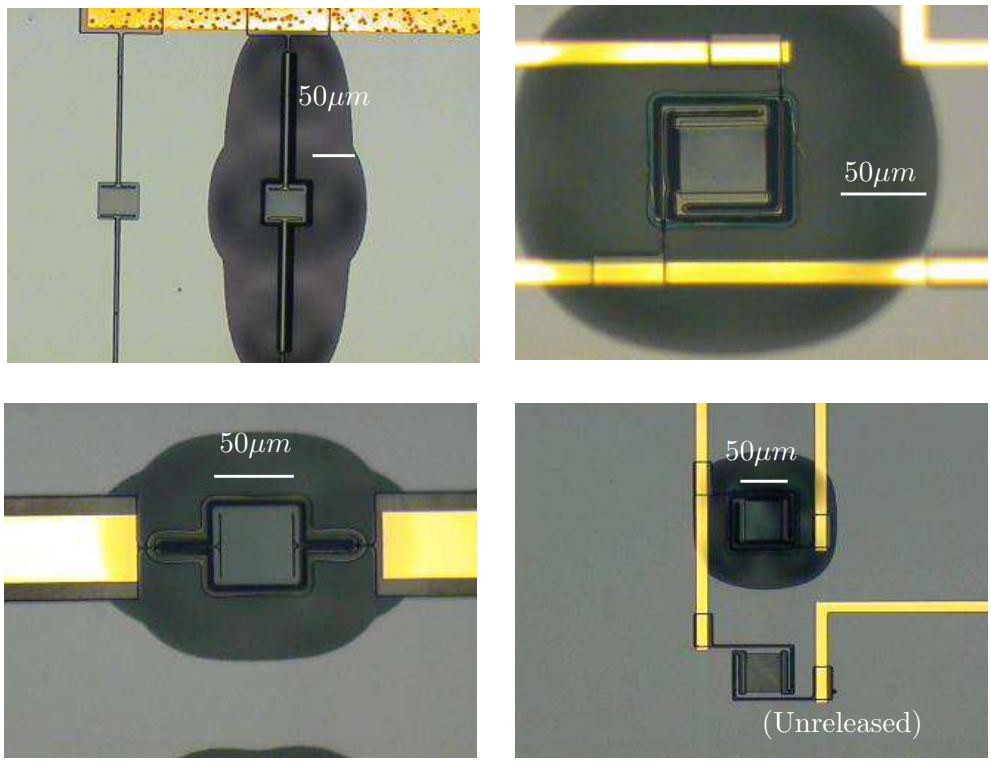

Figure 4.4: XeF2-Released Fabricated Pyrolyzed-Parylene Bolometers

be sufficient. However, due to a slight anisotropy of XeF_2 etching, we used an etch depth of about $60\mu m$. Figure 4.4 shows some fabricated devices.

4.2.2 Processing Issues

Typically, parylene depositions involve a prior coating of A174 for adhesion promotion [8]. However, it was found that this procedure leads to poor adhesion of the films after pyrolysis. On the other hand, the adhesion of pyrolyzed parylene on SiO2/Si wafers that have not been coated with A174 was excellent. This is also part of the reason why we chose to pattern the parylene after pyrolysis rather than the opposite. It was also observed that pyrolysis of pattern parylene leads to undesirable border effects, probably due to the pyrolysis-induced stress. Finally, due to the isotropic etching, patterning the parylene after it has been shrunk (4 to 5 times) by pyrolysis minimizes undercut. As mentioned earlier, for a good adhesion between the pyrolyzed-parylene films and the substrate it is crucial that the substrate be clean prior to parylene depositions. Therefore, an RCA-1 cleaning was performed before each parylene deposition. As can be seen on Figure 4.3, the second layer

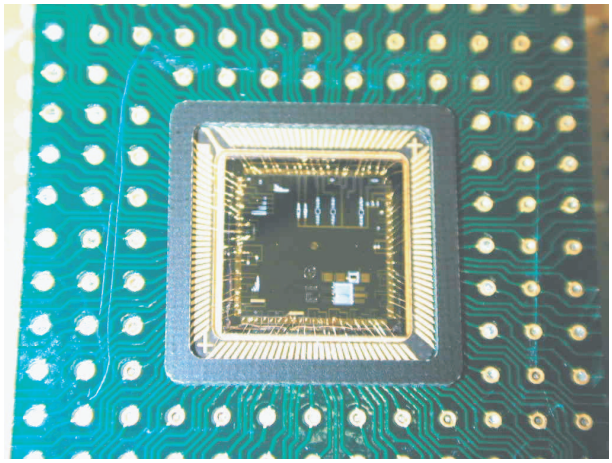

Figure 4.5: Bolometer Chip Wire-bonded in PGA Package

of parylene is directly in contact with first layer. No etch-stop layer can be used because the two layers of parylene must be in electric contact. Therefore, the etching of the second layer of parylene must be timed accurately to avoid etching the first layer of parylene as well.

4.3 Results

4.3.1 Electric Parameters

First, the bolometer chips were mounted in a Pin-Grid Array (PGA) package and wire bonded (Figure 4.5). The respective sheet resistance of both pyrolyzed layers were measured using van der Pauw "Greek-cross" structures [9] and an Hewlett-Packard HP4145B semiconductor parameters analyzer as a current source and voltage monitor. The contact resistance between the pyrolyzed parylene layers and titanium/gold was measured using Kelvin structures [10], again using an HP4145B semiconductor parameters analyzer as a current source and voltage monitor. The contact between the layers of pyrolyzed parylene and titanium/gold was found to be ohmic with a specific contact resistance of $3.5*10^{-3}\Omega.cm^2$ for the first layer and $3.5\Omega.cm^2$ for the second layer. The TCR of the second parylene layer was measured in a oven with flowing N_2 to avoid having measurement errors to humidity (see Section 3.2.5.4). The TCR around room temperature was measured to be $-1.63\%/K$. Table 4.1 shows different characteristics of interest for the two pyrolyzed-parylene layers.

	1^{st} Layer	2^{d} Layer
Pyrolysis Temperature (°C)	800	660
Holding Time (min)	0	120
Thickness before pyrolysis	$3\mu m$	$0.8\mu m$
Thickness after pyrolysis	$0.6\mu m$	$0.2\mu m$
Sheet Resistance ($\Omega.cm^{-2}$)	456	$3.97 * 10^{6}$
Resistivity ($\Omega.cm$)	$2.74 * 10 - 2$	79.4
TCR ($\%.K^{-1}$)	-0.35	-1.63

Table 4.1: Pyrolyzed-Parylene Parameters of Interest

The ratio between the sheet resistance of the first and the second layer is $8.7 * 10^{3}$. Therefore, for the chosen geometries, the total resistance of the bolometers is indeed dominated by the temperature-sensing element obtained from the second layer of pyrolyzed parylene.

4.3.2 Thermal Properties

The bolometers were placed in a vacuum chamber at $10mTorr$ and stabilized for several hours to eliminate any potential moisture-related drift. Current-voltage characteristics of bolometers were measured with an HP4145B working as a voltage source and current monitor. A hold time of 1 second was used at each bias to ensure thermal steady-state. Figure 4.6 shows the IV curve for a $50\mu m * 50\mu m$ bolometer with two $5\mu m * 170\mu m$ suspensions beams. The upward curvature seen on this figure clearly shows that the bolometers are self-heating (the TCR of pyrolyzed-parylene being negative). Unreleased bridges on SiO_2 do not exhibit this self-heating. Figure 4.7 shows the resistance and temperature rise as a function of input power. The temperature rise is calculated from the resistance change and TCR. We then extract the corresponding thermal conductance $G_{th} = 5.43 * 10^{-8} W.K^{-1}$. It should be noted that this extracted thermal conductance includes the radiation conductance, given by

$$G_{rad} = 8A_d\sigma\eta T^3. \tag{2.24}$$

For an absorptivity $\eta = 1$, the radiation conductance of a bolometer having area $50 * 50\mu m^2$ is $G_{rad} = 3.1 * 10^{-8} W.K^{-1}$.

An additional test was performed at higher pressure to make sure the measured thermal

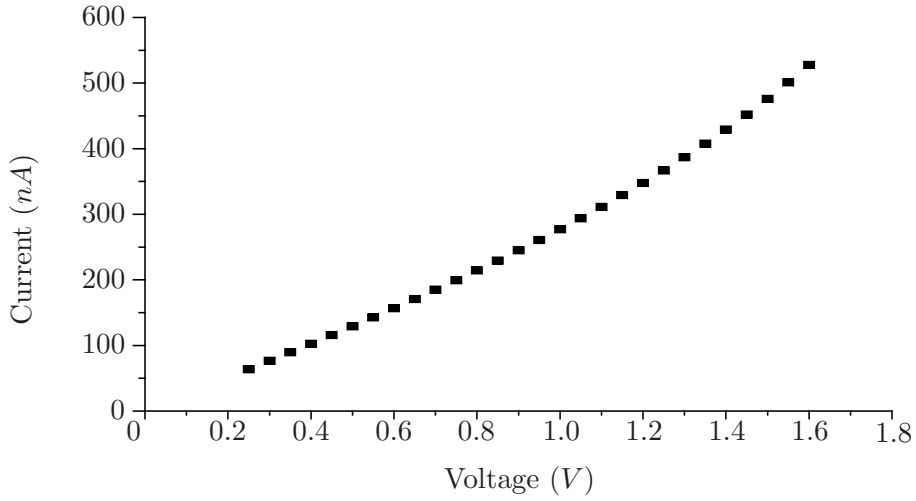

Figure 4.6: Bolometer I-V Characteristic

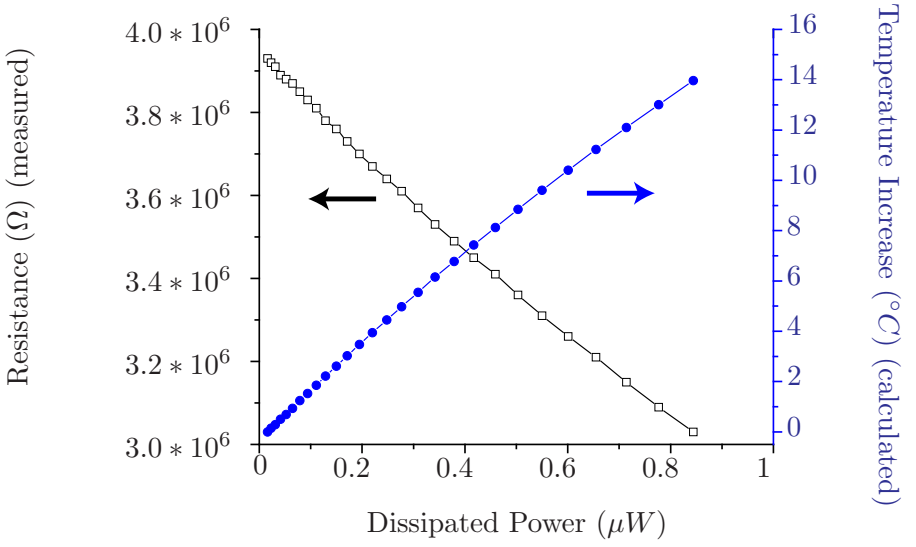

Figure 4.7: Bolometer Electrothermal Behavior

conductance was indeed that of the suspension legs. The thermal conductivity of an ideal gas is given in Equation 4.2 [11]

$$\kappa = \frac{n\bar{l}\bar{v}C_v}{3}, \tag{4.2}$$

where n is the density, $\bar{l}$ is the mean free path, $\bar{v}$ the mean particle velocity, and C_v the specific heat. The thermal conductivity of nitrogen (usually assumed to be the same as air) is $\kappa = 0.026\, W.m^{-1}.K^{-1}$. One may intuitively think that heat conductivity is proportional to density or at least decreases with decreasing density: such an intuition would be wrong. The expression of the mean free path is

$$\bar{l} = \frac{1}{\sigma_c n}, \tag{4.3}$$

where σ_c is the cross-sectional area for the gas considered. Since the mean free-path is inversely proportional to density, Equation 4.2 can be reduced to

$$\kappa = \frac{\bar{v}C_v}{3\sigma_c}. \tag{4.4}$$

Therefore, the thermal conductivity of a ideal gas is independent of pressure. However, this is only true as long as the mean free-path is much larger than the dimensions of the system considered [1, 12]:

$$\bar{l} = \frac{50\mu m}{p(Torr)}. \tag{4.5}$$

Therefore for a pressure $p = 10mTorr$ the mean free path is $5mm$, which is much larger than the gap between the bolometers and the bottom of the cavity.

The bolometers were then placed into a vacuum oven at $100Torr$ with bleeding N_2. The evolution of the bolometers resistance as a function of input power was measured, in an experiment similar to that described above. Figure 4.8 and 4.9 show the obtained electrothermal behavior of bolometers whose suspensions are $170\mu m * 5\mu m$ and $70\mu m * 5\mu m$, respectively. The thermal conductance of both pixels is two orders of magnitude higher than that measured at a pressure of $10mTorr$. The expected thermal conductance for a gap $d = 50\mu m$ and an absorber area of $A_d = 50\mu m * 50\mu m$ is

$$G_{th} = \kappa\frac{A_d}{d} = 1.3 * 10^{-6}(W.K^{-1}). \tag{4.6}$$

The measured thermal conductances are a few times higher than the calculated ones, which may be due to convection.

4.3.2.1 Thermal Conductivity

Next the bolometers were placed in a vacuum chamber with having a Zinc Sulfide (ZnS, also called Cleartran®) window obtained from ISP Optics.[1] The chamber was pumped down to a pressure below $20mTorr$. ZnS has an external transmittance between 60% and 70% from $0.5\mu m$ to $14\mu m$. A calibrated pyroelectric detector was was used to estimate the absorptivity of the bolometers. An IR-55 thermal infrared source obtained from Boston Electronics.[2] was used to produce pulsed infrared radiation. The infrared source was biased with a square wave at $15Hz$ with 50% duty cycle. The bolometers were biased with a constant current of $300nA$. A Stanford Research Systems[3] SR785 dynamic signal analyzer was used as a spectrum analyzer to observe the $15Hz$ voltage component. The signal was then compared to that of a $P1-71$ precision pyroelectric detector obtained from Coherent Incorporated.[4] (formerly Molectron) under the same conditions. The pyroelectric detector was calibrated by the manufacturer and the given responsivity at $15Hz$ was $7.09*10^4V.m^{-1}$ (after the built-in amplification). The absorptivity was estimated to be around 0.6 (assuming the same amount of radiation was indeed incident on both the bolometer and the pyroelectric detector). The radiation conductance for such a absorptivity is $G_{rad} = 1.86*10^{-8}W.K^{-1}$. The corresponding G_{leg} for the bolometer having a suspension $5\mu m * 170\mu m$ is $G_{leg} = 3.57*10^{-8}W.K^{-1}$. From this value, we estimated the thermal conductivity of the suspension legs:

$$\begin{aligned} G_{leg} &= 2\frac{\kappa tw}{L}, \\ \kappa &= \frac{G_{leg}L}{2tw} \\ \kappa &= 0.76W.m^{-1}.K^{-1}. \end{aligned}$$

The thermal conductivity reported here is about two times lower than the conductivity reported in [13]. This is because in [13] the calculation was made without taking the

[1] http://www.ispotics.com
[2] http://www.boselec.com/
[3] http://www.thinksrs.com
[4] http://www.coherent.com

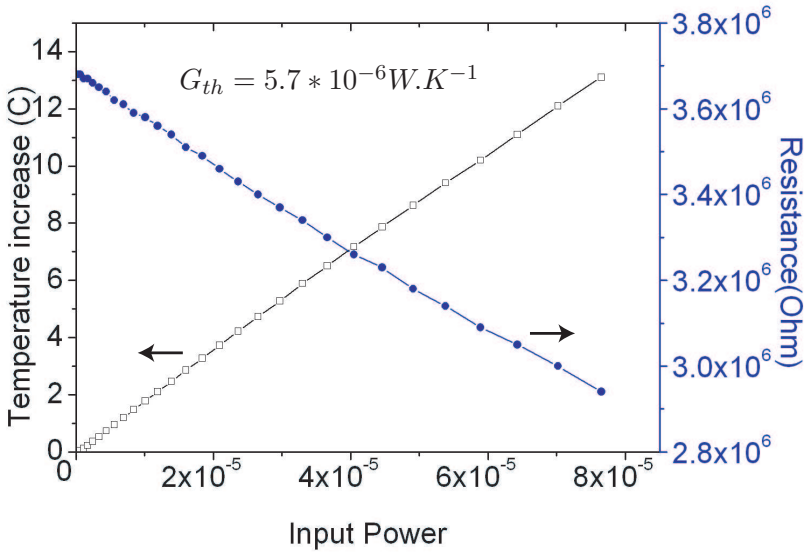

Figure 4.8: Bolometer Electrothermal Behavior at $100 Torr$

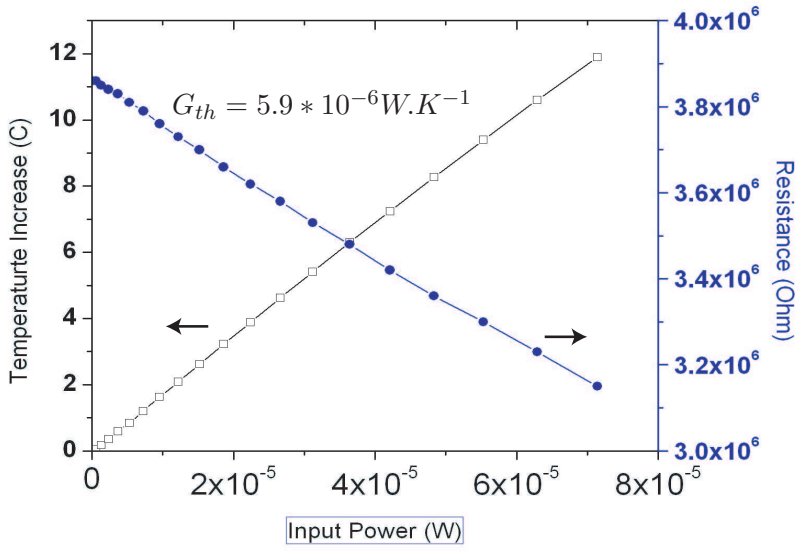

Figure 4.9: Bolometer Electrothermal Behavior at $100 Torr$

radiation conductance into account. Therefore, the calculation made here is more accurate. However, as mentioned before this calculation relies on the estimation of the absorptivity, which is only a rough estimation. This is lower than than values reported for silicon nitride deposited using Plasma Enhanced Chemical Vapor Deposition (PECVD) [14, 15], with the major advantage of providing electrical conductivity. It is also one order of magnitude lower than polysilicon. [16].

4.3.2.2 Thermal Capacitance and Thermal Capacity

An optical chopper wheel was used to measure the thermal time constant of the bolometers. The bolometers were biased with a constant current of $300nA$. A Stanford Research Systems[5] SR785 dynamic signal analyzer was used as a spectrum analyzer to observe fundamental voltage component for different chopping frequencies. As expected from the theory, the bolometers exhibit a first order response, as shown in Figure 4.10. The corresponding time constant is extracted to be be $\tau_{th} = 12.9ms$. From this value and that of the thermal conductance, we calculate the thermal capacitance C_{th}, the volumic heat capacity C_v, and the specific heat C.

$$\begin{aligned} C_{th} &= \tau_{th} G_{th} = 1.2 * 10^{-9} J.K^{-1}, \\ C_v &= \frac{C_{th}}{A_d t} = 2.3 J.cm^{-3}, \\ C &= \frac{C_v}{d} = 1.5 J.g^{-1}, \end{aligned}$$

where $t = 0.2\mu m$ is the thickness of the absorber and d the density. Using a result from Section 3.2.4.1 we chose to assume $d = 1.5g.cm^{-3}$

4.3.3 Noise

The $1/f$ noise of bolometers having a resistance $1.5M\Omega$ was measured using low-noise amplifiers and a Stanford Research Systems[6] SR785 dynamic signal analyzer to measure the low-frequency power spectral density. Batteries were used as power supply to avoid introducing additional noise, and the whole circuit was put in a metal enclosure. The internal voltage source of the SR785 was used to generated different voltage biases. The

[5] http://www.thinksrs.com
[6] http://www.thinksrs.com

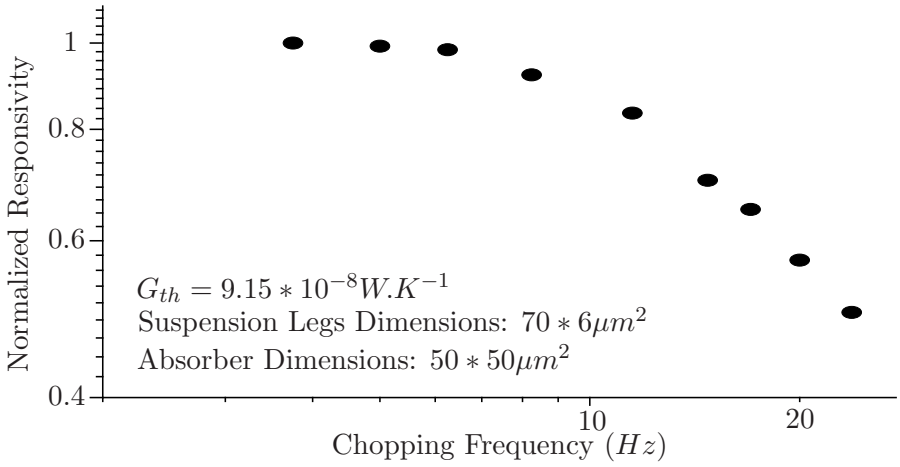

Figure 4.10: Bolometer Dynamic Response

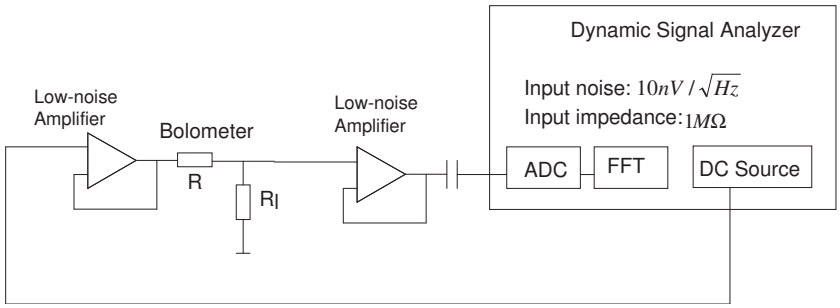

Figure 4.11: $1/f$ Noise Measurement Setup

input-referred noise of the instrument is $10nV.Hz^{-1/2}$ when used in its small input range ($-50dBV_{pk}$). Therefore, the circuit was connected to the dynamic signal analyzer with a $1\mu F$ capacitor in order to be able to use that range. The instrument having an input impedance of $1M\Omega$, the cut-off frequency of the high-pass filter is $0.16Hz$. Figure 4.11 shows the measurement circuit. The noise power contributions of both the amplifiers and the dynamic signal analyzer are both on the order of $10^{-16}V^2.Hz^{-1}$, one order of magnitude lower than the Johnson noise contribution of each resistor ($4.14*10^{-15}V^2.Hz^{-1}$). Assuming we can ignore the contributions from the amplifiers and from the dynamic signal analyzer, the noise power measured by the instrument is

$$S_{measured}(f) = kTR + kTR_l + \frac{S_f(f)}{4}, \tag{4.7}$$

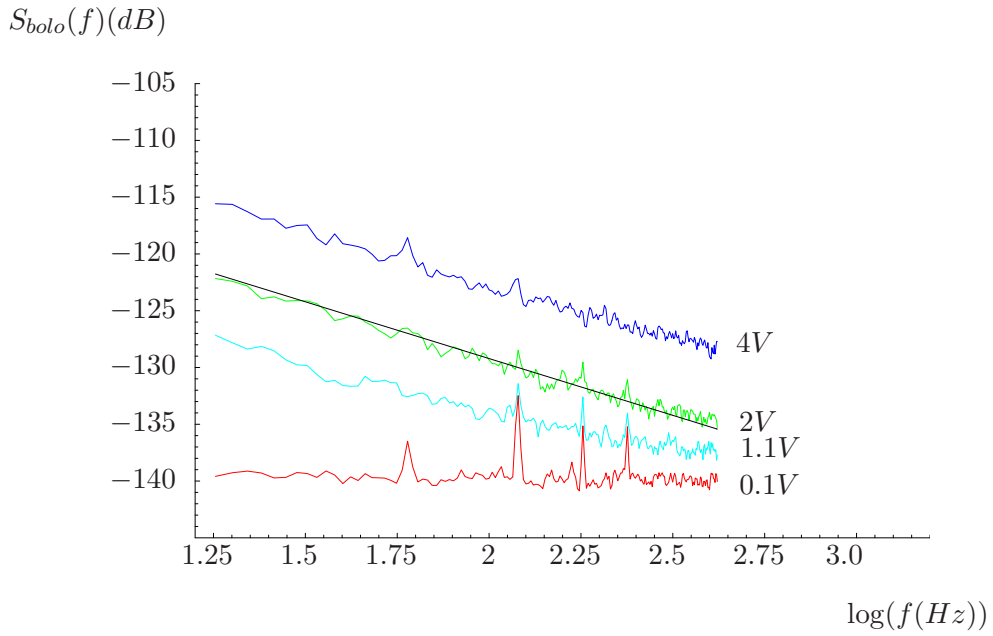

Figure 4.12: Bolometer $1/f$ Noise Power Spectrum

where R_l is the load resistor, R is the bolometer resistance, and $S_f(f)$ is the $1/f$ noise power spectral density. The load resistance R_l is chosen to match the bolometer resistance of the bolometer (to reach optimum power transfer). In this experiment, the bolometer resistance was $1.5M\Omega$. Figure 4.12 shows the noise power spectrum S_{bolo} generated by the bolometer for biasing voltages between $0.1V$ and $4V$, with

$$S_{bolo} = 4 * (S_{measured} - kTR_l). \tag{4.8}$$

As can be seen on Figure 4.12, at $V_b = 0.1V$, the noise is dominated by Johnson noise. The level of this Johnson noise was extracted to be $2.8 * 10^{-14}V^2.Hz{-}1$. This is more than the expected value $4kTR = 1.66 * 10^{-14}V^2.Hz{-}1$. Thinking it could be because the noise added by the amplifier and/or the dynamic signal analyzer, a plain metal resistor of $1M\Omega$ was swapped with the bolometer. The noise power found then was very close to the noise power given by Nyquist formula.

The $1/f$ noise was found to follow the form

$$S_f = \frac{A(V_b)}{f^\gamma}, \tag{4.9}$$

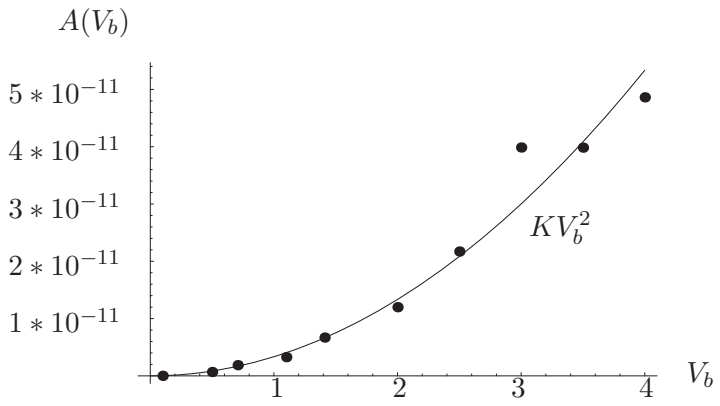

Figure 4.13: Noise Power Factor Evolution as a Function of Bias

where A is a constant that depends on the biasing voltage V_b. We found that $0.98 < \gamma < 1.06$ for all measured spectrum but with no trend that indicated a dependence on the biasing voltage. Therefore, for the rest of this analysis we chose to use $\gamma = 1$. Figure 4.13 shows the evolution of the noise power factor $A(V_b)$ as a function of bias. The continuous curve represents a parabolic fit with $K = 3.3 * 10^{-12}\, V^{-2}$. We conclude that $S_f(f) = \frac{3.3*10^{-12}V_b^2}{f}$ is a reasonable model for the $1/f$ generated by the bolometer and, if anything, an overestimation since the extra white noise might not come from the bolometer.

4.3.4 Analysis

Table 4.2 summarizes key properties of a bolometer having suspension legs $70\mu m * 5\mu m$, i.e., a number of electric and thermal conduction squares of 14. Similar electric and thermal properties should then be obtained with suspensions having dimensions $50\mu m * 3.6\mu m$. Some parameters were obtained by measurements presented in this section. Others, including the responsivity $\Re$ and the NETD, were calculated using definitions from Section 2.3. The parameters are compared with those reported for VOx bolometer in [1]. Even though the responsivity is higher in the work presented here, the $NETD$ for the same integration time ($5\mu s$) is close to three times higher. For the VOx bolometer, an integration time $\tau_{pulse} = 5\mu s$ and a biasing voltage of $5V$ leads to a temperature increase

$$\Delta T_{pulse} \simeq \frac{{V_b}^2}{R_0 C_{th}} \tau_{pulse} = 2K. \tag{4.10}$$

However, because the pyrolyzed-parylene bolometer has a much higher resistance, the same biasing voltage leads to a much smaller temperature increase, about $26mK$. Furthermore, because the films of pyrolyzed-parylene were prepared at high temperatures, we expect them to be able to withstand higher temperature increases during readout than VOx can. Therefore, longer integration times could be used for the carbon bolometer.

For an integration time $\tau_{pulse} = 100\mu s$, the NETD of our bolometer is reduced to $47mK$, which is comparable to that of the VOx bolometer. However, in imaging applications an array of bolometers needs to be completely read during each frame period ($33ms$). Having a longer integration time is therefore more demanding in term of the number of analog-to-digital required. Figure 4.14 shows the calculated noise contributions as a function of

Parameter	This Work	[1]
Suspension Dimensions	$70\mu m * 5\mu m$	$50\mu m * 2\mu m$
Suspension Material	$0.8\mu m$ Pyrolyzed Parylene	$0.8\mu m$ Silicon Nitride
Absorber Dimensions	$50\mu m * 50\mu m$	$35\mu m * 35\mu m$
Absorber Material	$0.2\mu m$ Pyrolyzed Parylene	$0.8\mu m$ Silicon Nitride
Resistance	$3.9M\Omega$	$20K\Omega$
TCR α	$-1.63\%.K^{-1}$	$-2.3\%.K^{-1}$
Sensing Material	Pyrolyzed Parylene	VOx
Thermal Conductance G_{th}	$9.6 * 10^{-8}\, W.K^{-1}$	$2 * 10^{-7}\, W.K^{-1}$
Thermal Capacitance C_{th}	$1.2 * 10^{-9}\, J.K^{-1}$	$3 * 10^{-9}\, J.K^{-1}$
Time Constant τ	$12.5ms$	$15ms$
Absorptivity η	0.6	0.8
Responsivity $\Re$ $(D.C.)$	$5.12 * 10^5 V.W^{-1}$	$4 * 10^5 V.W^{-1}$
$NETD$[1]	$109\, mK$	$39\, mK$
$NETD$[2]	$47\, mK$	–

[1] calculated for $V_b = 5V$, $\tau_{pulse} = 5\mu s$ and $1/f$ noise limit $f_1 = 10^{-3}Hz$
[2] calculated for $V_b = 5V$, $\tau_{pulse} = 100\mu s$ and $1/f$ noise limit $f_1 = 10^{-3}Hz$

Table 4.2: Summary of Bolometer Parameters

voltage bias. As can be seen, for biases $V_b < 2.6V$ the Johnson noise is dominating. However, both $1/f$ noise voltage and responsivity are proportional to the biasing voltage, while the Johnson noise is constant. Therefore, as the biasing voltage keeps increasing, the total noise becomes dominated by the $1/f$ noise and the NETD approaches the $1/f$ noise-limited

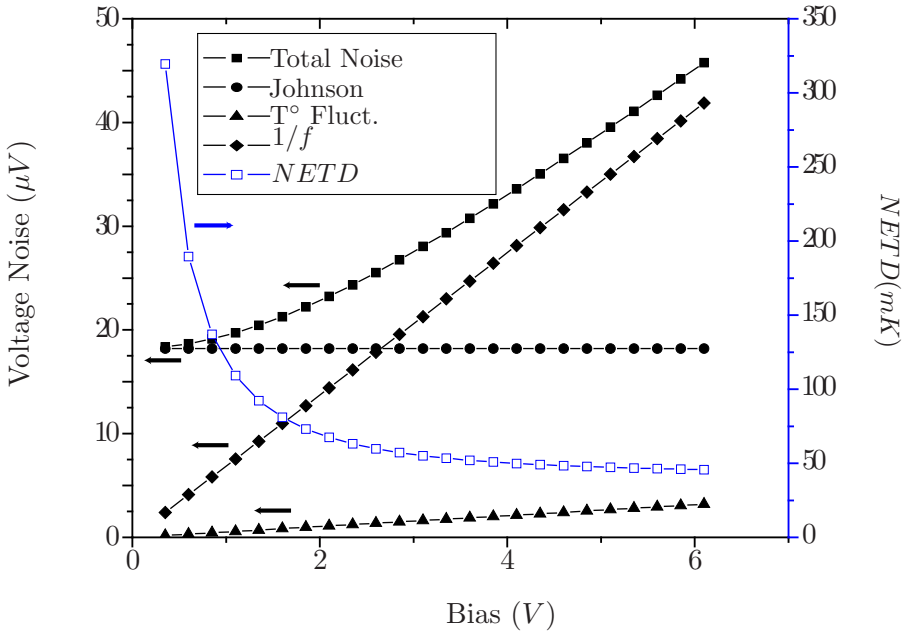

Figure 4.14: Noise Contributions for $\tau_{pulse} = 100\mu s$

NETD of Equation 2.77. Given thermal conductance, the temperature fluctuation noise is always one order of magnitude lower than the $1/f$ noise.

4.4 Conclusion

We have successfully fabricated uncooled infrared sensors with a simple two-layer pyrolyzed-parylene process. Electrothermal study shows that pyrolyzed-parylene is a promising candidate to replace silicon nitride and polysilicon for the thermal insulation, and that it can also be used to achieve high-TCR thin films for the pixel.

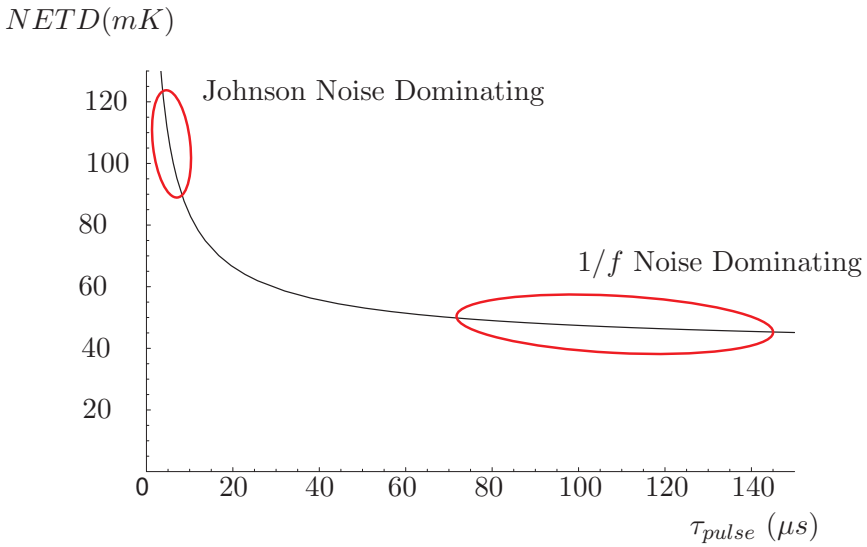

Figure 4.15: NETD for Varying Integration Time for $V_b = 5V$

Bibliography

[1] R. A. Wood, "Uncooled infrared imaging systems," in *Semiconductor and Semimetals* (D. D. Skatrud and P. W. Kruse, eds.), vol. 47, ch. 3, Academic Press, 1997. 85, 86, 93, 99, 100

[2] J. Tissot, "Ir detection with uncooled focal plane arrays. state of the art and trends," *Opto-Electronics Review*, vol. 12, no. 1, p. 105109, 2004. 85

[3] A. Rogalski, "Infrared detectors: Status and trends," *Progress in Quantum Electronics*, vol. 27, no. 2, pp. 59–210, 2003. 85

[4] A. Jahanzeb, C. Travers, Z. Celik-Butler, D. Butler, and S. Tan, "A semiconductor ybacuo microbolometer for room temperature ir imaging," *IEEE Transactions On Electron Devices*, vol. 44, pp. 1795–1801, October 1997. 85

[5] W. Boyle and K. Rodgers *Journal of The Optical Society of America*, vol. 49, no. 66, 1959. 85

[6] G. Shepard, "Static response characteristics for a carbon bolometer," *Journal of Applied Physics*, vol. 36, October 1965. 86

[7] M. Almasri, D. Butler, and Z. Celik-Butler, "Self-supporting uncooled infrared microbolometers with low-thermal mass," *Journal of Microelectromechanical Systems*, vol. 10, pp. 469–476, September 2001. 86

[8] S. C. S. Inc., "Product specifications, a-174 silane promotion." 89

[9] L. van der Pauw, "A method of measuring the resistivity and hall coefficient of lamellae of arbitrary shape," tech. rep., Philips, 1958. 90

[10] A. Walton, "Microelectronic test structures," tech. rep. 90

[11] D. W. Stops, "The mean free path of gas molecules in the transition regime," *J. Phys. D: Appl. Phys.*, vol. 3, 1970. 93

[12] X. He, T. Mei, W. Neuzil, and U.Sridhar, "Performance of microbolometer focal plane arrays uner varying pressure," *IEEE Electron Device Letters*, vol. 21, May 2000. 93

[13] M. Liger, S. Konishi, and Y. Tai, "Uncooled all-parylene bolometer," in *Technical Digest of The 17th IEEE International MEMS Conference (MEMS'04)*, pp. 593–596, 2004. 94

[14] M. von Arx, O. Paul, and H. Baltes, "Process-dependent thin-film thermal conductivities for thermal cmos mems," *Journal Of Microelectromechanical Systems*, vol. 9, March 2000. 96

[15] S. Hafizovic and O. Paul, "Temperature-dependent thermal conductivities of cmos layers by micromachined thermal van der pauw test structures," *Sensors and Actuators A*, vol. 97, no. 8, pp. 246–252, 2002. 96

[16] A. McConnell, S. Uma, and K. Goodson, "Thermal conductivity of doped polysilicon layers," *Journal of Microelectromechanical Systems*, vol. 10, pp. 360–369, September 2001. 96

Chapter 5

Uncooled Carbon Thermal Imager

This chapter presents a 1024 pixel parylene-pyrolyzed thermal imager. Using results from previous chapters, we designed and fabricated a $32 * 32$ array of carbon bolometers. Using infrared optics, we demonstrate for the first time the potential of this technology for uncooled thermal imaging.

5.1 Design

5.1.1 Pixel Layout

Figure 5.1 shows the pixel layout. The pitch distance was chosen to be $75\mu m$ in both directions. The main limitation for this number was the lithography and mask-making resolution. Nothing in the technology itself prevents us from fabricating arrays with a smaller pitch. The absorber area is $50\mu m * 50\mu m$ and is linked to the substrate by two suspension legs having dimensions $60\mu m * 2.8\mu m$ each. The fill factor is therefore 44.4%. On each pixel one suspension leg is connected to a "column" metal electrode (vertical line on Figure 5.1) while the other is connected to a "row" metal electrode (horizontal line on Figure 5.1). The two metal layers are insulated by a layer of parylene (non-pyrolyzed). The silicon underneath the absorber and suspension legs is removed to make the bolometers free-standing, while the metal electrodes and their contact with the suspension legs are deposited on silicon dioxide. Therefore, the silicon must be removed anisotropically in order to not undercut the metal electrodes.

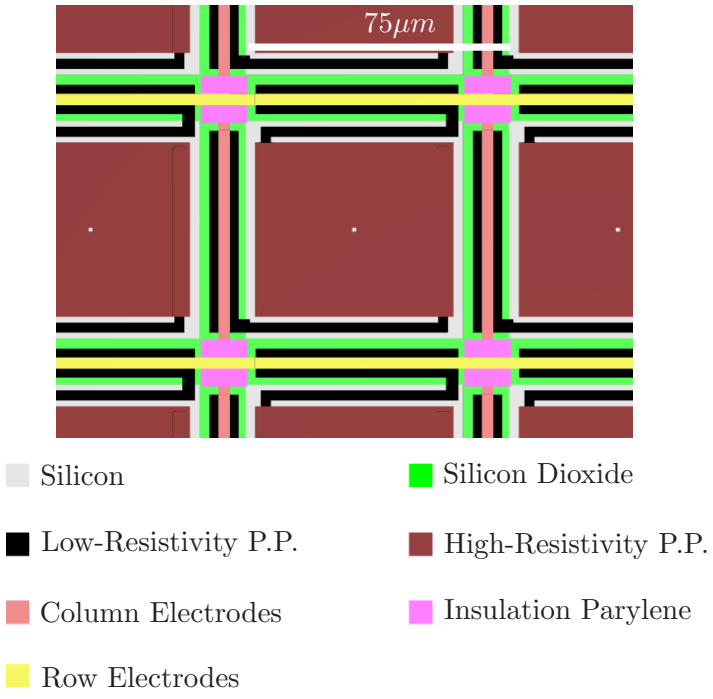

Figure 5.1: Pixel Layout

5.2 Fabrication

Two fabrication processes were explored in this work: a dry-etch bulk micromachining process and a wet-etch bulk micromachining process. Even though the wet process eventually proved to provide much better results, we present the dry process, as it may find some use for other applications.

5.2.1 Dry-Etch Bulk Micromachining Process

The Dry-Etch bulk micromachining process was the first process attempted in order to fabricate pyrolyzed-parylene bolometer arrays. There were two reasons for preferring dry etching *a priori* as opposed to wet etching: First, the interface between parylene and silicon or silicon dioxide is often reported to not withstand wet anisotropic etchants like Potassium Hydroxide (KOH) or Tetramethyl Ammonium Hydroxide (TMAH). Second, because the layers of pyrolyzed-parylene are only tenths of a micron in thickness, there was some concern that stiction would be unavoidable.

The main challenge when designing the dry-etch process was that we needed the bolometers to be freestanding, and therefore, needed the silicon underneath them to be undercut.

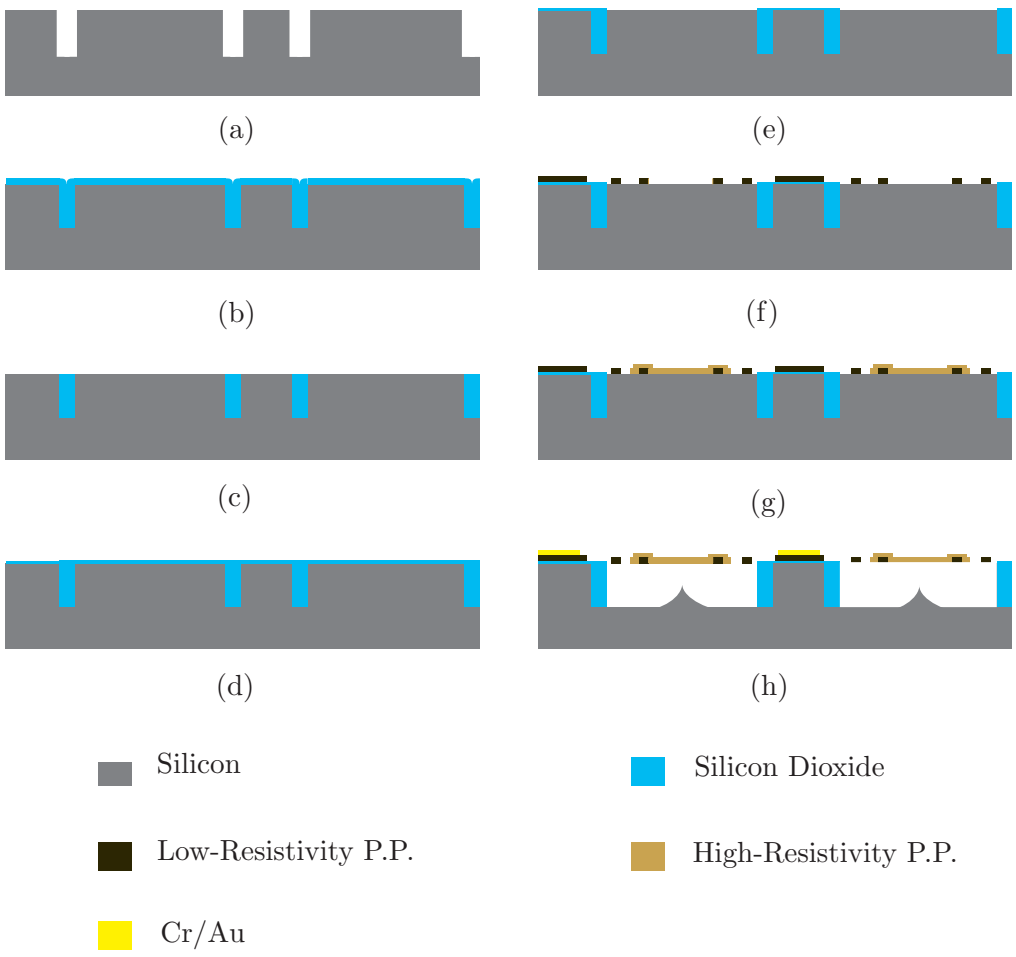

Figure 5.2: Process-Flow for Dry Release

At the same time, the silicon underneath the metal lines could not be undercut. To address this challenge, we developed a "Deep Shallow Trench Isolation" process, somewhat similar to the Shallow Trench Isolation (STI) process used to isolate devices in integrated circuits. However, in our case "isolation" stands for chemical insulation rather than electrical insulation.

The dry-etch bulk micromachining process flow is shown on Figure 5.2. First, Deep-Reactive Ion etching (DRIE) is used to etch trenches into the silicon substrate (a). Those trenches were $2\mu m$ in width. Then the trenches were filled with silicon dioxide in a thermal oxidation furnace (b). This is made possible by the conformality of silicon thermal oxidation. Also, because only 56% the silicon dioxide actually grows "out" of the silicon surface [1], $1.8\mu m$ of silicon dioxide growth are required to fill a $2\mu m$-wide trench. In the next step,

chemical-mechanical polishing (CMP) is used to delayer the silicon dioxide while providing a smooth surface for further processing (c).

A thin layer of thermal oxide is then grown to serve as electrical insulation (d). This oxide is patterned to leave the silicon exposed where the absorber and suspension legs are destined to be (e). A $4\mu m$-thick layer of parylene C is deposited, pyrolyzed at 800°C, and patterned by Reactive Ion Etching (RIE) (O_2 plasma) to define the suspension legs (f). As expected from previous experiments presented in Chapter 3, the pyrolyzed films shrunk to a thickness of $0.8\mu m$. A second layer of parylene C, $2.4\mu m$ in thickness, is deposited pyrolyzed at 640°C for 120 minutes and finally patterned to define the absorber area (g). The thickness after pyrolysis is $0.6\mu m$. A layer of chrome/gold/chrome (50Å/1000Å/50Å) is then deposited using a lift-off process. Because a thermal evaporator was used for this last step and because step coverage is needed, the wafers are titled at various angle during evaporation.

After an A174 silane coating is applied on the wafers [2] and a thin layer of parylene C ($0.3\mu m$) is deposited and patterned to serve as insulation between the column metal layer and the row metal layer. According the parylene dimer manufacturer, the dielectric strength for parylene C is $2.21 * 10^6 V.cm^{-1}$; therefore, this insulation should theoretically allow for voltage biases up to $66.3V$. The chrome/gold (50Å/2000Å) row metal layer is deposited using lift-off. Finally, the bolometers are released using XeF_2 gas-phase etching (h).

As mentioned in Chapter 3, having clean surfaces are essential to obtain good adhesion of parylene and pyrolyzed-parylene to their substrate. For this reason, $RCA-1$ cleaning is used before each of the three parylene depositions. Great precaution must be taken when releasing the bolometers. If etching is allowed to take place for too long, the etching front will reach the end of the silicon dioxide "isolation" trenches and the whole array will eventually be released.

The yield for the dry-etch process was found to be very small. Even though some arrays were successfully released, only about 70% of bolometers were operable. Also, long exposure to XeF_2 was found to damage the chrome/gold/chrome and chrome/gold electrodes. Therefore, the dry-etch was abandoned and the wet-etch process described in the next section was preferred.

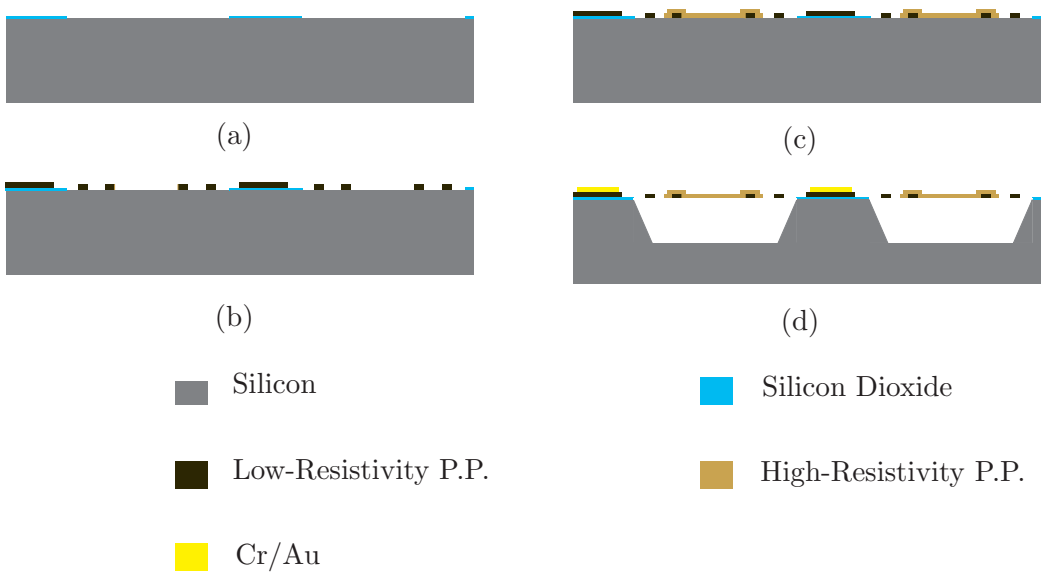

Figure 5.3: Process-Flow for Wet Release

5.2.2 Wet-Etch Bulk Micromachining Process

The Wet-Etch process described here uses TMAH. One remarkable property of TMAH silicon etching is that the etching of concave corners of (111) planes intersections while the convex corners are etched [3]. Also, TMAH is compatible with metals, and it was found that if appropriate precautions are taken, parylene/silicon dioxide interfaces do not delaminate. Therefore, using TMAH etching allows for the releasing of the bolometers while preserving the row and column metal lines as well as the silicon underneath them.

The Wet-Etch process can be seen in Figure 5.3. This process is much simpler and shorter than the dry-etch process. It begins with the growth of a thin layer of thermal oxide usede as electrical insulation and as mask for the final TMAH release. The rest of the process is very similar to the dry-etch fabrication process after its second silicon dioxide growth. A $4\mu m$-thick layer of parylene C is deposited, pyrolyzed at 800°C, and patterned by RIE (O_2plasma) to define the suspension legs (b). The thickness of the pyrolyzed-film was $0.8\mu m$ as expected. A second layer of parylene C, $2.4\mu m$ in thickness is deposited, pyrolyzed at 640°C for 120 minutes, and finally patterned to define the absorber area (c). The etching of the second layer of pyrolyzed-parylene must be timed carefully to avoid over-etching the first layer, which is unprotected. The thickness of the first layer of pyrolyzed parylene decreased to $0.75\mu m$ after the second layer patterning. The thickness of the second

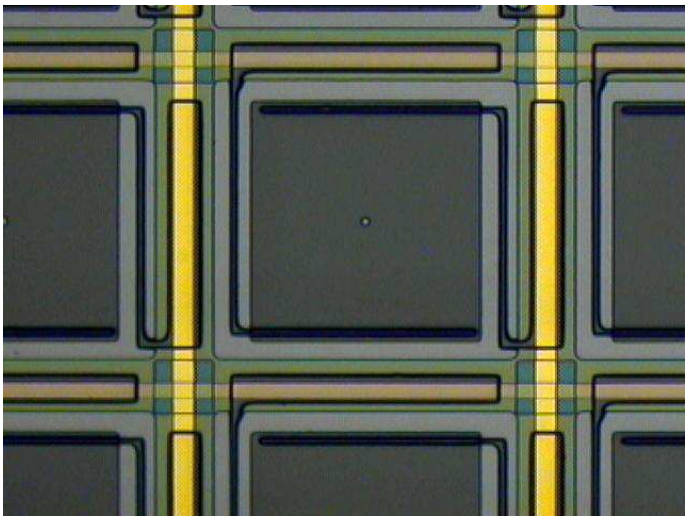

Figure 5.4: Pixel Before Release

pyrolyzed-parylene film was $0.6\mu m$. A layer of chrome/gold/chrome (50Å/1000Å/500Å) is deposited using a lift-off process to define the column metal layer. After applying an A174 silane coating as adhesion promoter on the wafers [2], a thin layer of parylene C ($0.3\mu m$) is deposited and patterned to serve as insulation between the column metal layer and the row metal layer. Again, because the two layers of pyrolyzed-parylene are unprotected during the insulation parylene etching, this etching must be timed carefully. The first layer of pyrolyzed-parylene after the insulation parylene patterning was $0.65\mu m$ and the thickness of the second pyrolyzed film was $0.4\mu m$. The chrome/gold (50Å/2000Å) row metal layer is deposited using lift-off. Figure 5.4 shows a pixel and part of its neighbors at this step of the process (right before release).

After dicing, the bolometers are released in a 15% solution of $TMAH$ taken to 90°C in a reflux system. The chips are rinsed for 15min in a water tank before they are immersed in methanol. In order to avoid stiction, the chip must not be allowed to dry. Each chip is finally dried using CO_2 supercritical drying in a Tousimis system. Figure 5.5 shows a released array at different magnifications.

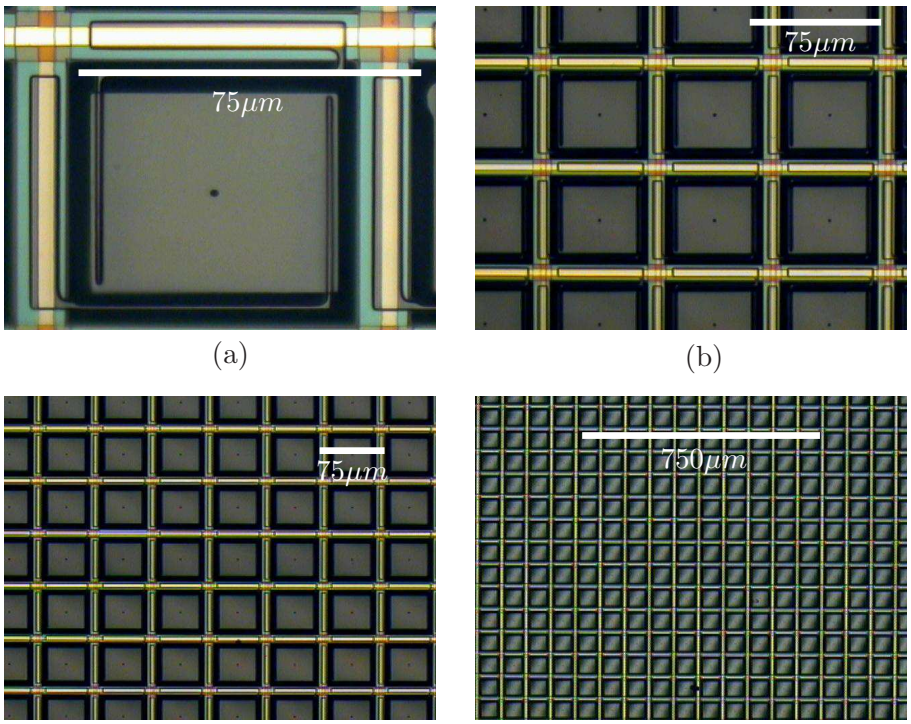

(a) (b)

(c) (d)

Figure 5.5: Release Bolometer Array

5.3 Characterization

5.3.1 Electrical Properties

First, the resistance of the bolometers was measured in N_2 and at low bias to avoid self-heating. The resistance across a $12 * 11$ array was $3.8M\Omega$ on average with a standard deviation of $421K\Omega$. This mediocre uniformity could be due to inaccuracy in the mask-making process. However, it should be noted that in a bolometer array, uniformity of dark resistance is not crucial. More important is the uniformity of responsivity (hence uniformity of thermal conductance). Thickness measurements across the $32 * 32$ array showed good thickness uniformity. The average resistivity, calculated assuming the contributions the suspension leg resistance were negligible, was $\rho = 3.04 * 10^2\Omega.cm$.

The TCR of the bolometers was measured in an oven with flowing N_2 using a precision thermocouple as reference. The TCR was measured to be $\alpha = -2.1\%$, which is what could be expected from the resistivity.

5.3.2 Thermal Properties

The arrays were then placed into a vacuum chamber at $20mTorr$ and allowed to stabilize for 2 hours to desorb any moisture. The current-voltage characteristic was measured using an Hewlett-Packard HP4145B semiconductor parameters analyzer. During such testing, attention must be paid to the power dissipated by the bolometers as the bolometers experience an increase in temperature that is proportional to this power. In our experiments, the power dissipated was kept lower than $0.5\mu W$. Figure 5.6 shows the relationship between dissipated power and resistance for a bolometer pixel. Since the resistance change is given by

$$\Delta R = \alpha R_0 \frac{P}{G_{th}}, \tag{5.1}$$

the data represented in Figure 5.6 gives us a direct measurement of α/G_{th}. The thermal conductance was then calculated using the previously measured TCR, leading to a value $G_{th} = 6.1 * 10^{-8}W.K^{-1}$. The absorptivity was measured using a EDO Corporation Infrascope (infrared microscope). The obtained absorptivity was $\eta \simeq 0.6$. However this piece of equipment actually measures the absorptivity from $1\mu m$ to $5.5\mu m$. Assuming the carbon acts as a graybody, the radiation conductance is calculated to be

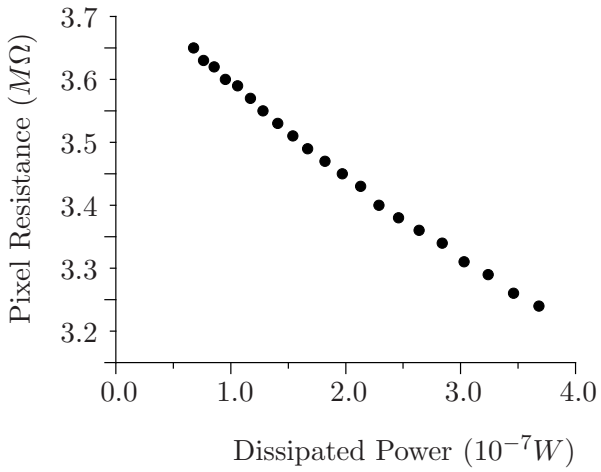

Figure 5.6: Bolometer Pixel Power-Resistance Relationship

$G_{rad} = 1.86 * 10^{-8} W.K^{-1}$. The thermal conductance of the suspension legs is then calculated to be $G_{leg} = 4.24 * 10^{-8} W.K^{-1}$ (or $2.12 * 10^{-8} W.K^{-1}$ for each leg). This is less than what could be expected from the suspension dimensions ($60\mu m * 2.8\mu m * 0.8\mu m$) and thermal conductivity reported in 4.3.2. This discrepancy is due to the fact that the actual width of the suspension legs is between $1.5\mu m$ and $2\mu m$ due to undercut during the etching as well as some exposure to O_2 plasma during the etching of the second layer of pyrolyzed-parylene and insulation parylene.

In an experiment similar to that presented in Section 4.3.2, the bolometers' thermal time constant was measured using a light chopping wheel at various frequencies. The thermal constant was found to be $31ms$, which with the value of G_{th} previously measured allows us to calculate the thermal capacitance to be $C_{th} = 1.9 * 10^{-9} J.K^{-1}$. The obtained time constant is close to the period corresponding to $30Hz$ ($33ms$). Therefore, the responsivity will drop for signals close to that frequency. However, this could be solved by reducing the pixel thickness (although this could lead to a decrease in absorptivity). From the TCR, absorptivity, and thermal conductivity the responsivity can be calculated using Equation 2.27:

$$\Re = \frac{\alpha \eta V_b}{G_{th}} = 1.03 * 10^6 V.W^{-1},$$

for $V_b = 5V$.

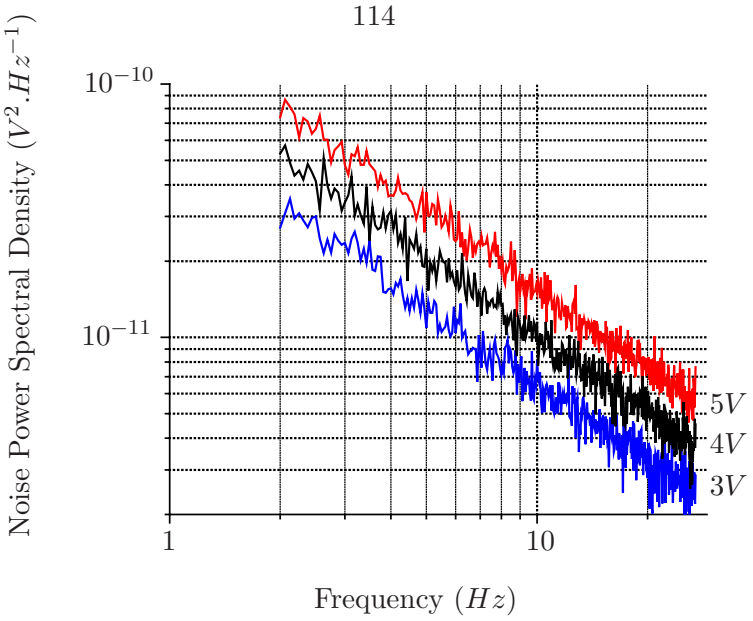

Figure 5.7: Low Noise Power Spectrum

5.3.3 Noise

The noise of individual pixels was measured using a dynamic signal analyzer as explained in Section 4.3.3. Figure 5.7 shows a typical $1/f$ noise spectrum for different biasing voltages. This measurement was performed in air. The extracted noise factor extracted from this data is $K = 6.4{*}10^{-12}$, higher than the noise reported in Chapter 3. One reason could be that the resistivity of the pyrolyzed-parylene is about four times higher than the pyrolyzed-parylene used in the single-element bolometer. It is well-known that materials with higher resistivity usually have higher $1/f$ noise.

5.3.4 Performance

Table 5.1 shows the calculated noise contributions of Johnson noise, $1/f$ noise and temperature fluctuation noise for $V_b = 5V$, $F = 1$ and a limit to $1/f$ noise $f_1 = 10^{-3}Hz$. Similar to the single-pixel bolometer presented in Chapter 3, the noise in the array is dominated by Johnson noise for an integration time $\tau_{pulse} = 5\mu s$ and by $1/f$ noise if $\tau_{pulse} = 100\mu s$. The corresponding NETD are $57mK$ and $31mK$ respectively. $31mK$ is very close to state of the art bolometers (it is actually a little better than the VOx bolometer reported in [4]). However, for an array of $320 * 200 = 64000$ pixels, an integration time of $100\mu s$ would require 193 analog-to-digital converters in order to read all pixels within

	$\tau_{pulse} = 5\mu s$	$\tau_{pulse} = 12\mu s$	$\tau_{pulse} = 100\mu s$
Johnson Noise (μV)	79.3	51.2	17.7
$1/f$ Noise (μV)	54.0	52.6	49.3
Temperature Fluctuation Noise (μV)	2.7	2.7	2.7
Total Noise(μV)	**96.0**	**73.5**	**52.5**
$NETD$	**57 mK**	**44mK**	**31mK**

Table 5.1: Bolometer Noise Contributions

one frame period of $33.3ms$. As explained in Section 2.5.5, once the integration time is long enough for the noise to be dominated by $1/f$ noise, little is gained from increasing it further. A good trade-off value for the integration time is when the Johnson noise and the $1/f$ noise contributions are equal:

$$KV_b{}^2\Big(\frac{3}{2} - \gamma - \ln(2\pi f_1 \tau_{pulse})\Big) = 4kTR_0(\frac{1}{2\tau_{pulse}} - f_1) \quad (5.2)$$

$$\tau_{pulse} = 11.3\mu s. \quad (5.3)$$

Using this integration time leads to an NETD of $44mK$ and would require 24 analog to digital converters, which is a more reasonable number.

Table 5.2 shows a summary of parameters for the pyrolyzed-parylene carbon bolometer array compared with the VOx bolometer array of [4].

5.4 Thermal Imaging

5.4.1 Testing Setup

Figure 5.8 shows the testing setup used to produce infrared images. The chips are mounted on a flange facing a Zinc Sulfide (ZnS) window obtained from ISP Optics Corporation.[1] Zinc sulfide has an external transmittance between 60% and 70% between $0.5\mu m$ and $14\mu m$. An array of 24 electrical feedthroughs was made in another flange using vacuum epoxy. This limits the thermal imaging capability to $12 * 11$ pixels (the last feedthrough begin used for grounding). Figure 5.9 shows the bolometer array mounted on its flange and seen through the ZnS window.

[1] http://www.ispotics.com

Parameter	This Work	[4]
Pitch	$75\mu m$	$50\mu m$
Suspension Dimensions	$60\mu m * 2\mu m$	$50\mu m * 2\mu m$
Suspension Material	$0.8\mu m$ Pyrolyzed Parylene	$0.8\mu m$ Silicon Nitride
Absorber Dimensions	$50\mu m * 50\mu m$	$35\mu m * 35\mu m$
Fill Factor	44%	70%
Absorber Material	$0.5\mu m$ Pyrolyzed Parylene	$0.8\mu m$ Silicon Nitride
Resistance	$3.8M\Omega$	$20K\Omega$
TCR α	$-2.1\%.K^{-1}$	$-2.3\%.K^{-1}$
Sensing Material	Pyrolyzed Parylene	VOx
Thermal Conductance G_{th}	$6.1 * 10^{-8}\, W.K^{-1}$	$2 * 10^{-7}\, W.K^{-1}$
Thermal Capacitance C_{th}	$1.9 * 10^{-9}\, J.K^{-1}$	$3 * 10^{-9}\, J.K^{-1}$
Time Constant τ	$31ms$	$15ms$
Absorptivity η	0.6	0.8
Responsivity $\Re$ $(D.C.)$	$\mathbf{1.03 * 10^6 V.W^{-1}}$	$\mathbf{4.6 * 10^5 V.W^{-1}}$
NETD[1]	**57 mK**	**39 mK**
NETD[2]	**44 mK**	–
NETD[3]	**31 mK**	–

[1] Calculated with $V_b = 5V$, $F = 1$, $\tau_{pulse} = 5\mu s$ and a limit to $1/f$ noise $f_1 = 10^{-3}Hz$
[2] Calculated with $V_b = 5V$, $F = 1$, $\tau_{pulse} = 12\mu s$ and $f_1 = 10^{-3}Hz$
[3] Calculated with $V_b = 5V$, $F = 1$, $\tau_{pulse} = 100\mu s$ and $f_1 = 10^{-3}Hz$

Table 5.2: Summary of Bolometer Array Parameters

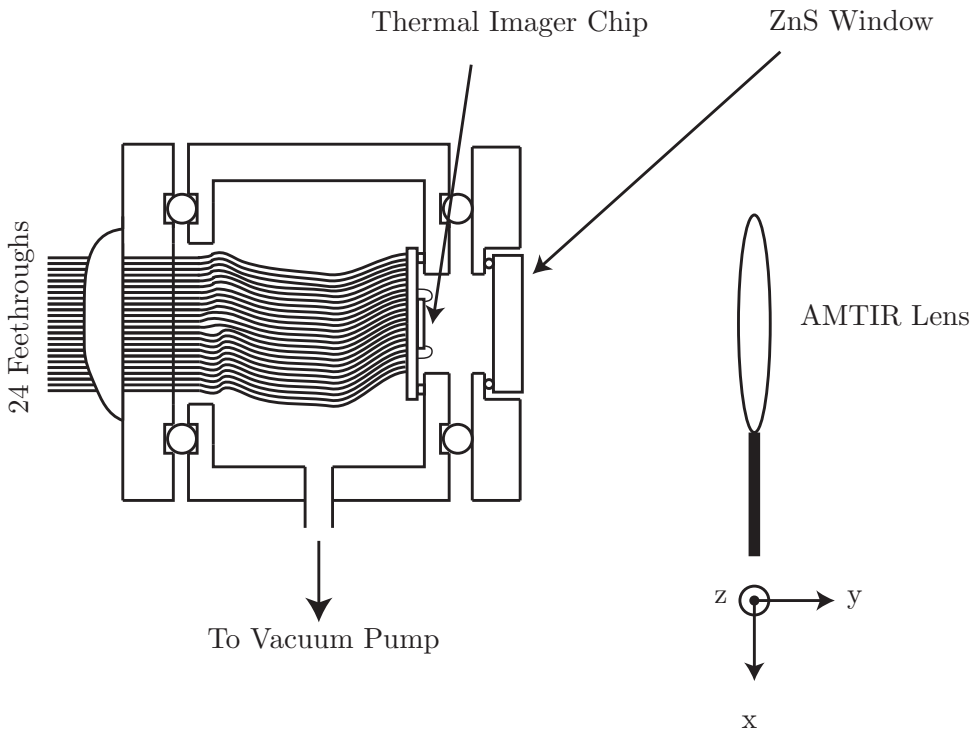

Figure 5.8: Schematic of Testing Setup

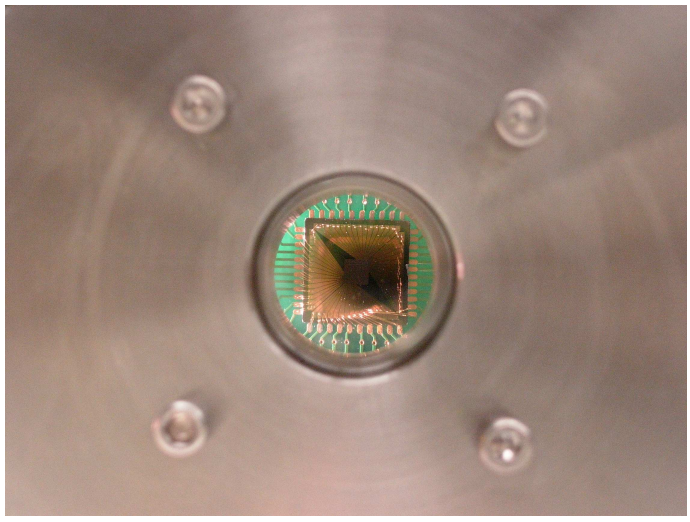

Figure 5.9: Thermal Imager Chip Seen Through ZnS Window

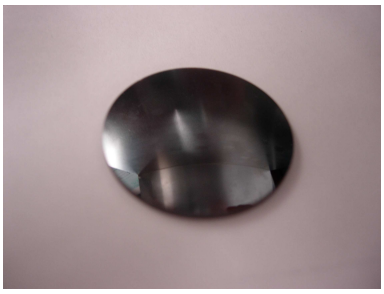

Figure 5.10: AMTIR Lens

An F/1.5 Amorphous Material Transmitting Infrared (AMTIR[2]) lens with focal length $38mm$ (obtained from Newport Corporation[3]) is mounted on an x-y-z stage outside of the vacuum chamber. The external transmittance of AMTIR is greater than 60% from $1\mu m$ to $14\mu m$. Figure 5.10 shows the lens.

Figure 5.11 shows the circuit used to read each pixel. A voltage bias is applied to one row at a time. Each column electrode is connected to an operational amplifier used as an inverting amplifier. The voltage at the output of an amplifier is given by

$$V = -\frac{V_b R_l}{R}, \tag{5.4}$$

where R_l is the feedback resistance used in the inverting amplifier.

A Hewlett-Packard HP34970A data acquisition system was used together with a 34903A 20-channel actuator module to apply the biasing voltage on the desired row and a 34901A 20-channel multiplexer to measure the voltage of the desired column. The HP34970A was remotely controlled with a computer through its General Purpose Interface Bus (GPIB). A C++ software was written to selectively access the pixels. In "continuous" mode the resistance of a given pixel is monitored continuously and can be saved. The resistance change expected from infrared illumination being smaller than the variation of resistance across the array, a calibration was necessary. To calibrate the array a "dark-image" mode was implemented. In this mode the resistance of each pixel is measured sequentially and saved. In an "image" mode the resistance of each pixel is measured and subtracted from the resistance measured in "dark-image" mode. The image is then displayed and saved. Figure 5.12 shows a screen capture of the software, while the radiation of a flashlight was

[2] $Ge_{33}As_{12}Se_{55}$
[3] http://www.newport.com

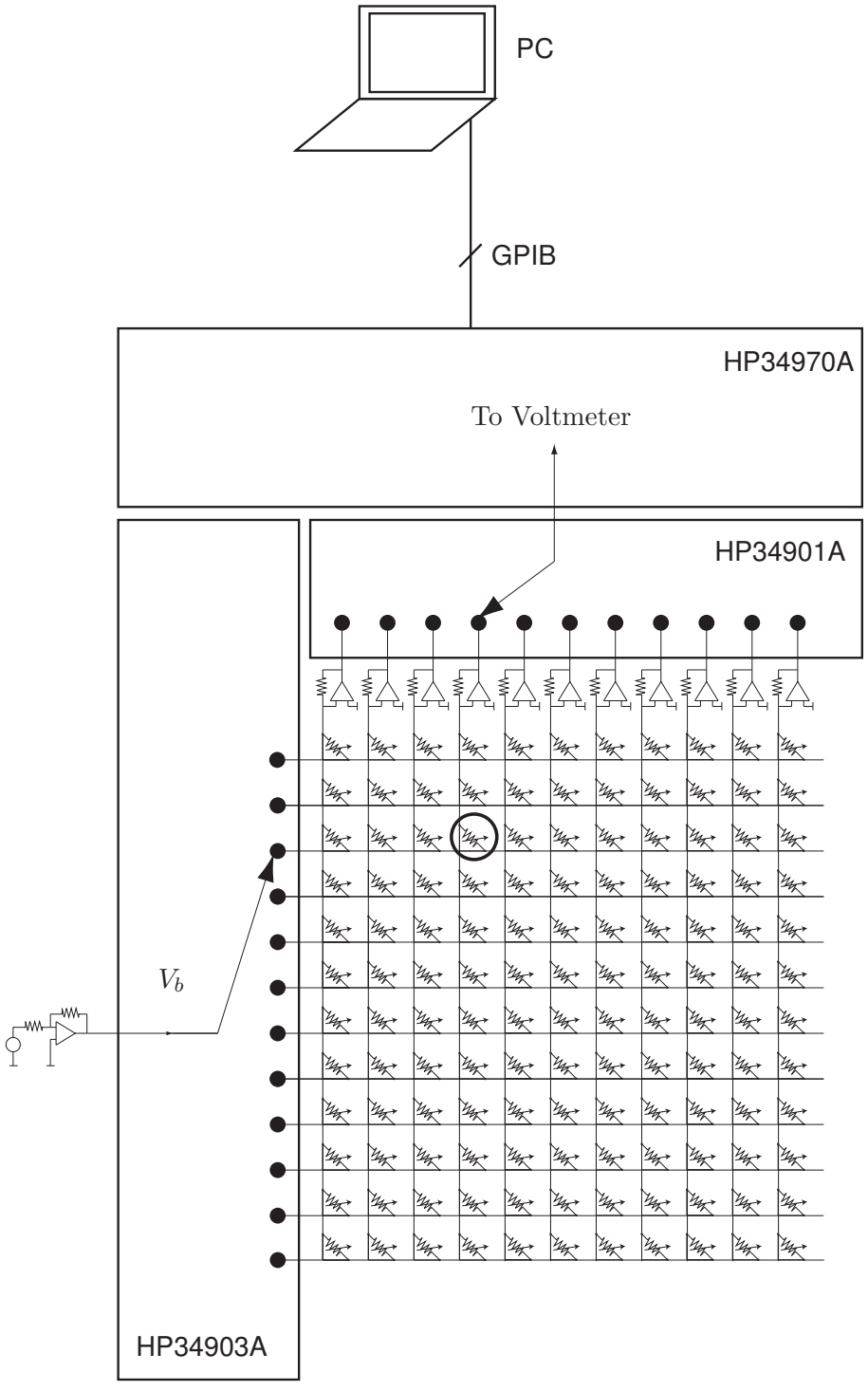

Figure 5.11: Thermal Imager Readout Setup

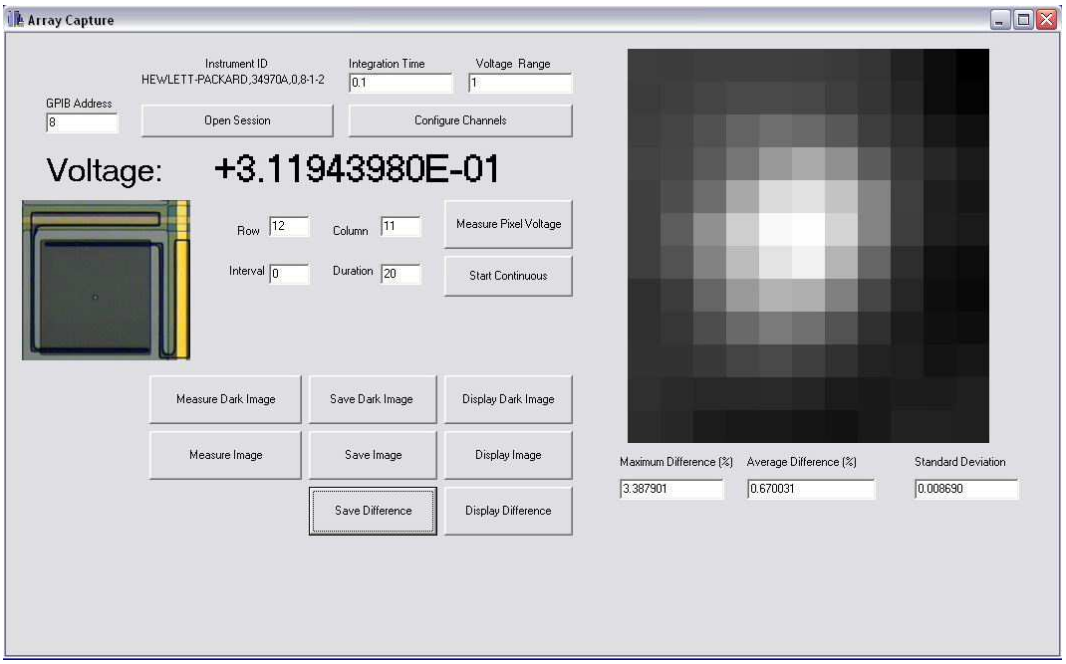

Figure 5.12: Readout Software

focused on the array.

5.4.2 Results

A $50W$ regular visible lamp was used to focus the array. The light was directed to the array and the position of the lens was adjusted using the x-y-z stage while monitoring the voltage on the central pixel continuously. Once the maximum voltage change is obtained, the lamp is replaced with the desired target. Figure 5.12shows a screen capture of the software window after an image was read.

Because the electronics were outside of the vacuum chamber, far away from the bolometers, a lot of noise is picked up during readout, although it does not come from the bolometers themselves. Therefore, only hot surfaces $> 100°$C were captured.

Figure 5.13 shows the tip of a soldering iron at a $3m$ distance.

$$\begin{aligned} \frac{1}{f} &= \frac{1}{z_i} + \frac{1}{z_o} \\ z_i &= \frac{f z_o}{z_o - f} = 38.5mm, \end{aligned}$$

where f is the focal length of the lens, z_o the object distance, and z_i the image distance.

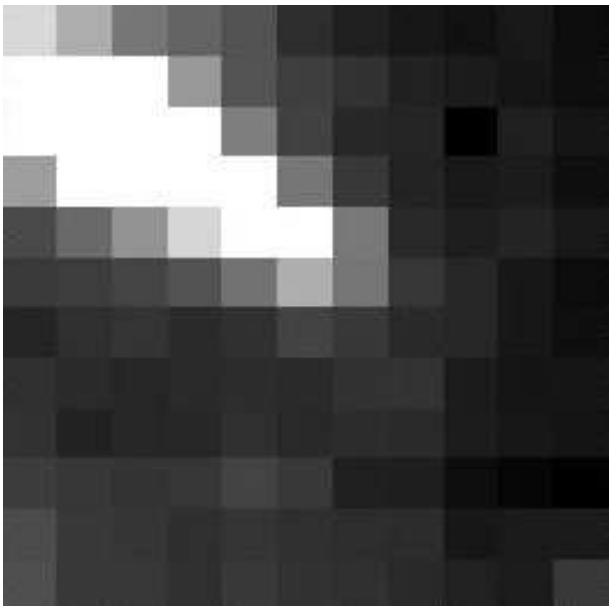

Figure 5.13: Soldering Iron Tip at 3m

The magnification factor is

$$M = \frac{z_i}{z_o} = 1.28 * 10^{-2}.$$

therefore each pixel correspond to an object area of $5.9mm$ and the total image area is $7.1cm * 6.5cm$.

Figure 5.14 shows thermal images obtained by arranging power resistors arranged in a "C" and an "O" pattern, as well as the same image after spatial interpolation. The maximum change of resistance in Figure 5.14 was -3.6%. Note that pixel $(3, 9)$ is consistently darker than its neighbors. After inspection under microscope, it was found that a piece of debris was thermally shorting the absorber and the column electrode. For all arrays tested the pixel operability was better than 98%.

5.5 Conclusion

We have designed, fabricated, and tested a carbon bolometer array based on two layers of pyrolyzed-parylene. Test results show good responsivity, acceptable noise, and high pixel operability. However, resistance uniformity remains an issue, and the thermal constant $(31ms)$ should be decreased for optimal operation at video frame rate.

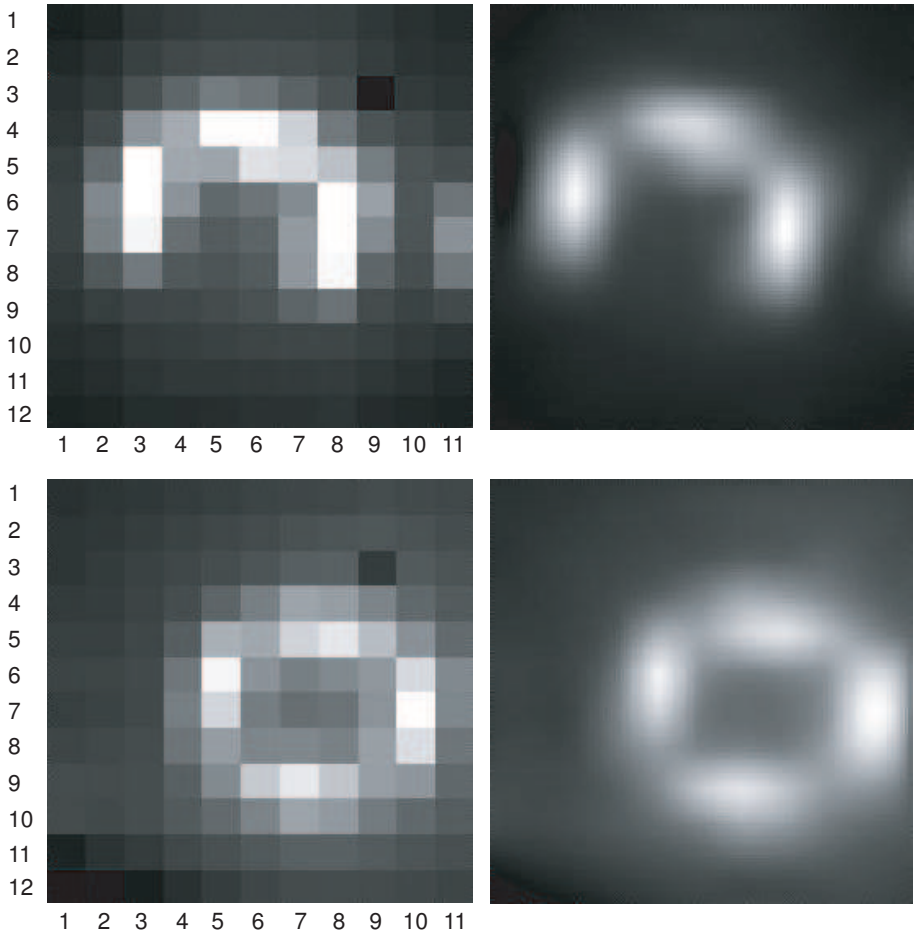

Figure 5.14: Power Resistors at 3m

Calculations show that if the same design was used in a $320 * 200$ array using an integration time of $12\mu s$ the NETD for $F/1$ optics would be $44mK$ which is very close to the state of the art. Such an array would require 24 analog to digital converters. This is very encouraging considering that this is the first reported carbon microbolometer. The thermal imaging functionality was demonstrated on a $12 * 11$ subset of the array.

Bibliography

[1] S. Wolf and R. Tauber, *Silicon Processing for the VLSI Era*. Lattice Press, 1986, vol. 1. 107

[2] S. C. S. Inc., "Product specifications, a-174 silane promotion." 108, 110

[3] G. Kovacs, N.I.Maluf, and K. Petersen, "Bulk micromachining of silicon," in *Proceedings of the IEEE*, vol. 86, no. 8, August 1998, pp. 1536–1551. 109

[4] R. A. Wood, "Uncooled infrared imaging systems," in *Semiconductor and Semimetals*, D. D. Skatrud and P. W. Kruse, Eds. Academic Press, 1997, vol. 47, ch. 3. 114, 115, 116

Chapter 6

Conclusion and Future Directions

In this work we have demonstrated how pyrolysis of parylene can be used to fabricate carbon microbolometers for uncooled thermal imaging on a chip and to produce carbon films that are easily integrated in standard microfabrication processes. We then showed that the properties of pyrolyzed-parylene carbon can be process-tuned to produce films with different electrical and thermal properties. Resistivity can be tuned between $10^{9}\Omega.cm$ and $10^{-2}\Omega.cm$, while the temperature coefficient of resistance changes from $4\%.K^{-1}$ to $0.3\%.K^{-1}$.

We fabricated a novel all-carbon microbolometer with a unique design using two layers of pyrolyzed parylene. Using the tunability of pyrolyzed-parylene carbon, we produced films with low electrical resistivity yet low thermal conductivity to serve as thermal insulation, while the absorber part of the bolometer was made out of carbon having high resistivity and a high temperature coefficient of resistance. With this design, the resistance of the whole device is dominated by the temperature-sensitive part while achieving high thermal insulation. After having characterized the various properties of the carbon microbolometer, including their excess noise, we set out to fabricate a $32 * 32$ array of carbon bolometers for thermal imaging applications. Using a wet bulk micromachining process we obtained arrays a pixel operability greater than 98% and a responsivity to infrared light of $10^{6}V.W$ for a $5V$ bias. We then demonstrated the thermal imaging functionality by taking thermal images using an infrared lens. Calculation using noise measurement results show that the sensitivity to target temperature (NETD) can be as low as $31mK$ and $44mK$ for $100\mu s$ and $12\mu s$ electrical signal integration time, respectively. This is very close to the current state of the art of microbolometers.

Future possible directions include the development of a surface-micromachined process

to improve the optical fill factor and absorptivity as well as reducing the pixel dimensions. More importantly, novel processes of reducing the $1/f$ noise in pyrolyzed-parylene carbon films should be explored, as it is the current performance-limiting factor. Possible strategies include annealing or the use of special gases during pyrolysis, e.g., forming gas. Another challenge is integration with electronics. The current process does not allow for monololithic integration with CMOS or bipolar electronics to high temperature processing steps. Ways of locally converting polymer films into carbon films with appropriate properties could be one way to solve this problem, e.g, using laser.

Index